

# REPORT DOCUMENTATION PAGE

Form Approved  
OMB No. 0704-0188

Public reporting burden for this collection of information is estimated to average 1 hour per response, including the time for reviewing instructions, searching existing data sources, gathering and maintaining the data needed, and completing and reviewing the collection of information. Send comments regarding this burden estimate or any other aspect of this collection of information, including suggestions for reducing this burden, to Washington Headquarters Services, Directorate for Information Operations and Reports, 1215 Jefferson Davis Highway, Suite 1204, Arlington, VA 22202-4302, and to the Office of Management and Budget, Paperwork Reduction Project (0704-0188), Washington, DC 20503.

1. AGENCY USE ONLY (Leave blank)		2. REPORT DATE 7 Jan. 99		3. REPORT TYPE AND DATES COVERED DISSERTATION	
4. TITLE AND SUBTITLE THE TI:SAPPHIRE RING LASER GYROSCOPE				5. FUNDING NUMBERS	
6. AUTHOR(S) CAPT BOHN MATTHEW J					
7. PERFORMING ORGANIZATION NAME(S) AND ADDRESS(ES) UNIVERSITY OF NEW MEXICO				8. PERFORMING ORGANIZATION REPORT NUMBER	
9. SPONSORING/MONITORING AGENCY NAME(S) AND ADDRESS(ES) THE DEPARTMENT OF THE AIR FORCE AFIT/CIA, BLDG 125 2950 P STREET WPAFB OH 45433				10. SPONSORING/MONITORING AGENCY REPORT NUMBER  FY99-7	
11. SUPPLEMENTARY NOTES					
12a. DISTRIBUTION AVAILABILITY STATEMENT Unlimited distribution In Accordance With AFI 35-205/AFIT Sup 1				12b. DISTRIBUTION CODE	
13. ABSTRACT (Maximum 200 words)					
14. SUBJECT TERMS				15. NUMBER OF PAGES	
				16. PRICE CODE	
17. SECURITY CLASSIFICATION OF REPORT	18. SECURITY CLASSIFICATION OF THIS PAGE	19. SECURITY CLASSIFICATION OF ABSTRACT	20. LIMITATION OF ABSTRACT		

# **The Ti:sapphire Ring Laser Gyroscope**

by

**Matthew John Bohn**

**B.S., Physics, United States Air Force Academy, 1988**  
**M.S., Physics, University of New Mexico, 1993**

DISSERTATION

Submitted in Partial Fulfillment of the  
Requirements for the Degree of  
**Doctor of Philosophy**  
**Optical Sciences**

The University of New Mexico  
Albuquerque, New Mexico

May, 1998

**DISTRIBUTION STATEMENT A**

Approved for public release;  
Distribution Unlimited

19990120 008

Matthew John Bohn  
Candidate

Physics and Astronomy  
Department

This dissertation is approved, and it is acceptable in quality  
and form for publication on microfilm:

*Approved by the Dissertation Committee:*

Jean Claude Guil, Chairperson

J. M. L. L.

S. R. J. Bruck

M. J. McAuliffe

Accepted:

Robin Muir - Grochowski

Dean, Graduate School

APR 14 1998

Date

©1998, Matthew John Bohn

DTIC QUALITY ASSURED



## **DEDICATION**

To my loving wife, Susan.

## ACKNOWLEDGMENTS

I would like to acknowledge the support of the United States Air Force Academy's Department of Mathematical Sciences for granting me this three year fellowship to complete my doctorate. I would like to thank Jean-Claude Diels for being available to answer questions and give advice. There are many people that I have turned to over the years for advice, but I need to especially remember the other members of my committee who took the time to read my manuscript: Jack McIver, Mansoor Sheik-Bahae, Steve Brueck and Mike McAuliffe. Karl Koch and Gerry Moore were also very helpful in the design of the OPO. There are many graduate students that have helped me in our mutual pursuit of wisdom and knowledge, these include (but are not limited to): Jason Jones, Jayesh Jasapara, Peter Dorn, Mike Dearborn, Tom Alley, Doug Nelson, Patrick Rambo, Jens Biegert, Jeff Nicholson, Scott Diddams, and Briggs Atherton.

Lastly I must thank my wife Susan for her loving support and incessant encouragement. And my two children, Luke and Hannah, who put it all in proper perspective and make it all worthwhile.

# **The Ti:sapphire Ring Laser Gyroscope**

by

**Matthew John Bohn**

## **ABSTRACT OF DISSERTATION**

Submitted in Partial Fulfillment of the  
Requirements for the Degree of  
**Doctor of Philosophy**  
**Optical Sciences**

The University of New Mexico  
Albuquerque, New Mexico

**May, 1998**

# THE TI:SAPPHIRE RING LASER GYROSCOPE

by

**Matthew John Bohn**

B.S., Physics, United States Air Force Academy, 1988

M.S., Physics, University of New Mexico, 1993

Ph.D., Optical Sciences, University of New Mexico, 1998

## ABSTRACT

This dissertation studied the Ti:sapphire laser as a pulsed ring laser gyroscope. Several new cavity designs were demonstrated, including a saturable absorber mode-locked laser gyroscope, a linear cavity laser, a Kerr-lens mode-locked femtosecond laser gyroscope, and a solid-state mutual Kerr-lens mode-locked ring gyroscope.

A solid-state ring laser gyroscope using a dye-jet saturable absorber was studied for the first time. This laser produced the lowest beat frequencies recorded in a pulsed laser (10 Hz with a 10 Hz bandwidth) and also the narrowest beat note bandwidth at 0.85 Hz. This low beat frequency bandwidth corresponds to a nonreciprocal change in optical path length of  $7 \times 10^{-15}$  meters. A sensitive technique to measure the intensity dependent refractive index,  $n_2$ , was developed using this laser. Null-bias dithering was

**DISTRIBUTION STATEMENT A**

Approved for public release;  
Distribution Unlimited

demonstrated for the first time using an electro-optic modulator. A new method of extracting the average beat frequency from a dithered laser was discovered and the experimental result was verified with an analytic solution.

A novel linear cavity with two pulses in the cavity was used for the first time to measure electro-optic coefficients. This laser can be analyzed as an extremely elongated ring laser with the difference being that the pulses are indistinguishable which implies no bias beat frequency.

Kerr-lens mode-locking was demonstrated for the first time in a ring laser gyroscope. This laser employed both passive negative and positive feedback in the same Kerr element. Both continuous wave operation and Q-switched mode-locked operation were demonstrated without lock-in. A novel method of stabilizing the crossing point in a ring laser was demonstrated by using mutual Kerr-lens mode-locking which resulted in a bidirectional, solid-state ring laser. Finally a bidirectional OPO ring gyroscope was designed. The OPO ring gyroscope solves many of the problems of a solid-state ring including, gain competition, lock-in and bias.

# Contents

<b>List of Figures</b>	<b>xii</b>
<b>1 Introduction</b>	<b>2</b>
1.1 Laser gyros . . . . .	4
1.1.1 Bias . . . . .	5
1.1.2 Lock-in . . . . .	6
1.1.3 Dithering . . . . .	14
1.1.4 Optimizing the modulation frequency in a dithered laser gyro . . .	17
1.1.5 Pulsed laser gyro . . . . .	18
1.1.6 Other solid-state laser gyros . . . . .	20
1.2 Soliton-like pulse shaping . . . . .	21
1.2.1 Historical . . . . .	22
1.2.2 Theory: wave equation and group velocity dispersion . . . . .	24
1.2.3 Self-phase modulation (chirp) . . . . .	26
1.2.4 Soliton solution . . . . .	27
<b>2 Saturable Absorber Mode-locked Ti:sapphire Laser</b>	<b>34</b>
2.1 Linear cavity . . . . .	35
2.1.1 Experimental setup . . . . .	36
2.1.2 Electro-optic measurements . . . . .	38
2.2 Ring gyro . . . . .	41
2.2.1 Large ring . . . . .	48
2.3 Electro-optic dither (theory and experiment) . . . . .	48

2.3.1	Introduction . . . . .	48
2.3.2	Null-bias dithering: experimental . . . . .	50
2.3.3	Derivation of modulation spectrum . . . . .	53
2.4	Solid-state saturable absorber . . . . .	64
2.4.1	Lock-in . . . . .	66
2.5	Conclusion . . . . .	67
<b>3</b>	<b>Kerr-lens Mode-locked Ti:sapphire Laser</b>	<b>68</b>
3.1	Introduction . . . . .	68
3.2	Preventing phase coupling between counter-propagating beams . . . . .	69
3.3	Preventing unidirectionality . . . . .	70
3.4	Experimental setup . . . . .	71
3.5	Unidirectional mode-locked pulses . . . . .	72
3.6	Q-switched mode-locked pulses . . . . .	74
3.6.1	Passive negative feedback . . . . .	76
3.7	Continuously mode-locked bidirectional operation . . . . .	77
3.7.1	Cavity analysis . . . . .	77
3.7.2	Experimental results . . . . .	82
3.8	Mutual Kerr-lens mode-locked . . . . .	91
3.8.1	Introduction . . . . .	91
3.8.2	Theory . . . . .	92
3.8.3	Experimental results . . . . .	95
3.8.4	The mysterious blue light . . . . .	100
3.9	Conclusions . . . . .	102
<b>4</b>	<b>Future Work</b>	<b>106</b>
4.1	OPO . . . . .	107
4.1.1	Introduction . . . . .	107
4.1.2	Spatial walk-off . . . . .	108

4.1.3	Temporal walk-off . . . . .	108
4.1.4	Spectral bandwidth . . . . .	109
4.1.5	Tuning . . . . .	109
4.1.6	Alignment . . . . .	109
4.1.7	Double pulse operation . . . . .	110
4.1.8	Bidirectional operation . . . . .	110
4.2	OPO pump-probe experiments . . . . .	112
4.3	Stopping the earth . . . . .	113
4.4	Bragg reflector vibrations . . . . .	113
4.5	Differential optical path meter . . . . .	114
4.6	Metal detector . . . . .	115
4.7	Decoupling of mutual Kerr-lens mode-locking . . . . .	116
4.8	Saturable Bragg reflector . . . . .	117
4.9	Ti:sapphire initiator . . . . .	117
4.10	Mapping the stability region of a Kerr-lens mode-locked ring laser . . . . .	118
4.11	Postmortem examination of failed experiments . . . . .	119
4.11.1	Cross phase modulation in Ti:sapphire . . . . .	119
4.11.2	Phase multiplier . . . . .	120
4.11.3	Pump/probe experiments with Schott glass . . . . .	121
4.12	Conclusions . . . . .	121



# List of Figures

1.1	A) Linear cavity: no bias beat note. B) Saturable absorber mode-locked: low beat frequencies and low bandwidths. C) Kerr-lens mode-locked: femtosecond pulses. D) Mutual Kerr-lens mode-locked: solid-state. . . . .	3
1.2	Vector change in $E_1$ as a result of scattering from $E_2$ . . . . .	7
1.3	Theoretical plot of the beat signal as a function of time. The plots A, B, C and D correspond to data points on the experimental lock-in curve plotted in Figure 1.5. . . . .	8
1.4	Time series of the beat signal at locations A,B, C and D along the lock-in curve. . . . .	9
1.5	Average beat frequency of the laser versus the effective rotation rate. . . . .	10
1.6	Experimental setup for the lock-in experiments. A reflective tape was used to scatter part of the CW beam into the CCW beam. . . . .	11
1.7	Plot of the beat signal as a function of time for 8 different values of $\beta$ , the scattering phase, in increments of $\pi/4$ . . . . .	12
1.8	The solid line is the mean frequency solution to the lock-in equation with $\Omega_{lock} = 10$ kHz. The instantaneous frequency varies between the upper and lower bounds. . . . .	13
1.9	FFT of plot C in Figure 1.4. The harmonics of the beat frequency follow a straight line in the log-linear plot because the amplitude of the harmonics are a geometric series. . . . .	15
1.10	Frequency response of a dithered gyro. Nearly linear response is restored near zero; however, when $\Omega_{rotation} = m\Omega_{dither}$ , the laser will lock again. . .	16

1.11	Schematic of ring laser with nonreciprocal intensities at the saturable absorber.	20
1.12	Laser diode ring gyroscope. The diodes are actively modelocked by gain switching. The R, S and P were used to induce coupling in the device. . .	21
1.13	The continuous wave fiber ring laser. The Faraday rotator in between the polarizers generates a bias beat note to prevent lock-in. . . . .	22
1.14	Typical Lorentzian dispersion curve near a resonance. Most glasses have positive GVD in the visible-infrared region because of an ultraviolet absorption edge. . . . .	24
1.15	Broadening of a pulse in a dispersive medium. . . . .	25
1.16	Negatively chirped pulse traveling through a medium of positive dispersion. The pulse initially compresses and then spreads. . . . .	26
1.17	Demonstration of Self-Phase Modulation (SPM) resulting in a chirped pulse.	27
1.18	Typical Kerr-lens modelocked Ti:sapphire laser. The radius of curvature of mirrors is 10 cm concave. The prism sequence has a net negative GVD to compensate for the GVD of the Ti:sapphire. Notice the 'red' ray travels through more glass which delays it with respect to the 'blue' ray. . . . .	31
2.1	Experimental setup: The dye jet is in the center of the cavity. The curved mirrors have a 5 cm focus. The output coupler (OC) is 1.3% transmitting, and the other flat mirror is a maximum reflector (R= 99.9%). The Ti:sapphire is 8 mm long. The SF-14 prisms are separated by 37 cm. . . .	37
2.2	Beat note as detected on a digital oscilloscope without averaging or smoothing.	38
2.3	Beat frequency versus optical delay (squares) and the plot of the voltage difference applied to the sample (curve). . . . .	39
2.4	LiNbO3 modulator processed in-house. The optical axis is coming up out of the page. . . . .	40
2.5	Beat frequency versus applied voltage for two different polarizations. . . .	41
2.6	Background-free second-order intensity autocorrelation of a Ti:sapphire ring laser mode-locked with an absorbing dye jet without prisms for GVD compensation. $\tau_{pulse} = 17.3$ ps. . . . .	42

2.7	Experimental arrangement for ring gyro. Fused silica plate is used to minimize the size of the beat note interferometer. . . . .	43
2.8	Smallest bandwidth ever recorded using a Ti:sapphire ring laser gyro. The time series shows only a small portion of the data. The data was taken for 0.74 seconds. . . . .	44
2.9	Log plot of Figure 2.8. Notice the $1/f$ noise and the beat note spike that is 50 db above the noise. . . . .	45
2.10	Lowest beat note recorded using a Ti:sapphire laser. The data was taken for 10 seconds, which implies a resolution of 0.1 Hz. Comparison with Figure 2.8 indicates that the broader bandwidth here is to be attributed to random frequency drifts on a time scale of seconds. . . . .	46
2.11	Plot of the beat frequency versus the location of CdS inside the cavity. . .	47
2.12	FFT of beat signal from 10 meter perimeter ring laser gyro. . . . .	49
2.13	Experimental setup for null-bias dithering. A small quartz plate is inserted near the crossing point at Brewster's angle to output couple two beams for the beat note detection. . . . .	50
2.14	Upper plot is the square wave modulation that is applied to the RF signal via an RF mixer. The lower plot is the corresponding beat signal. . . . .	51
2.15	Amplitude of $\omega_1$ beat note as a function of the modulation frequency. The data is fit to an exponential decay. . . . .	52
2.16	Upper: Beat signal as seen on the oscilloscope. The low frequency modulation is highlighted by the curve. Below: FFT of the beat signal. . . . .	53
2.17	Beat signal demonstrating the roll-off to $\omega_{ave}$ . Notice in this plot that the beat signals at $\omega_1$ and $\omega_2$ are barely visible. . . . .	54
2.18	Amplitude of average frequency as a function of modulation frequency. The model is $f_{mod} * P1 * \sin(P2/f_{mod})$ . . . . .	55
2.19	Plot of P2 fit parameter versus the beat frequency difference. The slope of the straight line is predicted by theory to be $\frac{\pi}{4}$ . . . . .	56

2.20	Plot of the phase as a function of time. The phase is continuous, but discontinuous in slope. The dotted line is the average phase. The modulation period is $2T$ . . . . .	57
2.21	Generated beat signal. The modulation frequency is 1.0, $\omega_1$ is 5.2 and $\omega_2$ is -4.7. Notice the faint modulation beginning to show at $\omega_{ave}$ . . . . .	58
2.22	Generated beat signal. The modulation frequency is 10, $\omega_1$ is 5.2 and $\omega_2$ is -4.7. Here we see the rolloff toward $\omega_{ave}$ is almost complete, there is only a small modulation at the original beat frequencies. The time scale is different from the graph above. . . . .	59
2.23	Setup of solid-state absorber experiments. Several absorbers were tried, including the RG-830 that is displayed. . . . .	65
3.1	Experimental setup. A1 and A2 are apertures. Curved mirrors have radii of 10 cm. Flat mirrors have reflectivities 0.999 (left) and 0.987 (right). Brewster-cut 8 mm Ti:sapphire rod. . . . .	71
3.2	CCW (upper) and CW (lower) outputs of laser demonstrating switching of laser output. Note the laser is unidirectional at all times. Detectors are p-i-n photodiodes with a bandwidth of 1 GHz, although the digitizing oscilloscope's bandwidth is 1 MHz. . . . .	73
3.3	CCW (upper) and CW (lower) pulses demonstrating Q-switch pulses. The period of pulses varied from 4 to 7 $\mu$ s. The inset shows a subset of the mode-locked pulse train within the Q-switch envelope. . . . .	75
3.4	Experimental arrangement for bidirectional Q-switched mode-locked pulses.	76
3.5	CW and CCW outputs in Q-switched operation are temporally overlapped.	77
3.6	Beat note of Q-switched pulses. Coupling is DC because the signal is pulsed. Notice the contrast is 60%. There are more than 3000 pulses in this plot and only 2048 data points. This undersampling explains the aperiodic nature of Q-switched pulses. . . . .	78
3.7	Plot of the beam waist in the Ti:sapphire crystal. The length of the crystal is about 10 times longer than the confocal parameter. . . . .	79

3.8	Plot of effective crystal length versus actual crystal length. Note for lengths longer than the Rayleigh range, the effective length is approximately a constant. $a$ is an empirically determined constant[1, 2]. . . . .	80
3.9	Location of the nonlinear lens plotted as a function of the location of the crystal with respect to the beam waist. . . . .	81
3.10	Beam waist in the nonlinear crystals, Ti:sapphire and ZnS, as a function of the number of computer iterations. . . . .	82
3.11	Theoretical graph of linear and nonlinear cavity waists plotted versus distance in the cavity. The distance is measured from the center of the Ti:sapphire rod in the CCW direction. A1 is the location of the Kerr-lens aperture. A2 is the location of the aperture for passive negative feedback. The plot begins and ends in the Ti:sapphire crystal. . . . .	83
3.12	Background free intensity autocorrelation. Traces obtained immediately after one another, only slit A2 was closed by 0.05 cm for bidirectional operation. The dashed lines are a Gaussian fit to the autocorrelation. The Gaussian pulsewidths are 220 fs for unidirectional and 420 fs for bidirectional. . . . .	84
3.13	CCW (upper) and CW (lower) output demonstrating the lack of switching as compared with Figure 3.2. The detectors and time base are the same as Figure 3.2. The dropouts are a result of unidirectional operation, which explains why the spikes are negatively correlated. . . . .	85
3.14	Difference frequency of the combined CW and CCW pulses. The Brewster reflections from two prisms are recombined after an appropriate delay onto a slow detector. . . . .	86
3.15	Beam waist in Ti:sapphire crystal. The upper equations apply for the CW pulse, and the lower equations are for the CCW pulse. Because of the asymmetry, the peak intensity will be less for the CW pulse. . . . .	87

3.16	Setup for beat note detection, auto and cross correlations. The $\lambda/2$ waveplate at locations A and B control the auto and cross correlations, respectively. The beam combiner for the beat note detection is a 50/50 beam splitter, while the beam splitter/combiner for the auto/cross correlator is a polarizing beam splitter. . . . .	89
3.17	Auto and cross correlations of CW and CCW pulses. The cross correlation lies between the autocorrelations of the CW and CCW pulses, which implies no timing jitter between the pulses with a margin of error of 30 fs. . . . .	90
3.18	Beam waist as a function of position in the cavity. The calculation begins and ends in the Ti:sapphire crystal, TiS. Three different cases are plotted: continuous-wave, single-pulse and bidirectional pulses. . . . .	94
3.19	Experimental setup for mutual Kerr-lens mode-locking in ZnS. The ZnS crystal is 3 mm long and at Brewster's angle. The cavity fold mirrors all have a radius of curvature of 10 cm. . . . .	96
3.20	Experimental arrangement for mutual Kerr-lens mode-locking. The bidirectional pulses meet in the ZnS crystal. . . . .	96
3.21	Beat signal versus time demonstrates the evolution of the interferogram from locked to a frequency of about 8 kHz. . . . .	97
3.22	CCW signal (top) and beat note (bottom). Notice that the beat frequency appears as an amplitude modulation on the CCW pulse train. . . . .	98
3.23	Normalized FFT of the beat signal in Figure 3.22. The second harmonic of the beat signal is easily identified and yields a geometric series ratio, $r = .032$ . . . . .	99
3.24	Autocorrelation of the CCW pulse train. The pulse width is calculated to be $18.6 \pm .08$ ps. . . . .	100
3.25	Autocorrelation of the CW pulse train. The pulsewidth is calculated to be $22.6 \pm .13$ ps. . . . .	101
3.26	Cross-correlation between the CW and CCW pulses. The minimum width predicted from the autocorrelations is 29 ps. . . . .	102

3.27	Spectra of CW and CCW pulse trains. The FWHMs are 2.5 and $2.65 \pm .04$ nm for the CW and CCW pulses. The resolution of monochromator is 0.4 nm. . . . .	103
3.28	Schematic of blue beams emanating from ZnS crystal. The beams are identified as: reflected surface second-harmonic (RSSH), transmitted surface second-harmonic (TSSH) and sum-frequency generation (SFG). . . . .	104
3.29	Wave vectors involved in SFG (Sum Frequency Generation). The beams are mixed in the intracavity ZnS crystal. The larger beams are the strong, intracavity fundamental beams. The weaker solid beams are the surface reflection of the fundamental. The dotted lines are the SFG beams. . . . .	105
3.30	Spectra of CW and CCW surface second-harmonic and the spectrum of sum frequency generated normal to the ZnS crystal. . . . .	105
4.1	Tuning curve of signal wavelength as a function of pump wavelength for noncritical phase matching in KTP . . . . .	110
4.2	The cavity perimeter is 4 times the length of the pump cavity, which produces two OPO pulses in the OPO cavity. The ROC of the curved mirrors is 10 cm concave. The curved mirrors are max-R at the signal wavelength and high-T at the pump and idler wavelength. . . . .	111
4.3	The OPO cavity is twice as long as the pump cavity, therefore there will be two pulses in the OPO cavity. ROC of curved mirrors is 10 cm concave. The curved mirrors are max-R for the signal and high-T for the pump and idler. . . . .	111
4.4	A 50/50 beamsplitter divides the pump pulse into two beams. The split off beam is delayed such that the CW and CCW pulses meet only in air. The radius of curvature of the curved mirrors is 10 cm concave. The curved mirrors are max-R at the signal wavelength and high-T at the pump and idler wavelengths. . . . .	112

4.5	Similar to the double ring cavity in Figure 4.2. The second pulse is split off and pumps the KTP crystal from the opposite direction. The advantage is that the full pump pulse is used in each direction. The disadvantage is that the cavity perimeter must be 4 times the cavity length of the pump. . . . .	113
4.6	Bidirectional ring with modulated pump pulse. Every other pump pulse is selected to pump sample. The OPO pump is split by a 50/50 beam splitter.	114
4.7	The top schematic shows the layout of the modulators and polarizing beam splitter. The middle schematic shows the optical path when the device is measuring a rotation. The bottom schematic shows the optical figure-8 path when the device is measuring the bias beat note. . . . .	115
4.8	End mirror of typical Ti:sapphire cavity is replaced with a concave mirror which focuses the beam onto the semiconductor end mirror. The beams must be focused to achieve the maximum modulation. The $\text{LiIO}_3$ crystal generates the second-harmonic. The $\text{LiTaO}_3$ is an electro-optic modulator.	116
4.9	Schematic for testing optical elements. Every other pulse is deflected at the sample, yielding a differential measurement of its thickness. . . . .	117
4.10	Schematic of a laser gyro metal detector. Any ferrous material that enters the field emitted by the coil will be detected as a change in beat note. . . .	118
4.11	The polarizing beam splitter separates the s and p polarizations. The s polarization is injected back into the cavity. The modulator selects every other pulse to be injected back into the cavity by switching the pulses between s and p polarization. . . . .	119
4.12	The intracavity beam is incident on the dove prism such that it is always totally internally reflected. The modulator selects every other pulse out of the Ti:sapphire laser. The $\text{LiIO}_3$ crystal generates the second-harmonic. The $\text{LiTaO}_3$ crystal is an electro-optic modulator. . . . .	121
4.13	A) Linear cavity: no bias beat frequency. B) Saturable absorber mode-locked ring gyro: measured low beat frequencies. C) Kerr-lens mode-locked ring gyro: femtosecond pulses. D) Mutual Kerr-lens mode-locked: all solid-state. . . . .	122



# Chapter 1

## Introduction

Laser gyroscopes are a billion dollar[3] industry because of the demand for an accurate rotation sensor in guided weapons, airplanes, submarines, automobiles, ships and satellites[4]. Other applications include the study of geophysical phenomena such as the wind, rain and tides that can alter the rotation rate of the earth[5]. Sensitive gyroscopes can also be used to detect earthquakes and other movements of the earth's surface[6, 7]. In addition to the applications above, pulsed laser gyros can study nonreciprocal optical effects[8]. Pulsed laser gyros are an area of research that has been largely unexplored. In the 60s the HeNe laser was mode-locked to reduce the lock-in band, but was not very successful[9]. In the 70s the Soviets studied the actively mode-locked Nd:YAG laser as a possible laser gyroscope[10, 11]. In the 90s the mode-locked ring dye laser [12, 13] and the diode laser[14] were studied for the first time as possible gyro candidates. More recently solid-state lasers such as Ti:sapphire, Cr:LiSAF and Cr:YAG have entered the arena with excellent stability, high power and extremely short pulses.

The Ti:sapphire laser is less noisy than a ring dye laser, it is easier to operate and is also capable of producing sub-10 femtosecond (fs) pulses. Ti:sapphire can be pumped by an Argon ion laser, which makes it simple and cheap to replace the gain medium in a CPM ring dye laser with a Ti:sapphire crystal. The lifetime of Ti:sapphire differs from dyes by about 3 orders of magnitude, and this difference has created many problems in building a bidirectional femtosecond Ti:sapphire laser. These problems have resulted in new cavity designs, several new methods of mode-locking and a new design of a pulsed gyro based on an

Optical Parametric Oscillator (OPO). The OPO design is extremely exciting and has the potential to revolutionize the gyro industry. Because the OPO might be sensitive enough to be used for gravity wave detection, it could very well pave the road toward a Nobel Prize.

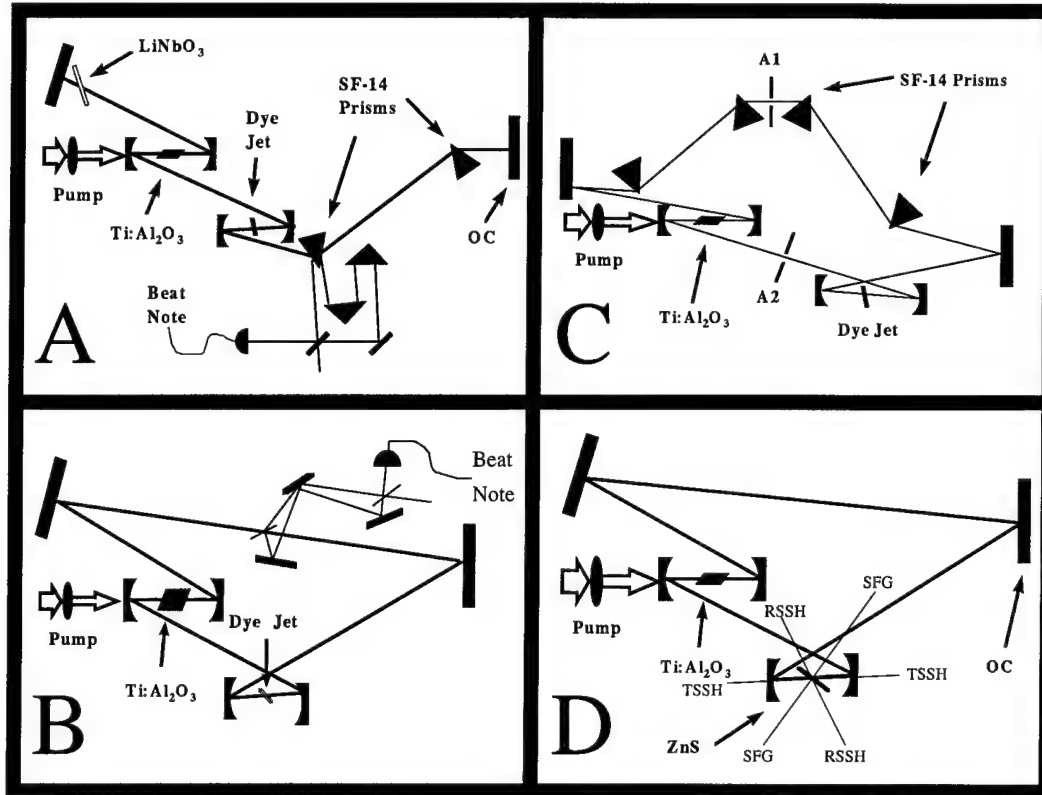


Figure 1.1: A) Linear cavity: no bias beat note. B) Saturable absorber mode-locked: low beat frequencies and low bandwidths. C) Kerr-lens mode-locked: femtosecond pulses. D) Mutual Kerr-lens mode-locked: solid-state.

The rest of Chapter 1 will fill in the background on ring lasers and short-pulsed lasers. Chapter 2 will present a novel laser design that I like to call "The Linear Gyro" (see Figure 1.1A), and also some new experimental and analytic results on electro-optic dithering of a laser gyro (see Figure 1.1B). The world's first Kerr-lens mode-locked femtosecond bidirectional ring laser gyro (see Figure 1.1C) is presented in Chapter 3. Q-switched mode-locked operation is obtained by using a concentrated dye solution and a two-photon absorber. A novel method of mode-locking is introduced in Chapter 3 called mutual Kerr-lens mode-locking, which generates CW and CCW pulses without a saturable absorber and is completely solid-state (see Figure 1.1D). The Bidirectional Optical Parametric Oscillator (OPO)

Ring Gyro (or BORG) is an exciting design that is presented in Chapter 4. Numerous applications of sensitive gyros are outlined in Chapter 4 entitled "Future Work." Chapter 4 also includes experiments that would make excellent follow-on projects for graduate-level research. Chapter 4 concludes with failed experiments and a brief explanation about why they did not work. This dissertation chronicles the advancement of pulsed ring laser gyros from the dye laser into an all solid-state system.

## 1.1 Laser gyros

When a bidirectional ring laser is rotated in the clockwise (CW) direction, the clockwise traveling wave will see a slightly longer cavity because the mirrors of the cavity are moving away from the propagation direction. Likewise the counter-clockwise (CCW) wave will see a slightly shorter cavity because the cavity mirrors are moving opposite to the propagation vector. The slight change in cavity length ( $P$  for perimeter) will result in a slight shift in the frequency ( $\nu$ ) of the laser. When the CW and CCW beams are combined on a detector, the frequency difference (called the beat frequency  $\Delta\Omega$ ) is measured. It is a trivial derivation, but still worthwhile. The frequency of a laser is defined to be:

$$\nu = q \frac{c}{P} \quad (1.1)$$

where  $q$  is the number of half-wavelengths that "fit" into the laser cavity. A small change in  $P$  results in a differential change in the frequency:

$$\Delta\nu = q \frac{c}{P^2} \Delta P \quad (1.2)$$

substituting in the definition of  $\nu$ :

$$\Delta\nu = \frac{\nu}{P} \Delta P \quad (1.3)$$

or:

$$\frac{\Delta\nu}{\nu} = \frac{\Delta P}{P} \quad (1.4)$$

Thus a small change in cavity length results in a large change in frequency because the frequency difference is multiplied by the frequency of light. A small change is defined as

$\Delta P < \frac{\lambda}{4}$  because a change of  $P$  greater than a quarter-wavelength would lead to ambiguous results for a mode-locked system because the change in frequency would be closer to the next longitudinal mode. The range  $\Delta P$  could be extended to  $\frac{\lambda}{2}$  if the ambiguity of sign were removed from the beat note. Another way to arrive at this same result is to consider that the repetition rate of the laser is  $\frac{c}{P}$ , the Nyquist theorem states that the maximum frequency that can be resolved is  $\frac{c}{2P}$ . A beat frequency of  $\frac{c}{2P}$  would correspond to a  $\Delta P$  of  $\frac{\lambda}{2}$ . Since a quarter-wavelength is much, much smaller than the cavity length, the use of differentials is well justified in the derivation above. The same derivation will also work for any other interaction that will lead to a difference in optical path length for the CW and CCW directions.

### 1.1.1 Bias

A bias beat note is a frequency difference that is caused by something other than a rotation. If it cannot be properly compensated, it will lead to a source of error. Unlike the mode-locked laser gyro that will be presented in the next section, there are few effects in the continuous wave laser gyro that will lead to a bias beat note. This is a result of the light being of low intensity and continuous and therefore lacking a large nonlinear drive.

Fresnel drag is one way to obtain an artificial bias beat note. This was originally discovered in the HeNe system because the electrical discharge imparts momentum to the atoms and the unexcited atoms diffuse toward the cathode[15]. The electrical discharge imparts a uniform distribution while the back-diffusion is parabolic, thus creating a net velocity difference in the center of the tube. Fresnel drag is demonstrated in a laser gyro by simply using an air hose and blowing it along one of the arms of the laser. This effect is a result of the velocity addition in special relativity[15, 16, 17, 18]. The phase velocity of light in a moving medium is:

$$v = \frac{c}{n} \pm V_{medium} \left( 1 - \frac{1}{n^2} \right) \quad (1.5)$$

where the  $\pm$  depends on whether the light is moving with or against the velocity of the

medium,  $V_{medium}$ , which leads to a frequency difference in a ring laser gyro of:

$$\Delta\Omega = 2(n^2 - 1)V_{medium}\frac{d}{\lambda P} \quad (1.6)$$

where  $d$  is the length of the medium and  $P$  is the perimeter of the laser gyro. The change in frequency observed in our laser was on the order of a few hundred Hz.

A Faraday rotator will also induce a difference in the optical path length. The setup consists of a Faraday rotator separated by two quarter wave plates. The Faraday material has a different refractive index for the left-hand circularly polarized light than for right-hand circularly polarized light. This leads to a difference in optical path length for the two beams. Since the two counter-propagating beams have different polarizations, they could be spatially separated by using polarizing beam splitters. In fact, this bias has been analyzed using spatially resolved eigenstates[19, 20].

### 1.1.2 Lock-in

For a laser gyro to work properly, the frequencies of the CW and CCW modes must be independent of one another. Any coupling between the two will result in frequency pulling and a reduction in the measured rotation rate. This coupling is similar to injection locking where a small signal is injected into a free-running oscillator and causes the oscillator's frequency to tune. If the scattering is severe enough or the frequency difference between the CW and CCW modes is small enough, then the two modes can actually lock to one another resulting in no measured beat frequency. This disastrous frequency range is called the 'dead-band'.

Next we will derive the lock-in equation (Adler's equation) and analyze the beat frequency as initially derived by Aronowitz[15], reworked by Dennis and Diels[21] and analyzed by Stedman[22, 3]. Consider the two fields  $E_1$  and  $E_2$  corresponding to the CW and CCW electric fields. A fraction of  $E_2$ ,  $r$ , is scattered into  $E_1$ . Because of the phase difference between  $E_1$  and  $E_2$ , the addition must be done vectorally (see Figure 1.2). Since  $E_1$  must meet the round-trip requirements of a laser, its phase must be adjusted by the amount  $\alpha$  in

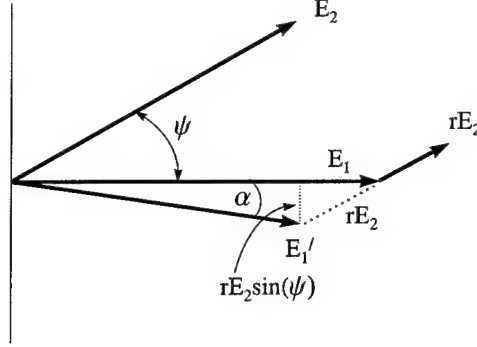


Figure 1.2: Vector change in  $E_1$  as a result of scattering from  $E_2$ .

order to be self-consistent. Therefore the change in phase per round-trip is:

$$\frac{d\psi}{dt} = \Delta\omega = \alpha \frac{c}{P} \quad (1.7)$$

Where  $P$  is the perimeter of the laser and  $\frac{c}{P}$  is the round-trip time. From Figure 1.2 we see that  $\alpha = r \frac{E_2}{E_1} \sin(\psi)$  for small values of  $\alpha$ . Including a rotation rate,  $\Omega$ , with scale factor,  $R$  yields:

$$\Delta\omega = \frac{d\psi}{dt} = R\Omega - r \frac{E_2}{E_1} \sin(\psi) \quad (1.8)$$

A more complete derivation includes the phase of the scattered light,  $\beta$  and the scattered waves from both directions[23, 15, 24] as shown below:

$$\frac{d\psi}{dt} = R\Omega - \Omega_{lock} \sin(\psi + \beta) \quad (1.9)$$

where  $\Omega_{lock} = r \left( \frac{E_2}{E_1} + \frac{E_1}{E_2} \right) \frac{c}{P}$  is the frequency the laser will lock,  $r$  is the field scattering of one mode into the other,  $E_1$  and  $E_2$  are the electric field amplitudes,  $\Omega$  is the rotation rate,  $R = \frac{4A}{\lambda P}$  is the scale factor and  $A$  is the area enclosed. The solution to the nonlinear differential equation can be solved by integration:

$$\int dt = \int \frac{d\psi}{R\Omega - \Omega_{lock} \sin(\psi + \beta)} \quad (1.10)$$

$$t = \frac{-2 \arctan\left(\frac{\Omega_{lock} - R\Omega \tan\left(\frac{\psi + \beta}{2}\right)}{\sqrt{R^2\Omega^2 - \Omega_{lock}^2}}\right)}{\sqrt{R^2\Omega^2 - \Omega_{lock}^2}} \quad (1.11)$$

$$\tan\left(\frac{(\psi(t) + \beta)}{2}\right) = \frac{\Omega_{lock} + \sqrt{R^2\Omega^2 - \Omega_{lock}^2} \tan\left(\frac{t}{2} \sqrt{R^2\Omega^2 - \Omega_{lock}^2}\right)}{R\Omega} \quad (1.12)$$

Figure 1.3 is a plot of the cosine of the phase  $\psi(t)$  for four different rotation rates (A, B, C and D) as defined in Figure 1.5. Note the good qualitative correspondence between the theoretical plot in Figure 1.3 and the experimental results in Figure 1.4. Some experimental

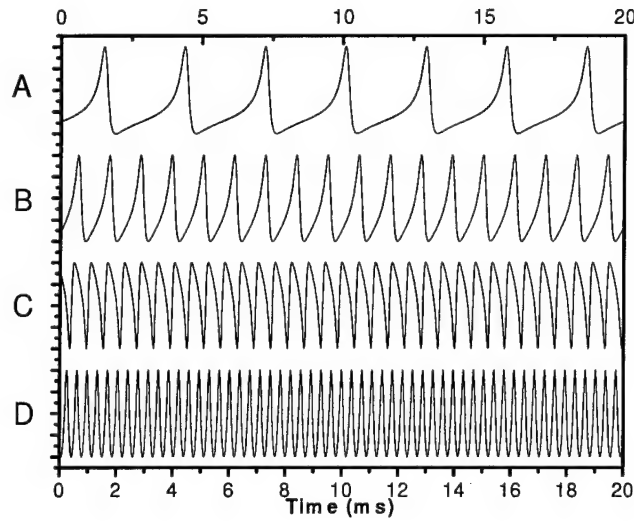


Figure 1.3: Theoretical plot of the beat signal as a function of time. The plots A, B, C and D correspond to data points on the experimental lock-in curve plotted in Figure 1.5.

results demonstrating lock-in are shown in Figure 1.5. The points labeled in Figure 1.5 correspond to the beat signals plotted in Figure 1.4. Notice the non-sinusoidal behavior near lock-in. These data were taken using a Ti:sapphire laser mode-locked with an absorbing dye jet (see Figure 1.6). A bicycle reflector was used to scatter a small portion of the CCW beam into the CW and a LiNbO<sub>3</sub> modulator was used to simulate rotation. The phase of

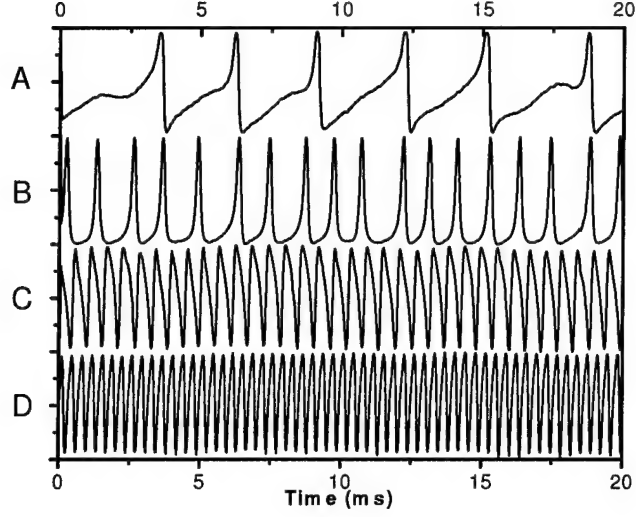


Figure 1.4: Time series of the beat signal at locations A,B, C and D along the lock-in curve.

the scattering,  $\beta$ , plays a critical role in the shape of the beat signal, as can be seen in Figure 1.7. It appears that the bicycle reflector induces a phase change of  $\frac{3\pi}{4}$  in reflection. Far from  $\Omega_{lock}$ , the solution is clearly periodic with frequency:

$$2\pi p \equiv \sqrt{R^2\Omega^2 - \Omega_{lock}^2} \sim R\Omega \quad (1.13)$$

To avoid a plethora of omegas, we will make the substitutions,  $2\pi f \equiv R\Omega$ ,  $2\pi\ell \equiv \Omega_{lock}$  and  $2\pi p = \sqrt{R^2\Omega^2 - \Omega_{lock}^2}$ . Where  $f$  is the unpulled frequency,  $\ell$  is the lock-in frequency and  $p$  is the pulled frequency. By taking the time derivative of the phase, we will find the instantaneous beat frequency. Note that this can be solved by using equation 1.9 and 1.12



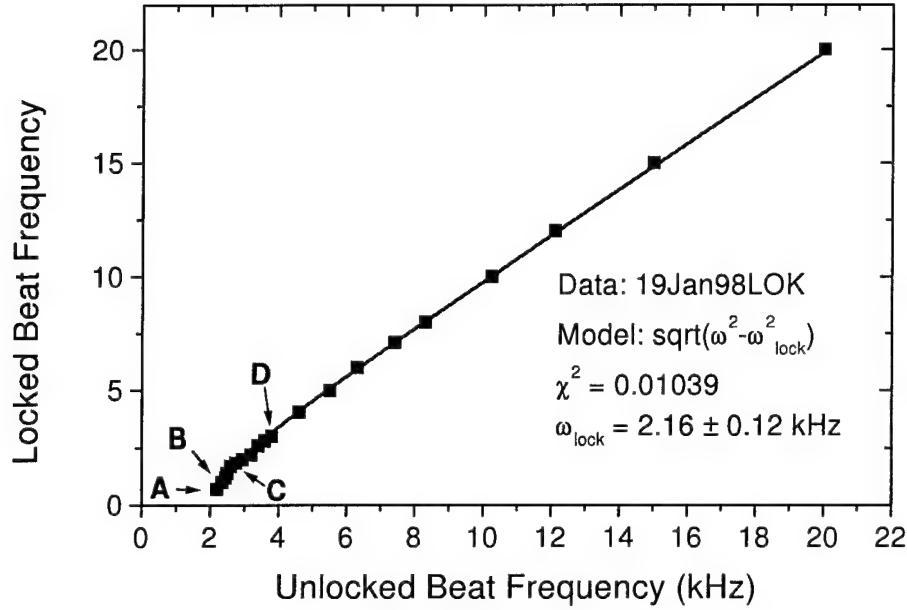


Figure 1.5: Average beat frequency of the laser versus the effective rotation rate.

to yield the instantaneous frequency:

$$\frac{1}{2\pi} \frac{d\psi}{dt} = f_0(t) = \frac{fp^2}{f^2 + \ell^2 \cos(2\pi pt) + \ell p \sin(2\pi pt)} \quad (1.14)$$

$$f_0(t) = \frac{p^2}{f + \ell \left\{ \frac{\ell}{f} \cos(2\pi pt) + \frac{p}{f} \sin(2\pi pt) \right\}} \quad (1.15)$$

$$f_0(t) = \frac{p^2}{f + \ell \{ \cos(\theta) \cos(2\pi pt) + \sin(\theta) \sin(2\pi pt) \}} \quad (1.16)$$

$$f_0(t) = \frac{p^2}{f + \ell \cos(\theta - 2\pi pt)} = \frac{(f - \ell)(f + \ell)}{f + \ell \cos(2\pi \sqrt{f^2 - \ell^2} t - \theta)} \quad (1.17)$$

$$\text{where } \cos(\theta) \equiv \frac{\ell}{f} \text{ and } \sin(\theta) = \frac{\sqrt{f^2 - \ell^2}}{f} \equiv \frac{p}{f} \quad (1.18)$$

From equation 1.17, you can see that the frequency is not constant, but drifts from  $f + \ell$  to  $f - \ell$ . Near  $\ell$  the beat frequency is less periodic and falls to zero at the lock-in frequency. To

calculate the mean frequency, we evaluate the first moment of the instantaneous frequency:

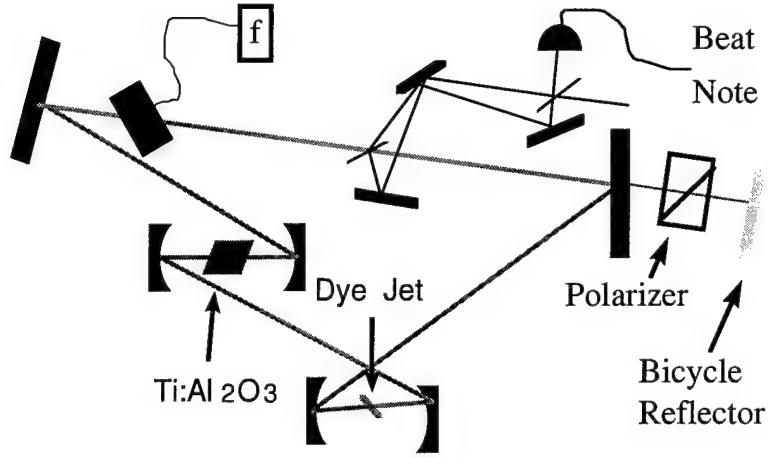


Figure 1.6: Experimental setup for the lock-in experiments. A reflective tape was used to scatter part of the CW beam into the CCW beam.

$$\begin{aligned}
 \langle f_0 \rangle &= \frac{1}{2T} \int_{-T}^T f_0(t) dt \\
 \langle f_0 \rangle &= \frac{1}{2\pi} \int_{-\pi}^{\pi} \frac{p^2}{f + \ell \cos(t')} dt' \\
 \langle f_0 \rangle &= \frac{1}{2\pi} \int_{-\pi}^{\pi} \frac{p^2}{f + \ell \cos(t')} dt' \\
 \langle f_0 \rangle &= \frac{p^2}{2\pi} \int_{-\pi}^{\pi} \frac{1 + \tan^2\left(\frac{t'}{2}\right)}{f \left(1 + \tan^2\left(\frac{t'}{2}\right)\right) + \ell \left(1 - \tan^2\left(\frac{t'}{2}\right)\right)} dt' \\
 \langle f_0 \rangle &= \frac{p^2}{2\pi} \int_{-\pi}^{\pi} \frac{\sec^2\left(\frac{t'}{2}\right)}{f + \ell + (f - \ell) \tan^2\left(\frac{t'}{2}\right)} dt'
 \end{aligned}$$

Let  $y = \tan\left(\frac{t'}{2}\right)$ :

$$\langle f_0 \rangle = \frac{p^2}{2\pi(f - \ell)} \int_{t'=-\pi}^{t'=\pi} \frac{1}{\frac{f + \ell}{f - \ell} + y^2} dy$$

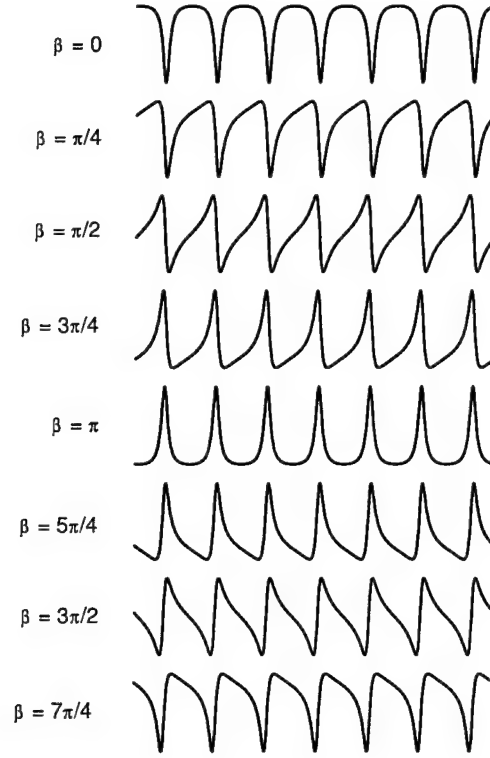


Figure 1.7: Plot of the beat signal as a function of time for 8 different values of  $\beta$ , the scattering phase, in increments of  $\pi/4$ .

Apply the trigonometric substitution:  $\cos \theta = \frac{\sqrt{\frac{f+\ell}{f-\ell}}}{\sqrt{y^2 + \frac{f+\ell}{f-\ell}}}$  yields:

$$\begin{aligned} \langle f_0 \rangle &= \frac{p^2}{\pi(f-\ell) \sqrt{\frac{f+\ell}{f-\ell}}} \int_{t'=-\pi}^{t'=\pi} d\theta \\ \langle f_0 \rangle &= \left[ \frac{p^2}{\pi(f-\ell) \sqrt{\frac{f+\ell}{f-\ell}}} \arctan\left(\frac{\tan(\frac{t'}{2})}{\sqrt{\frac{f+\ell}{f-\ell}}}\right) \right]_{-\pi}^{\pi} = \sqrt{f^2 - \ell^2} = p \end{aligned}$$

Thus we see that the average frequency is less than the linear response,  $f$ . A detection system that records the number of fringes will measure  $p$  and not  $f$ . The average beat frequency,  $p$ , is plotted as a function of  $f$  in Figure 1.8. In a similar manner, we can

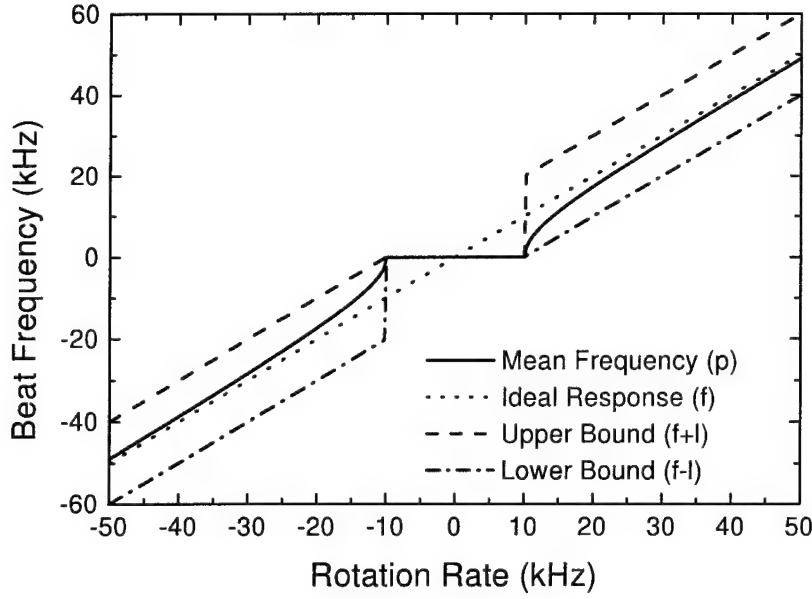


Figure 1.8: The solid line is the mean frequency solution to the lock-in equation with  $\Omega_{lock} = 10$  kHz. The instantaneous frequency varies between the upper and lower bounds.

calculate the second moment:

$$\langle f_2^2 \rangle = \frac{1}{2T} \int_{-T}^T f_0^2(t) dt = fp$$

The standard deviation can be calculated:

$$\begin{aligned} \sigma &= \sqrt{\langle f_2^2 \rangle - \langle f_2 \rangle^2} \\ \sigma &= \sqrt{fp - p^2} \\ \sigma &= \ell \sqrt{1 - \frac{1}{1 + \frac{p}{f}}} = \ell \sqrt{1 - \frac{1}{1 + \frac{\sqrt{f^2 - \ell^2}}{f}}} \\ \sigma &\approx \ell \sqrt{1 - \frac{1}{1 + 1 - \frac{\ell^2}{f^2}}} \approx \frac{\ell}{\sqrt{2}} \end{aligned}$$

This is the linewidth of the instantaneous frequency and simply demonstrates that the instantaneous frequency varies from  $f + \ell$  to  $f - \ell$ . This bandwidth does not effect the bandwidth of the interferogram (the beat signal), which can be seen below, because the beat

signal can be written as a geometric series of complex exponentials similar to the solution for a Fabry-Perot cavity. Regardless of the coupling the first term of the series will have a Fourier component that is a delta function in frequency at the pulled frequency,  $p$ .

A Fourier series analysis of the instantaneous frequency yields Fourier coefficients that follow a geometric progression[22]. Since the instantaneous frequency is purely even, we only need to evaluate the cosine integral:

$$F_n = \frac{1}{\pi} \int_{-\pi}^{\pi} \frac{p^2 \cos(nt')}{f + l \cos(t')} dt'$$

$$F_n = \frac{2p^2}{f\pi} \int_0^{\pi} \frac{\cos(nt')}{1 + \frac{l}{f} \cos(t')} dt'$$

Equation 3.163 from Gradshteyn and Ryzhik is:

$$\int_0^{\pi} \frac{\cos(nx)}{1 + a \cos(x)} dx = \frac{\pi}{\sqrt{1-a^2}} \left( \frac{\sqrt{1-a^2}-1}{a} \right)^n \quad [a < 1, n \geq 0]$$

$$F_n = 2p \left( \frac{f-p}{\ell} \right)^n = 2pr^n \quad (1.19)$$

$$\frac{F_n}{F_0} = r^n$$

Equation 1.19 shows that the harmonics of the beat frequency will follow a geometric series. A linear-log plot of the Fourier transform of the beat signal will follow a straight line, as can be seen in Figure 1.9, a plot of the FFT of plot C of Figure 1.4. From the ratio,  $r$ , we can determine the lock-in frequency,  $\ell = \frac{2pr}{1-r^2}$ . In this example,  $r = .41 \pm .046$ , which leads to a lock-in frequency of  $\ell = 1740 \pm 290$  Hz. This technique will be used to establish an upper bound to the lock-in frequency in Chapters 2 and 3.

### 1.1.3 Dithering

One method to regain linear operation near  $\Omega = 0$  would be to simply apply a bias beat note to the CW or CCW directions, as was first proposed by Killpatrick[25] in 1967. This would avoid the  $\Delta\Omega = 0$  region and would lead to a decoupled laser gyro. Although this is how the decoupling is often described, this is not the most practical method. A more practical method applies an equal, but opposite bias to each direction that periodically

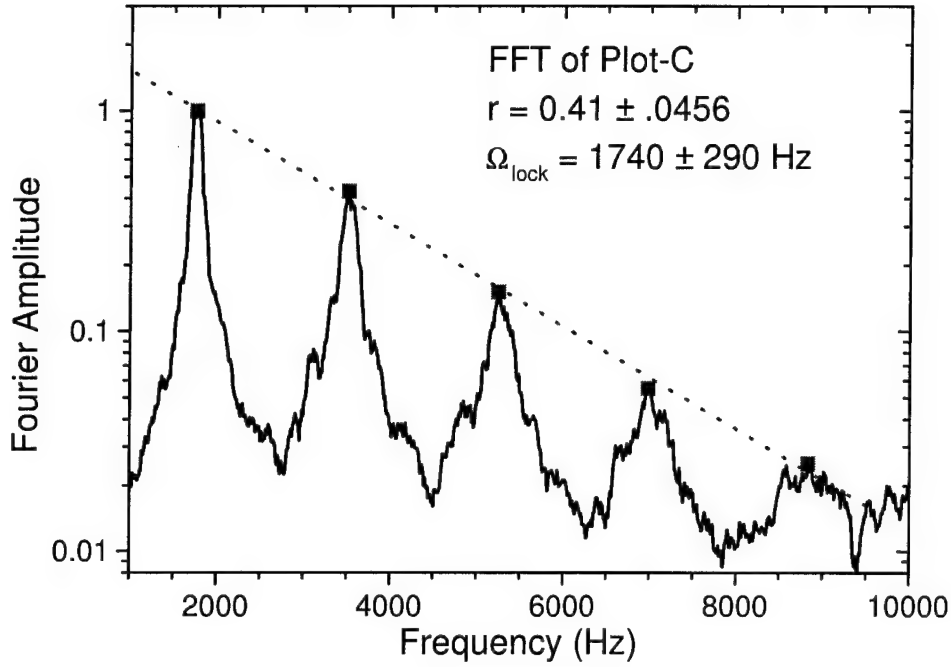


Figure 1.9: FFT of plot C in Figure 1.4. The harmonics of the beat frequency follow a straight line in the log-linear plot because the amplitude of the harmonics are a geometric series.

reverses direction. This leads to an 'average' bias beat note of zero which means the measured beat frequency is once again linear at  $\Omega = 0$ . The beat note when null-bias dithering is applied is shown in Figure 1.10. Notice that the gyro will lock at the dithering frequency and higher multiples of the dithering frequency, as solved analytically by Bambini and Strenholm[26, 27, 28]. This dithering method can be very simply implemented. The laser is mounted via springs to a solid frame. The spring-mass system forms a simple harmonic oscillator which oscillates back and forth. This back and forth motion decouples the laser gyro and gives an average zero beat note[15, 24]. This is typically solved by adding a dithering term to equation 1.9:

$$\frac{d\psi}{dt} = R\Omega - \Omega_{\text{lock}} \sin(\psi + \beta) + C \cos(\Omega_{\text{dither}} t) \quad (1.20)$$

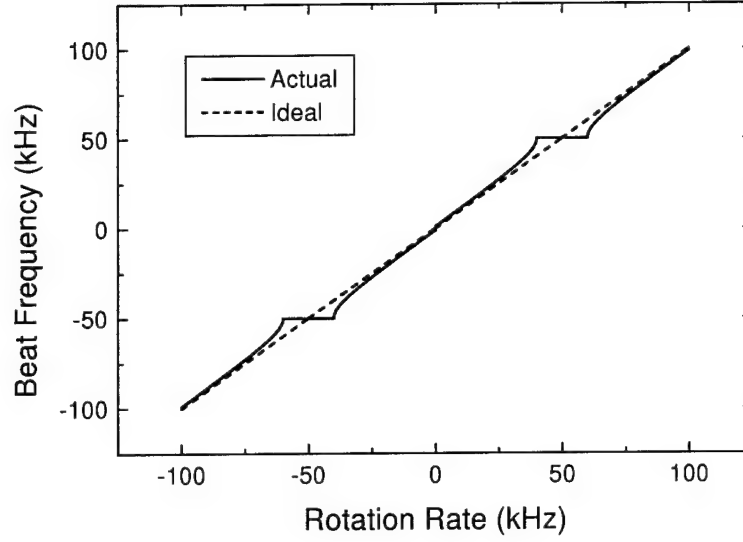


Figure 1.10: Frequency response of a dithered gyro. Nearly linear response is restored near zero; however, when  $\Omega_{rotation} = m\Omega_{dither}$ , the laser will lock again.

This equation describes a direct modulation of the phase of the fields. With the substitution[28]

$$y = \psi - \frac{C}{\Omega_{dither}} \sin(\Omega_{dither}t) \quad (1.21)$$

into equation 1.20, the equation becomes:

$$\frac{dy}{dt} = R\Omega - \Omega_{lock} \sin\left(y + \frac{C}{\Omega_{dither}} \sin(\Omega_{dither}t)\right) \quad (1.22)$$

Now the equation describes a phase modulation of the scatterer. A similar dithering of the phase of the scatterer happens in the absorbing dye jet of a mode-locked ring dye laser and explains why such a laser does not lock. The difference is that, in the case of an absorber dye jet, the scattering is a random rather than harmonic modulation. With this substitution, all of the theoretical calculations for dithering can also be applied to the case of the dye jet which causes a random dithering of the phase of the scatterer.

Honeywell Corporation, in a private communication, uses a mechanical random dither in their commercial laser gyros. The average value of the dither is designed to be zero, similar to the null-bias dithering, in order to prevent a bias beat note. The randomness of

the dithering frequency restores linearity of the laser gyro at all frequencies. The design of a ring laser gyro that is mechanically driven by random amounts is extremely difficult because there will always be mechanical resonances. In addition, it is difficult to prevent a broad spectrum of mechanical motion from exciting resonator modes. The random dither[29] and quantum noise[30, 31] have both been solved analytically by the methods of the Cayley matrix formulation, the Langevin equation, and infinite matrices; respectively.

A less reliable method to dither a ring laser gyro is to use the Faraday effect, also called the magnetic mirror[32]. This method is less reliable because it is difficult to accurately control the magnetic fields in the rotator.

The lock-in beat frequency is independent of the scale factor. Therefore, for a large enough gyro, the rotation rate of the earth is in the 100 Hz range. If the internal scattering can be reduced to  $|r|^2 < 10^{-16}$ , the earth's rotation can unlock the gyro. Of course it is not possible to eliminate the gain medium, but the laser mirrors can be manufactured to have low scattering. Super-mirrors with  $|r|^2 < 10^{-18}$  were used at the University of Canterbury in New Zealand in a large area ( $A \sim 1 \text{ m}^2$ ) with excellent results[3]. Stedman et al.[6, 33, 22, 34, 7] have reduced the coupling to the point that the rotation rate of the earth is enough to decouple the CW and CCW modes. They have measured the earth's rotation rate to within a bandwidth of 100 nHz. They have also been able to measure the effect of tides on the earth's rotation rate and have measured earthquakes on the other side of the world[5].

#### 1.1.4 Optimizing the modulation frequency in a dithered laser gyro

Because HeNe laser gyros depend on a mechanical method of dithering, there are mechanical limitations to the modulation frequency. Because a pulsed laser gyro can be easily dithered using an electro-optic modulator, it is simple to explore a large bandwidth of dithering frequencies. In Chapter 2 the dithering of a pulsed laser gyro will be explored both experimentally and theoretically. The results of these experiments have lead to some interesting theoretical discoveries by using Fourier transforms. These results will be discussed in more



detail in Chapter 2.

### 1.1.5 Pulsed laser gyro

Another method to eliminate the coupling between the CW and CCW modes is to make the system pulsed and then insure that the pulses cross in a medium with low scattering (i.e. air or vacuum). A 100 femtosecond pulse is only 30  $\mu\text{m}$  long, so the scattering from the CW mode into the CCW mode can only occur in a region of roughly 60  $\mu\text{m}$ . The lock-in equation is modified for the pulsed laser[35]:

$$\frac{d\psi}{dt} = R\Omega - e^{-\left(\frac{\tau'}{\tau_p}\right)^2} \Omega_{lock} \sin(\psi + \beta) \quad (1.23)$$

where  $\tau'$  is the time difference between the scatterer and the pulse crossing point and  $\tau_p$  is the pulsewidth. It should then be trivial to design a laser cavity that has crossing points only in air. There is; however, a need for an amplitude coupling mechanism that defines the pulse crossing point; a point that has to be imaged onto a detector. This amplitude coupling should not introduce any phase coupling. Mutual saturation in an absorbing dye jet does provide the required amplitude coupling. Even though a scattering coefficient of  $r = 10^{-3}$  was measured for a pure ethylene glycol jet, the laser does not lock. The motion of the dye randomizes the phase of the scatterer, which unlocks the laser(see equation 1.22). When the laser is mode-locked using an absorbing glass, the CW and CCW pulses did lock; thus supporting the claim that it is the motion of the scatterers which decouples the CW and CCW modes. The four-wave mixing[36] in the jet might help to equilibrate the amplitudes of the CW and CCW pulses by phase-conjugate coupling[21]. Recall that in equation 1.9 that  $\Omega_{lock}$  included a term of  $\frac{E_1}{E_2} + \frac{E_2}{E_1}$ , clearly if  $E_1 = E_2$  the lock-in frequency will be reduced.

**Two-beam coupling** Consider the possible four-wave mixing polarizations that can occur as a result of two beams with frequencies  $\omega_1$  and  $\omega_2$  counter-propagating in a medium with a non-resonant third-order susceptibility  $\chi^{(3)}$ :

$$P(\omega_1) = \chi^{(3)} (3E_1 E_1^* + 6E_2 E_2^*) E_1 \quad (1.24)$$

$$P(\omega_2) = \chi^{(3)} (6E_1 E_1^* + 3E_2 E_2^*) E_2 \quad (1.25)$$

$$P(2\omega_1 - \omega_2 = \omega_1 + \Delta) = 3\chi^{(3)} E_1^2 E_2^* \quad (1.26)$$

$$P(2\omega_2 - \omega_1 = \omega_2 - \Delta) = 3\chi^{(3)} E_2^2 E_1^* \quad (1.27)$$

$$\Delta = \omega_1 - \omega_2 \quad (1.28)$$

$$P(3\omega_1) = \chi^{(3)} E_1^3 \quad (1.29)$$

$$P(3\omega_2) = \chi^{(3)} E_2^3 \quad (1.30)$$

Equations 1.29 and 1.30 are third-harmonic generation. Equations 1.24 and 1.25 are intensity dependent changes in the index of refraction. And equations 1.26 and 1.27 are the phase-conjugate scattering terms. Notice that the frequency is shifted and that the field is conjugated. It can be shown that the two beams only couple power into one another if  $\chi^{(3)}$  is imaginary[37] and the only terms that contribute are 1.26 and 1.27. An imaginary  $\chi^{(3)}$  is a result of a finite response time of the medium. The finite response time will cause a slight phase shift in the moving index grating with respect to the fields,  $E_1$  and  $E_2$ . Equations 1.24 and 1.25 will be used in Chapter 3 in the discussion of mutual Kerr-lens mode-locking.

Although the pulsed laser gyro offers a unique solution to the lock-in problem, it also creates additional problems such as an arbitrary bias beat note. This arbitrary bias is a result of nonlinearities in the laser cavity. A simple example is to consider the cavity shown in Figure 1.11. Note that the CW pulse is incident in the saturable absorber with intensity  $\alpha I_0$  while the CCW pulse has intensity  $I_0$  at the saturable absorber. Since the saturable absorber is an intensity dependent element, there will be a nonreciprocal effect because of the different intensities. This is a simple example that could perhaps be corrected by a judicious use of output coupling to compensate the different intensities. Perhaps a more relevant example is the Kerr effect. Because of the Kerr effect, any difference in intensities between the CW and CCW pulses will result in a bias beat note because the intensity dependent index of refraction will result in a change in cavity length.

Although the randomizing of the phase of the scattering in the dye jet prevents lock-in, the amplitude fluctuations in the laser is significantly worse than a solid-state laser. The

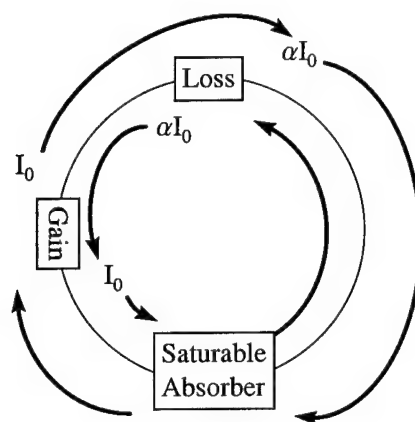


Figure 1.11: Schematic of ring laser with nonreciprocal intensities at the saturable absorber.

noise characteristics of a solid-state laser in comparison to an Argon ion-dye laser has been well documented[38, 39, 40, 41]. The reason the solid-state laser is less noisy is because the lifetime of the dye is about 1 ns and the lifetime of Ti:sapphire is 3  $\mu s$ . The longer lifetime integrates any fluctuations of the pump, in addition a solid-state pump laser is less noisy than an Argon ion laser.

Because our group is interested in studying nonlinear intracavity effects using pump/probe experiments, high output powers are required. Typically a dye laser is capable of only a few milliwatts. For these reasons, the Ti:sapphire laser is the next logical step in the evolution of the pulsed laser gyro. Before going on to discuss the Ti:sapphire laser in more detail, we need to mention that there are at least two other solid-state laser gyros...

### 1.1.6 Other solid-state laser gyros

The competing technologies in the race for a practical solid-state ring laser gyro are diode lasers and fiber lasers. The diode laser had problems with noise from the power supply[14]. Because diode lasers use gain switching to actively mode-lock the device, they required a very good, fast power supply (see Figure 1.12). Christian and Rosker also report a nonreciprocal response in the device, which is to be expected because of the direct relationship between gain and index in semiconductors through the alpha parameter[42]. The smallest beat note

they were able to measure was 20 kHz. What was most disturbing about this ring laser gyro was that the scale factor varied with alignment. They report that the scale factor could vary from 20 kHz to 500 kHz depending on the alignment of the etalons. It would be impossible to use such a device for a ring laser gyro unless they were able to fix the scale factor.

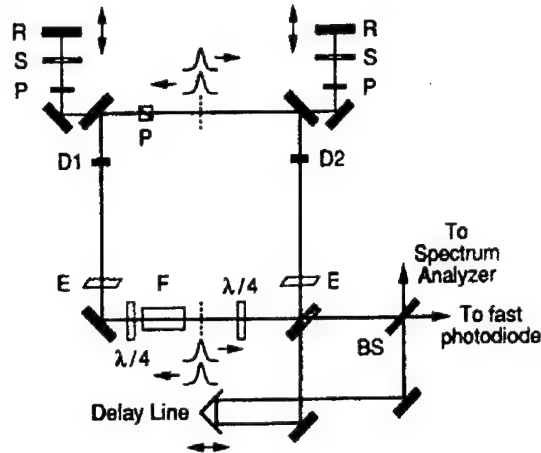


Figure 1.12: Laser diode ring gyroscope. The diodes are actively modelocked by gain switching. The R, S and P were used to induce coupling in the device.

The fiber laser shown in Figure 1.13 is a continuous wave laser that is decoupled by frequency shifting the CW beam by 0.1 MHz to 12.5 MHz from the CCW beam[43]. What is remarkable about this ring laser gyro is the 100 Hz bandwidth. Their study was inconclusive about how much dither needs to be applied to prevent lock-in. Nor did they discuss the linearity of the device to rotation.

## 1.2 Soliton-like pulse shaping

In order to build a pulsed Ti:sapphire ring laser gyro, we also need to have a solid foundation in short pulsed lasers. The soliton model is a good place to start, although for sub-10 fs pulses its validity is currently in dispute[44, 45]. In the Ti:sapphire laser the most important parameter to consider when making a femtosecond laser is the group velocity dispersion (GVD). However, if you wish to build a sub-10 fs laser then you must also consider the

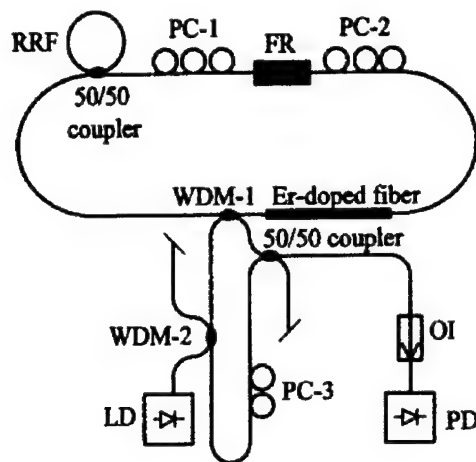


Figure 1.13: The continuous wave fiber ring laser. The Faraday rotator in between the polarizers generates a bias beat note to prevent lock-in.

third and fourth order dispersion (TOD and FOD). The explanation for this is found in the soliton model of a laser pulse. Because this model is paramount to understanding the Ti:sapphire laser, a brief discussion is included.

### 1.2.1 Historical

In 1834, Scott-Russell recorded the first soliton wave:

“I was observing the motion of a boat which was rapidly drawn along a narrow channel by a pair of horses, when the boat suddenly stopped—not so the mass of water in the channel which it had put in motion; it accumulated round the prow of the vessel in a state of violent agitation, then suddenly leaving it behind, rolled forward with great velocity, assuming the form of a large solitary elevation, a rounded, smooth and well-defined heap of water, which continued its course along the channel apparently without change of form or diminution of speed. I followed it on horseback, and overtook it still rolling on at a rate of some eight or nine miles an hour, preserving its original figure some thirty feet long and a foot to a foot and a half in height. Its height gradually diminished, and after a chase of one or two miles I lost it in the windings of the channel. Such, in the

month of August 1834, was my first chance interview with that singular beautiful phenomenon... .”

This colorful definition of a soliton is still accurate. A soliton is only loosely defined by its two properties 1) a localized wave that does not change in shape or velocity, and 2) the collision of two solitons will not change their shape or velocity[46]. Because the elements of GVD and SPM are separated in the Ti:sapphire laser, the pulse shape varies throughout the laser. Often the pulses in the Ti:sapphire laser are called 'soliton-like' because many of their properties are determined by the soliton model even though they are not true solitons.

Optical fibers and ultra-short pulse lasers are two applications of soliton theory in the optics and laser community. It was not until 1980 that Mollenauer et al.[47] discovered solitons in optical fibers. Researchers are still designing the final components of the fiber optic soliton communication system which includes: soliton routing switches[48], and digital logic gates [49]. The application of the soliton model to ultra-short pulse Ti:sapphire lasers will be the focus of the remainder of this discussion.

Several breakthroughs in the mid-1980s set the stage for  $\sim 10$  femtosecond soliton pulses: 1) Dye lasers solidified the soliton theory and how self-phase modulation and group velocity dispersion must work together in the formation of ultra-short pulses[50, 51] 2) The discovery of Ti:sapphire as a laser material with a gain bandwidth of 100 THz [52] and 3) the discovery of negative group dispersion velocity in prism pairs[53]. By 1992 many groups around the world have been producing femtosecond laser pulses and 'solitons' are becoming a vernacular of the laser community[54, 55, 56, 57, 58, 59]. Today the Ti:sapphire laser is at the limit of the soliton model that includes only group velocity dispersion (GVD) and self-phase modulation (SPM). Higher order effects (i.e. third order dispersion (TOD) and fourth order dispersion (FOD)) are becoming the limiting factor for ultra-short pulses in most lasers [58, 60, 61, 62]. Although the current soliton model does not include these terms, it is my opinion that theories will be developed to include these higher order effects[63, 61, 62, 64]. Since GVD and SPM are so crucial to soliton formation, let's take a look at GVD and SPM before discussing the soliton model.

### 1.2.2 Theory: wave equation and group velocity dispersion

The wave equation can be developed from Maxwell's equations:

$$\nabla^2 E - \frac{1}{c^2} \frac{\partial^2 E}{\partial t^2} = \frac{1}{e_0 c^2} \frac{\partial^2 P}{\partial t^2} \quad (1.31)$$

Then the Classical Electronic Oscillator (CEO) model can be used to find the material polarization ( $P$ ). The polarization is related to material properties by:  $P = \epsilon_0 (n^2(\omega) - 1) E$ . The CEO model predicts Lorentzian-shaped absorption lines and roughly the derivative of a Lorentzian for the index of refraction  $n(\omega)$ . Figure 1.14 is a plot of the index of refraction as a function of frequency near a resonance.

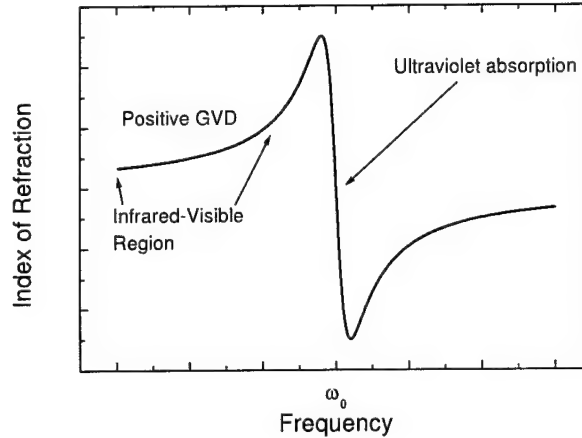


Figure 1.14: Typical Lorentzian dispersion curve near a resonance. Most glasses have positive GVD in the visible-infrared region because of an ultraviolet absorption edge.

From the graph above we can see that dispersion is a function of frequency, which means that the velocity (because  $v = \frac{c}{n(\omega)}$ ) in this material is a function of frequency. If a pulse of light is sent through a medium with negative dispersion, the lower frequency components will travel slower than the high frequency components; thus causing the pulse to spread. This effect is called Group Velocity Dispersion (GVD). Figure 1.15 demonstrates pulse spreading in a medium with GVD[65].

Let's define GVD mathematically. Milonni and Eberly define the wavevector as 'k' but many publications (Siegman) also use 'β':  $k^2 = n^2(\omega) \frac{\omega^2}{c^2} = \beta^2$ . At any single frequency, 'k'

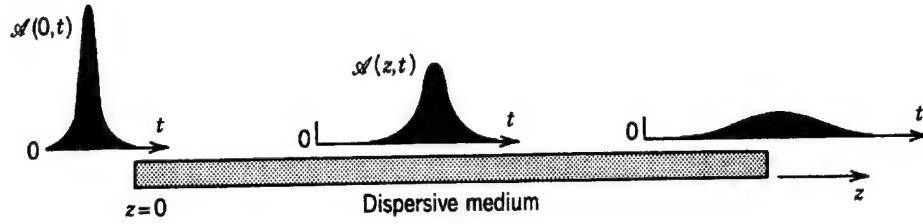


Figure 1.15: Broadening of a pulse in a dispersive medium.

will determine how the field propagates. If we are considering a distribution of frequencies (a pulse by definition of the Fourier transform must contain many frequencies), then the propagation of the fields will be a complicated function of frequency. To simplify the analysis, we can Taylor expand the wavevector about the carrier frequency  $\omega_0$  :

$$k(\omega) = k(\omega_0) + (\omega - \omega_0) \left. \frac{dk(\omega)}{d\omega} \right|_{\omega_0} + \frac{1}{2} (\omega - \omega_0)^2 \left. \frac{d^2k(\omega)}{d\omega^2} \right|_{\omega_0} \quad (1.32)$$

$$k(\omega) = k(\omega_0) + (\omega - \omega_0)k' + \frac{1}{2} (\omega - \omega_0)^2 k'' \quad (1.33)$$

where phase velocity  $\Rightarrow v_p = \frac{\omega_0}{k(\omega_0)}$ ,

$k'$  is related to the group velocity:  $k' = \left. \frac{dk(\omega)}{d\omega} \right|_{\omega=\omega_0} = \frac{1}{v_g}$

and  $k''$  is the group velocity dispersion  $k'' = \left. \frac{d^2k(\omega)}{d\omega^2} \right|_{\omega=\omega_0} = -\frac{1}{v_g^2} \left. \frac{dv_g}{d\omega} \right|_{\omega=\omega_0}$

In this simple CEO model, we can see that the GVD will be positive at frequencies below a resonance. Therefore we expect most glasses (which typically have resonances in the UV) to have a positive GVD in the visible spectrum. Positive GVD for glasses is verified by the literature[65]. The coefficients above are typically found experimentally.

Clearly if dispersion exists inside a laser cavity, GVD will limit the pulse width. If we are designing a short pulse laser, we should limit the amount of dispersive material in the cavity. However a certain amount of dispersive material will exist in all lasers. In a Ti:sapphire laser the sapphire itself is dispersive. It would appear that short pulses and lasers are incompatible. But what if the frequency varied throughout the pulse? If the slower, low frequency components preceded the faster, higher frequency components (in a medium with negative GVD); we would see the trailing edge of the pulse “catch-up” with the leading edge



of the pulse resulting in pulse compression. This effect is dependent on the rate of change of the frequency (called chirp) and on the amount of dispersion. Figure 1.16 below illustrates a pulse with negative chirp (frequency decreases with time) propagating in a medium with positive GVD. Notice the pulse initially compresses, but then expands as it propagates through more dispersive material[65]. This effect has recently been used to incorrectly claim pulse compression in quasi-phased matched OPOs[66](true pulse compression compares only bandwidth limited pulses). The effect is the same if we propagate a positive chirped pulse through a medium of negative GVD.

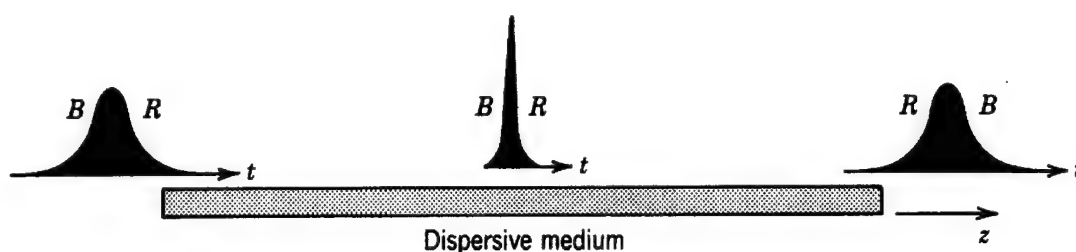


Figure 1.16: Negatively chirped pulse traveling through a medium of positive dispersion. The pulse initially compresses and then spreads.

How do pulses become chirped in a laser? This question will be answered in the next section.

### 1.2.3 Self-phase modulation (chirp)

The classical electron oscillator model yields good results for linear interactions, but for soliton formation we need to perturb the harmonic potential and use the anharmonic oscillator model. The anharmonic model includes nonlinear effects. This model predicts a term in the index of refraction that goes as  $|E|^2$  and is called the third-order susceptibility ( $\chi^3$ ). This term is responsible for many of the nonlinear effects in optics including: self-phase modulation, self-focusing, bistability, four-wave mixing and third-harmonic generation. We can go back to the classical electron oscillator model and simply replace  $n \Rightarrow n + n_2 |E|^2$ . To understand what  $n_2$  will do to a pulse let's consider a Gaussian pulse,  $E(t) = E_0 e^{i\omega_0 t - at^2} = E_0 e^{i(\phi(t))}$ , propagating a distance,  $L$ , through a nonlinear

medium. After propagating a distance  $L$  (remember that:  $\omega_0 t = 2\pi n_0 \frac{L}{\lambda}$ ) the phase will be:  $\phi(t) = \omega_0 t - 2\pi n_2 |E(t)|^2 \frac{L}{\lambda}$ . The derivative of the phase shift is approximately:

$\frac{d}{dt}\phi(t) = \omega_0 - 8\pi n_2 |E_0|^2 \frac{L}{\lambda} t e^{-2at^2} = \omega_0 - 8\pi n_2 |E(t)|^2 \frac{L}{\lambda} t$ . Near the peak ( $t = 0$ ) of the pulse the frequency has a component that is changing approximately linear in time:  $\omega(t) = \frac{d}{dt}\phi(t) = \omega_0 - 8\pi n_2 |E_0|^2 \frac{L}{\lambda} t$  this is called a chirped pulse. If  $n_2 > 0$ , SPM causes a negative frequency shift in the leading half of the pulse and a positive frequency shift on the trailing edge. In illustration 1.17 we see an unchirped pulse propagate through a nonlinear medium and become chirped [65]. Notice that SPM does not change the pulse width.

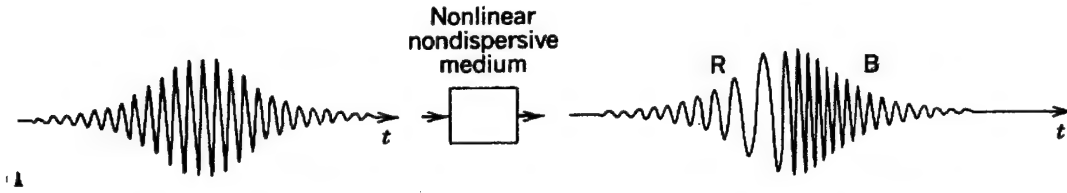


Figure 1.17: Demonstration of Self-Phase Modulation (SPM) resulting in a chirped pulse.

When a pulse becomes chirped as a result of its intensity distribution, this process is called Self-Phase Modulation (SPM). We have seen how SPM can chirp a pulse and we have seen how GVD can compress a chirped pulse, but can the two effects really interact synergistically to produce an ultra-short pulsed laser?

### 1.2.4 Soliton solution

To answer the question above we return to the wave equation and add the two effects we discussed above. This new equation is called the Nonlinear Schrödinger equation (NLSE)[65, 67]. The derivation of the NLSE follows the outline given in Boyd[37]. Assume an electromagnetic pulse traveling in the  $z$ -direction of the form:

$$E(z, t) = A(z, t)e^{i(k_0 z - \omega_0 t)} \quad (1.34)$$

We propagate this pulse through a dispersive, nonlinear medium. The pulse must obey the wave equation:

$$\frac{\partial^2 E(z, t)}{\partial z^2} - \frac{1}{c^2} \frac{\partial^2 D(z, t)}{\partial t^2} = 0 \quad (1.35)$$

Where  $D$  contains both the linear and nonlinear response of the medium. Define the Fourier transforms of  $E(z, t)$  and  $D(z, t)$ :

$$E(z, t) = \frac{1}{2\pi} \int_{-\infty}^{\infty} \tilde{E}(z, w) e^{-iwt} dw \quad (1.36)$$

$$D(z, t) = \frac{1}{2\pi} \int_{-\infty}^{\infty} \tilde{D}(z, w) e^{-iwt} dw \quad (1.37)$$

Remember that  $D$  and  $E$  are related by:

$$\tilde{D}(z, w) = \epsilon(w) \tilde{E}(z, w) \quad (1.38)$$

Substitute equations 1.36, 1.37 and 1.38 into the wave equation:

$$\frac{\partial^2 \tilde{E}(z, w)}{\partial z^2} + \epsilon(w) \frac{w^2}{c^2} \tilde{E}(z, w) = 0 \quad (1.39)$$

Since we are only concerned with the evolution of the envelope of the pulse, we need to take the Fourier transform of equation 1.34 and substitute the result into equation 1.39.

$$E(z, t) = \int_{-\infty}^{\infty} A(z, t) e^{i(k_0 z - w_0 t)} e^{iwt} dt \quad (1.40)$$

$$E(z, t) = e^{ik_0 z} \int_{-\infty}^{\infty} A(z, t) e^{it(w - w_0)} dt \quad (1.41)$$

$$E(z, t) = e^{ik_0 z} \tilde{A}(z, w - w_0) \quad (1.42)$$

where  $\tilde{A}(z, w)$  is the Fourier transform of  $A(z, t)$ . The wave equation in terms of  $\tilde{A}(z, w - w_0)$  :

$$\frac{\partial^2}{\partial z^2} e^{ik_0 z} \tilde{A} + \epsilon(w) \frac{w^2}{c^2} \tilde{A} e^{ik_0 z} = 0 \quad (1.43)$$

$$2ik_0 e^{ik_0 z} \tilde{A} + e^{ik_0 z} \frac{\partial^2 \tilde{A}}{\partial z^2} - k_0^2 \tilde{A} e^{ik_0 z} + \epsilon(w) \frac{w^2}{c^2} \tilde{A} e^{ik_0 z} = 0 \quad (1.44)$$

Since  $\tilde{A}(z, w - w_0)$  is a slowly varying envelope, we drop  $\frac{\partial^2 \tilde{A}}{\partial z^2}$ . From electromagnetic theory, we can identify  $k^2(w) = \epsilon(w) \frac{w^2}{c^2}$  and cancel common exponential terms.

$$ik_0 \frac{\partial \tilde{A}(z, w - w_0)}{\partial z} + (k^2 - k_0^2) \tilde{A}(z, w - w_0) = 0 \quad (1.45)$$

Because self-phase modulation and dispersion are considered small perturbations, we can make the approximation that  $k^2 - k_0^2 = 2k_0(k - k_0)$ .

$$\frac{\partial \tilde{A}(z, w - w_0)}{\partial z} - i(k - k_0) \tilde{A}(z, w - w_0) = 0 \quad (1.46)$$

Next Taylor expand  $k(w)$  about  $w_0$  and include the nonlinear term:

$$k(w) = k_0 + n_2 I \frac{w_0}{c} + k'(w - w_0) + \frac{1}{2} k''(w - w_0)^2 \quad (1.47)$$

Where,  $I$ , is the intensity  $I = \frac{nc}{2\pi} |A(z, t)|^2$ . Finally we make the change in variables  $\Delta = (w - w_0)$ , substitute equation 1.47 into 1.46 and take the inverse Fourier transform,  $\mathcal{F}^{-1}$ .

$$\mathcal{F}^{-1} \left[ \frac{\partial \tilde{A}(z, \Delta)}{\partial z} - in_2 I \frac{w_0}{c} \tilde{A}(z, \Delta) - ik' \Delta \tilde{A}(z, \Delta) - i \frac{k''}{2} \Delta^2 \tilde{A}(z, \Delta) = 0 \right] \quad (1.48)$$

The inverse Fourier transforms are:

$$\mathcal{F}^{-1} [\tilde{A}(z, \Delta)] = A(z, t) \quad (1.49)$$

$$\mathcal{F}^{-1} [\Delta \tilde{A}(z, \Delta)] = i \frac{\partial A(z, t)}{\partial t} \quad (1.50)$$

$$\mathcal{F}^{-1} [\Delta^2 \tilde{A}(z, \Delta)] = -\frac{\partial^2 A(z, t)}{\partial t^2} \quad (1.51)$$

Substitution of these inverse Fourier transforms yield:

$$\frac{\partial A(z, t)}{\partial z} - in_2 I \frac{w_0}{c} A(z, t) + k' \frac{\partial}{\partial t} A(z, t) + i \frac{k''}{2} \frac{\partial^2}{\partial t^2} A(z, t) = 0 \quad (1.52)$$

Next we make a Galilean Boost transformation and recall that  $I = \frac{nc}{2\pi} |A(z, t)|^2$ . Boost  $\Rightarrow \tau = t - \frac{z}{v_g}$

$$\frac{\partial A(z, \tau)}{\partial z} + i \frac{k''}{2} \frac{\partial^2}{\partial t^2} A(z, \tau) = i \frac{nn_2 w_0}{2\pi} |A(z, \tau)|^2 A(z, \tau) \quad (1.53)$$

Equation 1.53 is known as the nonlinear Schrödinger equation. This form is typically found in the optics community, but it is not truly in the form of the nonlinear Schrödinger equation. If the change in variables is done slightly differently, we can obtain the NLSE with appropriately scaled wavefunctions:

$$\begin{aligned}
\tau &= \frac{\left(t - \frac{z}{v_g}\right)}{\tau_0} \\
\xi &= \frac{|k''|}{\tau_0^2} z \\
\psi(\xi, \tau) &= \tau_0 \sqrt{\frac{wn_2 n}{2c |k''|}} A(z, t)
\end{aligned} \tag{1.54}$$

Where  $\tau_0$  is the pulse width and  $\psi(\xi, \tau)$  is the wave function.

$$i \frac{\partial \psi(\xi, \tau)}{\partial \tau} + \frac{1}{2} \frac{\partial^2}{\partial \tau^2} \psi(\xi, \tau) + |\psi(\xi, \tau)|^2 \psi(\xi, \tau) = 0 \tag{1.55}$$

The NLSE was originally solved by Zakharov and Shabat[68] in 1972. The solutions are solitons in terms of the field envelope:

$$A(z, t) = A_0 \operatorname{sech} \left( \frac{t - \frac{z}{v_g}}{\tau_0} \right) e^{-i \frac{k''}{2\tau_0^2} z} \tag{1.56}$$

The coefficients are defined as:  $\tau_0 \equiv$  pulse width,  $|A_0|^2 = \frac{-2\pi k''}{nn_2\omega_0\tau_0^2} \equiv$  amplitude of envelope of electric field,  $v_g \equiv$  group velocity, and  $k'' =$  group velocity dispersion. Note for  $A_0$  to be real and positive,  $k''$  and  $n_2$  must be of opposite sign. Since  $n_2$  is positive for Ti:sapphire, we require that  $k''$  be negative. The boost transformation simply puts us in the reference frame of the pulse. You can imagine yourself riding on top of the soliton wave like a surfer riding a tsunami. Thus we see that when SPM and GVD act together and their coefficients obey  $n_2 > 0$  and  $k'' < 0$ ; there is a stable solution that does not spread in time or frequency. Notice that the measurable quantity, intensity, goes as  $\operatorname{sech}^2()$ . This function is often used in the literature to characterize ultra-short pulses. The coefficient  $n_2$  is positive for Ti:sapphire, but  $k''$  is also positive! How do we achieve a negative value for GVD?

A revolutionary optical technique was developed by several groups[50, 53]. They proposed and verified that by sequencing two prisms with positive GVD a net negative GVD could be engineered, see Figure 1.18. This basic method for obtaining negative GVD is used in almost all ultra-short pulse Ti:sapphire lasers. The experimental setup shown in

Figure 1.18 was typical until the advent of doubly chirped mirrors[69, 70]. These mirrors have negative GVD designed into their layers and are able to eliminate the need for GVD compensating prisms. Initially the laser needs some sort of 'kick' to generate a short

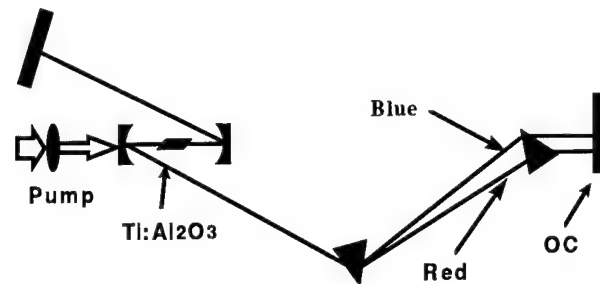


Figure 1.18: Typical Kerr-lens modelocked Ti:sapphire laser. The radius of curvature of mirrors is 10 cm concave. The prism sequence has a net negative GVD to compensate for the GVD of the Ti:sapphire. Notice the 'red' ray travels through more glass which delays it with respect to the 'blue' ray.

modulation. One of the most innovative techniques to initiate mode-locking is the use a solid-state saturable absorber[71, 72, 73]; in fact, this method has produced the shortest pulses in a Ti:sapphire laser. Once the pulse is in the picosecond range the soliton model takes over and the GVD/SPM effects compress the pulse to its limits, which is usually determined by third order dispersion. A second very important pulse width limiting process occurs because the nonlinear and dispersive effects are physically separated. The nonlinear Schrödinger equation is a differential equation. The infinitesimal approximation does not apply in the Ti:sapphire laser when the change/element is large. In this case a difference equation approach is more appropriate[74]. The pulse shape will be a strong function of its location in the laser and what components it has propagated through. Some researchers believe this is the most important limiting effect[57]. When you consider that the model was developed with the assumption that the nonlinear and dispersive effects were slowly varying and continuous; it is not surprising that the model might fail when the pulses become a

few tens of femtoseconds in width. There have been some interesting experiments done to demonstrate how the pulse changes as it propagates through the different components in the laser[59, 60]. To conclude; we have seen how group velocity dispersion can compress chirped pulses and how pulses can become chirped by a nonlinear medium. Finally we have combined the two effects, and discovered the nonlinear Schrödinger equation. The nonlinear Schrödinger equation was seen to have soliton solutions that do not decay or expand as they propagate.

### Kerr-lens mode-locking

Soliton-like pulse-shaping stabilizes a short pulse in a laser cavity, but what causes the pulse-shortening? Typically a fast saturable absorber is needed for pulse shortening. In the sub-picosecond region the possibilities are: Kerr-Lens mode-locking(KLM), Semiconductor Saturable Absorber Mirror(SESAM[72]), Additive Pulse mode-locking (APM) and Colliding Pulse mode-locking(CPM). Of these only the first three can be used in Ti:sapphire. APM is not stable because it requires an interferometer. SESAM requires specially made semiconductor materials that we are exploring, but as of yet these are unavailable. This leaves KLM, which is by far the cheapest way to mode-lock a laser because it requires no additional components. The Kerr-lens is the result of a nonlinear refractive index ( $\chi^3$ ) effect. It is the same physical mechanism that was used to generate SPM. KLM is a spatial effect that is a result of the intensity being a function of the beam radius; whereas SPM is a result of the pulse intensity being a function of time. To first order, the nonlinear index can be approximated with a thin lens of focal length,  $f_{nl}$ .

$$f_{nl} = \frac{n_0 \pi \omega_0^4}{8 n_2 P d} \quad (1.57)$$

Using the ABCD matrix method for the cavity, it is easy to determine locations in the cavity where the pulsed beam waist will be smaller than the continuous-wave beam waist. An aperture at this location will create a nonlinear loss that favors short-pulse operation. Often the Gaussian profile of the gain can be used as a 'soft aperture.' Apodized slits can also provide a smooth aperture. If razor slits are used, it is called a 'hard aperture.' The modeling of the cavity is discussed in more detail in Chapter 3. The rest of this dissertation

deals with the daunting task of merging a ring laser and a short pulsed solid-state laser.



## Chapter 2

# Saturable Absorber Mode-locked Ti:sapphire Laser

Although the saturable absorber is used in the femtosecond dye laser, this is the first time, to our knowledge, where it is used to mode-lock a solid-state ring laser gyro. This chapter is divided into four sections: 1) intracavity measurements of electro-optic coefficients using a linear cavity, 2) an experimental study on null-bias dithering, 3) a derivation that supports the experimental results of null-bias dithering and 4) solid-state saturable absorber mode-locked laser. A novel double-pulsed laser using a linear cavity makes its debut in this chapter. The linear cavity has advantages over the ring laser gyro when it is used to measure electro-optic effects because the linear cavity can only measure changes in index that occur on every round-trip.

A big advantage of a pulsed laser gyro is the ease in which the cavity can be dithered using electro-optic modulators. The frequency response to external modulation is explored for the first time, to our knowledge, in the second half of the chapter. This experiment would be almost impossible using a body-dithered continuous-wave HeNe laser. Also a new method of extracting the average beat note is demonstrated. This method doesn't require sophisticated counting electronics to keep track of the dithered phase. Finally some results using a solid-state saturable absorber are presented.

## 2.1 Linear cavity

Laser gyroscopes have been measuring rotational velocities since the advent of continuous wave ring lasers[75]. More recently, femtosecond mode-locked lasers have demonstrated a gyroscopic response for homogeneously broadened lasers, with no measurable deadband[12, 13, 76]. It is not as well known that femtosecond laser gyroscopes can also make sensitive phase measurements on a stationary optical bench[76]. The phase difference per round-trip between the clockwise (CW) and counter-clockwise (CCW) pulses is measured by combining the CW and CCW pulses on a detector. The detector will measure a beat frequency, which includes the gyroscopic response.

The phase difference can be the result of a rotation, a change in index, a mechanical vibration, or even a perturbation in a multilayer dielectric coating (for more examples of experiments see Chapter 4). Some applications of this method are measurements of the electro-optic effect[76, 77] and nonlinear spectroscopy[8]. We report the ability to make sensitive phase measurements in a linear cavity geometry, the limit of an extremely elongated ring cavity. It is possible to have two pulses circulating simultaneously in a linear cavity, which serve the same purpose as the CW and CCW pulses in a ring cavity. Without any rotation or modulation a mode-locked ring laser normally has a beat frequency bias of at least 100 Hz and as high as 100 kHz[12]. The bias frequency is a result of nonlinear effects combined with asymmetry between CW and CCW pulses. Because of the nonlinear intracavity elements, the order in which the pulse encounters the optical elements will affect the pulsewidth and pulse amplitude[57, 63, 74]. Any variation in pulse amplitude or pulsewidth will be translated into a phase-shift per round-trip in the various nonlinear intracavity elements, hence a beat signal. Since the pulses in a linear cavity travel through the same optical elements in the same order, the phase shift is the same for both pulses, and therefore no 'bias' beat note. Any of the typical T-violating asymmetries (such as the Faraday effect, rotation, and Fresnel drag) that are measured in a ring gyro cannot be measured in a linear cavity. Therefore one advantage of a linear cavity versus a ring geometry is the improvement in the frequency bias.

There is; however, competition between the two pulses for the same gain, which can

result in a difference in amplitude between the two pulse trains, hence a different phase shift due to the Kerr effect resulting in a non-zero bias. This effect was not observed and was indistinguishable from the bandwidth of the beat note. This is not surprising because the four-wave mixing in the absorber dye jet[36] should help to equilibrate any differences in amplitude. A mirror vibration of 1  $\mu\text{m}$  amplitude at a mechanical resonance frequency of 100 Hz will result in random beat frequencies in the range of 0 — 275 Hz. We routinely observed a beat frequency bias of about 100 Hz which could be a result of these random fluctuations. The beat frequency lower limit of 100 Hz is more than likely a result of mechanical vibration of the optical components, especially since we are not actively stabilizing the laser cavity[78]. In general if the cavity length  $L$  ( $L = 210$  cm in our case) is perturbed by the amount,  $\Delta L$ , in intervals corresponding to the cavity round trip time, then the measured beat frequency,  $\Delta\nu$ , will be given by:

$$\frac{\Delta\nu}{\nu} = \frac{\Delta L}{L} \quad (2.1)$$

where  $\nu$  is the optical frequency of the laser. In our case, we can measure a  $\Delta\nu$  of 100 Hz, which means a  $\Delta L$  of only  $1.1 \times 10^{-13}$  meters or about 0.1 picometers! In the following experimental results, we changed the index of refraction,  $n$ , of a 0.5 mm sample of  $\text{LiNbO}_3$ . In this case  $\Delta L \Rightarrow \Delta n \times 0.5\text{mm}$ , which implies a minimum detectable change of index of  $10^{-9}$ .

### 2.1.1 Experimental setup

The laser cavity is similar to the typical linear cavity mode-locked Ti:sapphire laser with a saturable absorber (a jet of HITCI or IR140 dye dissolved in ethylene glycol) placed in the center of the cavity, see Figure 2.1. The laser is not Kerr-lens mode-locked and the pulses are between 1.5 ps to 3.1 ps in width. There are two pulses in the cavity, because the dye jet is located in the center of the cavity. Mutual saturation of the absorber favors the pulses colliding in the dye jet. Double pulse operation can not be obtained when the laser is Kerr-lens mode-locked because of gain depletion coupled with the nonlinear loss associated with Kerr-lens mode-locking. The competition of one versus two intracavity pulses is analyzed in Chapter 3. The dye jet can be accurately centered in the cavity through translation of one

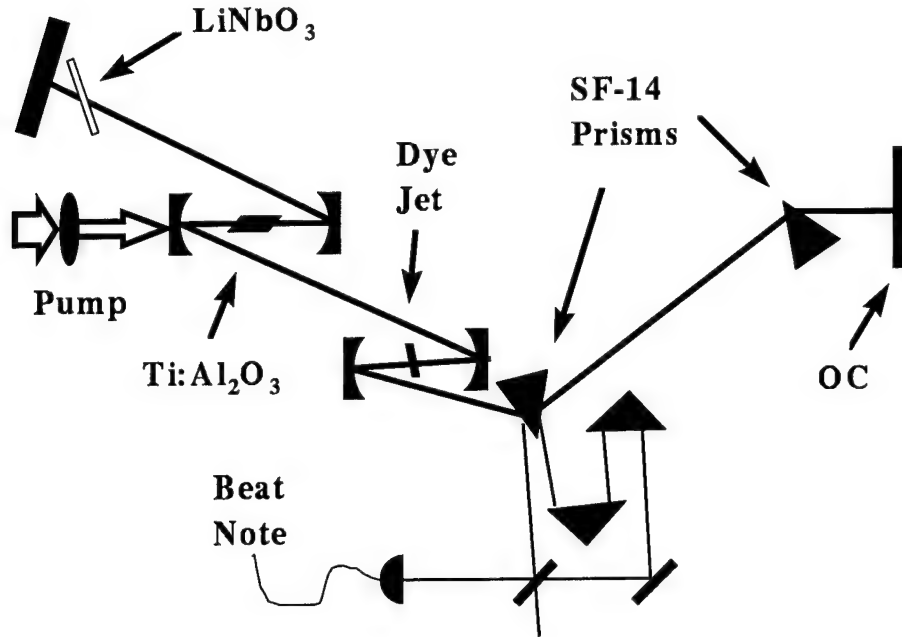


Figure 2.1: Experimental setup: The dye jet is in the center of the cavity. The curved mirrors have a 5 cm focus. The output coupler (OC) is 1.3% transmitting, and the other flat mirror is a maximum reflector ( $R=99.9\%$ ). The Ti:sapphire is 8 mm long. The SF-14 prisms are separated by 37 cm.

of the end mirrors. The distance that the end mirror can be translated while maintaining double pulses is about 2 cm. The 2 cm distance corresponds to a 120 ps delay which is close to the excited state lifetime of the dye. The dye concentration is not a critical parameter and can be varied over a broad range without affecting the performance of the laser. The output from one end of the laser goes through a variable delay and then is detected on a p-i-n photodiode. This signal is amplified by a bandwidth limited amplifier resulting in a 140 MHz sinusoidal output. The signal frequency is divided by two by converting the sinusoidal wave into ECL logic and then sending it through a flip-flop to cut the frequency in half. After the logic circuit the signal is amplified by a bandwidth limited circuit, which yields a 70 MHz sinusoidal signal. Finally the signal is amplified again and applied to the LiNbO<sub>3</sub> sample in parallel with a 50 ohm terminator. The flat mirrors consist of a 99.9% reflectivity back mirror and a 98.7% reflectivity output coupler. The mirrors in the cavity are not specially made

for short pulses and their dispersion and reflectivities were not measured. The pump laser is a Coherent Innova 200 Ar<sup>+</sup> running at about 10 W all lines. The SF-14 prism pair are used for pulse compression, by giving the cavity a net negative GVD[53]. The small reflections off of one of the prisms are combined, after a variable delay, onto a slow photodiode (RC time constant integrates over many pulses) to observe the beat frequency. A typical example of the beat note as observed on a digital oscilloscope, without averaging, is displayed in Figure 3.14.

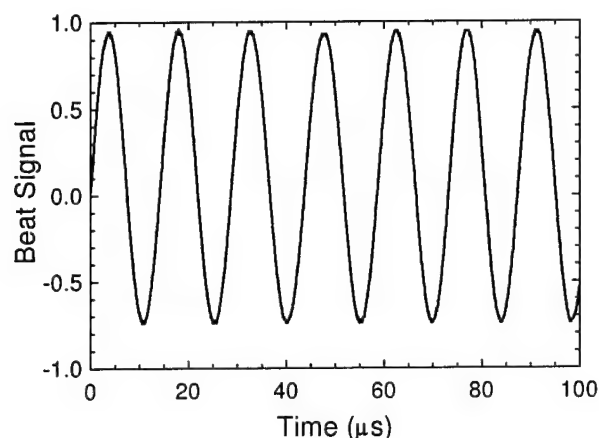


Figure 2.2: Beat note as detected on a digital oscilloscope without averaging or smoothing.

### 2.1.2 Electro-optic measurements

The first experiment consists in recording the beat note versus the delay of the signal applied to the LiNbO<sub>3</sub>. The optimum timing occurs when each of the interwoven pulse trains sees equal and opposite voltage ( $\pm V_0$ ) at the sample. Figure 2.3 is a scatter plot of the beat frequency versus delay. The line plotted in Figure 2.3 is the function  $V_0 \left| \sin\left(\frac{2\pi c}{2L}\tau - \phi_0\right) \right|$ , where the fixed phase,  $\phi_0$ , has been fit to the data. Notice the excellent correlation between theory and experiment. With the delay set for the maximum signal, the voltage is varied in order to determine the electro-optic coefficients for LiNbO<sub>3</sub>. Since the voltage is applied

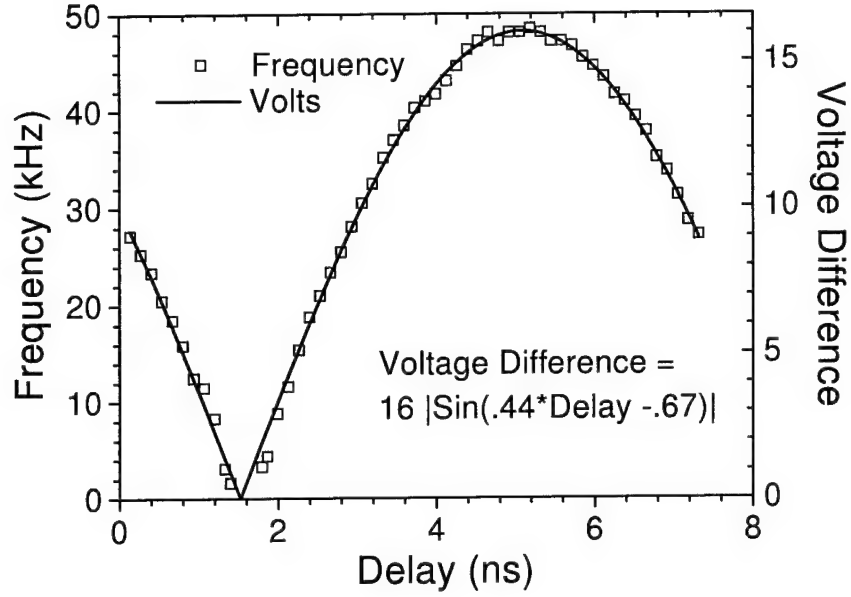


Figure 2.3: Beat frequency versus optical delay (squares) and the plot of the voltage difference applied to the sample (curve).

along the  $z$ -axis of the crystal, only two different coefficients ( $r_{13}$  and  $r_{33}$ ) can be observed.

$$\Delta \left( \frac{1}{n^2} \right)_i = \begin{pmatrix} 0 & -r_{22} & r_{13} \\ 0 & r_{22} & r_{13} \\ 0 & 0 & r_{33} \\ 0 & r_{24} & 0 \\ r_{24} & 0 & 0 \\ -r_{22} & 0 & 0 \end{pmatrix} \cdot \begin{pmatrix} 0 \\ 0 \\ \frac{V}{d} \end{pmatrix} \quad (2.2)$$

$i = 1, 2, 3 \Rightarrow x, y, z$

Where ' $i$ ' refers to the plane of polarization of the optical field. Note that for light polarized in the  $x$ - $y$  plane, the electro-optic coefficient is simply the  $r_{13}$  component and for light polarized in the  $z$  plane, the  $r_{33}$  component. The electrodes are simply two thin strips of vapor deposited gold, see Figure 2.4. Since the electric field in the  $\text{LiNbO}_3$  is a fringing field, it is difficult to extract exact results for the coefficients. However, we are able to accurately determine the ratio of the coefficients because the unknown quantities cancel in

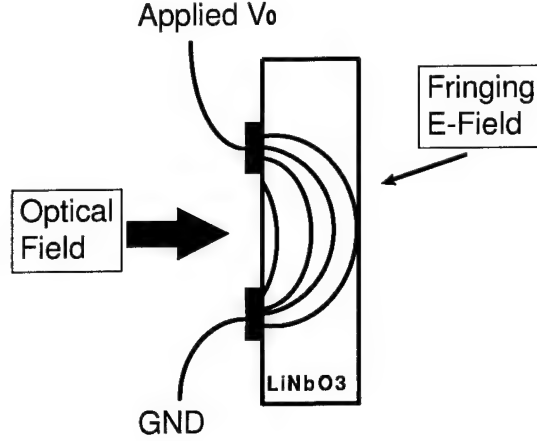


Figure 2.4: LiNbO<sub>3</sub> modulator processed in-house. The optical axis is coming up out of the page.

the equations:

$$\frac{\Delta n_z}{\Delta n_{x-y}} = \frac{n_e^3 r_{33}}{n_o^3 r_{13}} = \frac{\Delta \nu_z}{\Delta \nu_{x-y}} = 3.2 \quad (2.3)$$

Where  $n_e$  and  $n_o$  are the extraordinary and ordinary refractive indexes and  $\Delta \nu_i$  is the slope of the beat frequency versus applied voltage for light polarized in the  $i$ th direction. The beat frequency versus applied voltage for the two polarizations is plotted in Figure 2.5 along with a linear fit. Notice that the curves fit a straight line which means there is no measurable lock-in or dead band. The slopes from the linear fits are used to arrive at the ratio  $\frac{r_{33}}{r_{13}}$  of  $3.57 \pm 0.1$ , which is close to the expected[79] value of 3.62 (the value of 3.62 is an interpolation between values measured at  $\lambda = .63 \mu m$  and  $1.06 \mu m$ ). The calculation is not quite as simple as described in equation 2.3 because the LiNbO<sub>3</sub> is at Brewster's angle in the cavity, but the actual calculation differs by only a simple geometric relation when it is oriented in the z-axis.

$$\Delta n_{z-measured} = \sqrt{(\cos(\theta_b) \Delta n_z)^2 + (\sin(\theta_b) \Delta n_x)^2}$$

When the LiNbO<sub>3</sub> is at Brewster's angle in the x-y plane, there isn't a problem because  $\Delta n_x = \Delta n_y$ . The error bars are a result of power fluctuations in the RF amplifier and the

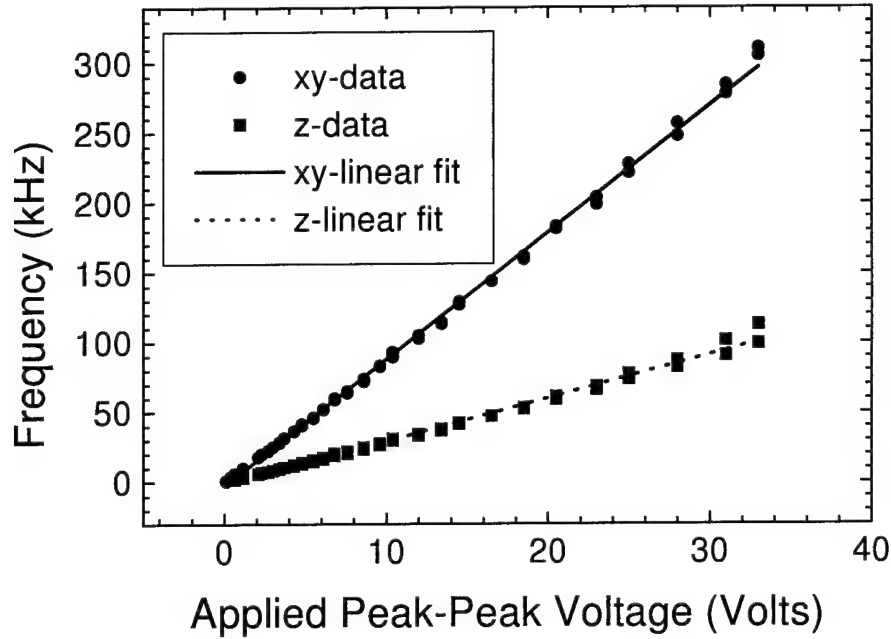


Figure 2.5: Beat frequency versus applied voltage for two different polarizations.

error in measuring the RF amplitude. It is not indicative of the ultimate resolution of the measurement technique.

## 2.2 Ring gyro

The picosecond ring gyro is very similar to the linear cavity without the prisms. Without the prisms, the net GVD of the cavity is at least  $600 \text{ fs}^2$ . Because a stable soliton solution does not exist for positive GVD in the nonlinear Schrodinger equation, the concept of soliton-like pulse-shaping does not apply for this laser. Pulse durations are in the 20 ps range as can be seen by the autocorrelation in Figure 2.6. It is extremely difficult to obtain an autocorrelation of this length because the delay must be scanned over a range of 1.5 cm. We use a type-II, background-free autocorrelator (there is a schematic in Chapter 3). Because this autocorrelator uses a polarizing beam splitter/combiner, the retro-reflectors in the Michelson interferometer are simply silver mirrors. It is very simple to translate mirrors and maintain



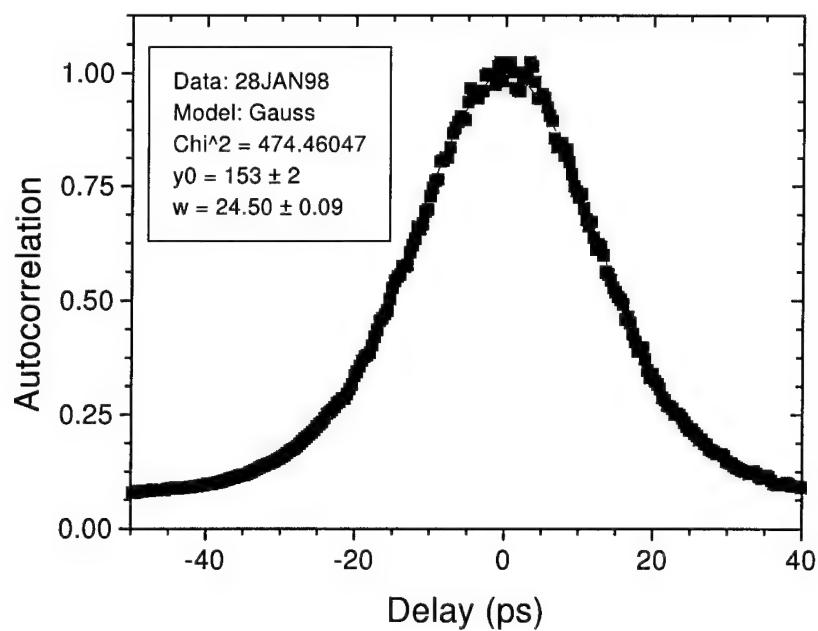


Figure 2.6: Background-free second-order intensity autocorrelation of a Ti:sapphire ring laser mode-locked with an absorbing dye jet without prisms for GVD compensation.  $\tau_{pulse} = 17.3$  ps.

alignment whereas a retro-reflecting corner cube typically misaligns after translating (unless great care is taken in its alignment).

The peak powers in this geometry are reduced by a factor of ten, which should minimize the nonlinear, nonreciprocal processes that generate the bias beat note. In fact, the lowest beat note was measured using a ring cavity without prisms. It is difficult to measure a low beat note because of various nonreciprocal effects in the laser like the motion of the dye jet, air currents (Fresnel drag) and mechanical noise. The experimental schematic is shown in Figure 2.7. Notice that there is an additional fused silica plate inserted near the

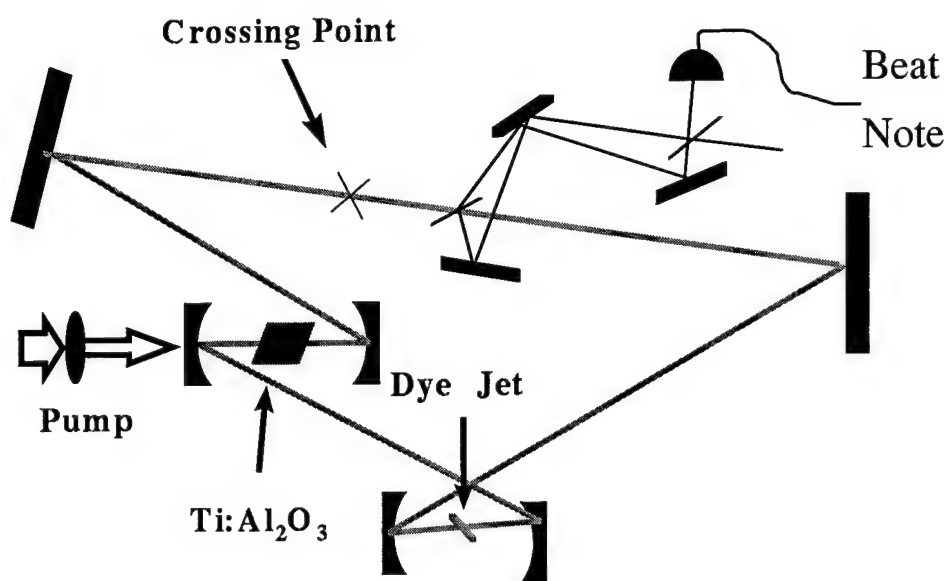


Figure 2.7: Experimental arrangement for ring gyro. Fused silica plate is used to minimize the size of the beat note interferometer.

crossing point. The plate is used to pick off beams for the beat note detection. It is very important that the beat note interferometer be kept as small as possible to minimize noise from vibrating mirrors and air currents. The beat signal with the narrowest bandwidth and its Fourier transform is shown in Figure 2.8. The bandwidth is limited by the time interval. The log plot of Figure 2.8 is shown in Figure 2.9. Notice the  $\frac{1}{f}$  noise and the spike

corresponding to the beat signal, obviously there is no background subtraction in this data. Recall from Chapter 1 that the lock-in frequency is given by:  $\ell = \frac{2pr}{(1-r^2)}$ , where  $r$  is the ratio of the amplitude of the second-harmonic to the fundamental. Based on the amplitude of the second and third-harmonic, we estimate the upper bound of the lock-in frequency to be 35 Hz for the data in Figure 2.9. Figure 2.10 is a longer trace (10 seconds) and the beat note is centered at 10 Hz, an amazingly low beat note. For this data, the harmonic analysis yields an upper bound of the lock-in frequency of 4.64 Hz. Figure 2.10 demonstrates the dynamic nature of the beat note. It appears that the beat note has good spectral quality for short time periods, but the frequency varies perhaps due to motion of the table, the dye jet or air currents. The beat note is typically lower after 7 PM when the local traffic has decreased, so perhaps the major factor contributing to the beat note is motion of the table.

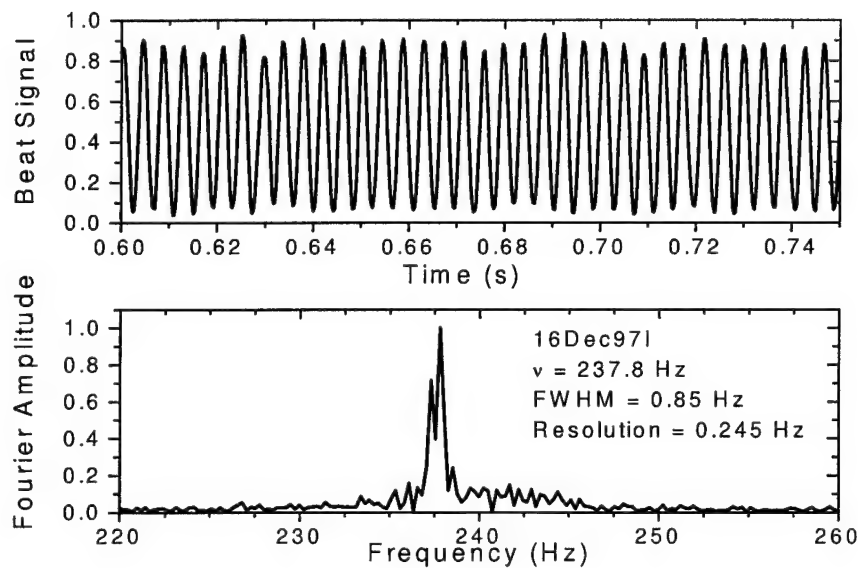


Figure 2.8: Smallest bandwidth ever recorded using a Ti:sapphire ring laser gyro. The time series shows only a small portion of the data. The data was taken for 0.74 seconds.

The advantage of the linear cavity is that it cannot measure a beat note from air currents and table rotations. For the ring laser, these effects become interesting demonstrations. By simply blowing air along one of the arms of the ring gyro, a beat note is detected.

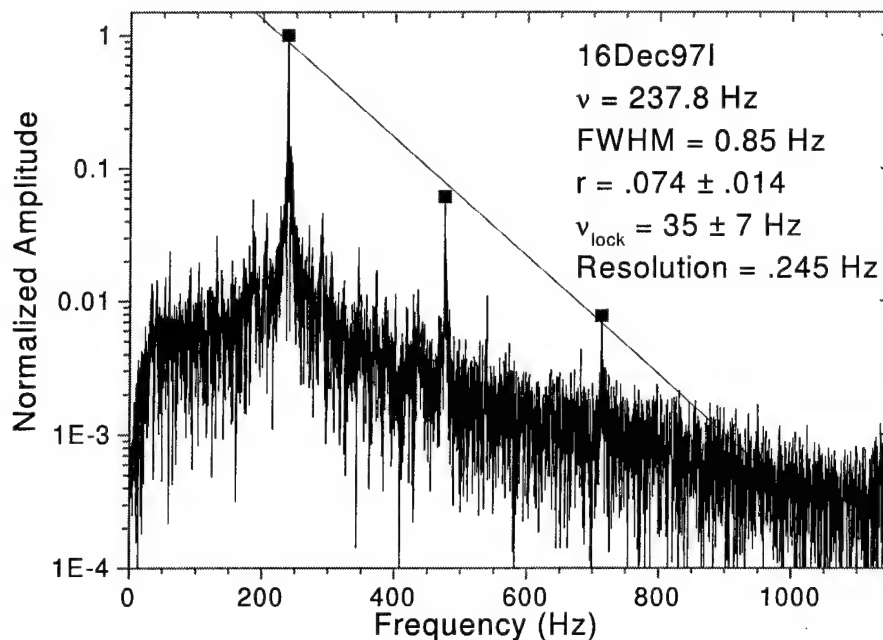


Figure 2.9: Log plot of Figure 2.8. Notice the  $1/f$  noise and the beat note spike that is 50 db above the noise.

This is a result of the vector addition of light in a moving medium. It is not a simple Doppler shift, but rather a result of special relativity. The Fresnel drag provides a simple way to remove the ambiguity on the sign of the beat note. The laser has a bias beat note of 100 Hz. When the air is blown in the CW direction, the beat note increased to 200 Hz. When the air is blown in the CCW direction, the beat note decreased to near zero. Clearly the frequency of the CCW pulse was lower than the frequency of the CW pulse. This bias is small enough to be the rotation rate of the earth, but there are many other contributions on the same order of magnitude.

Another interesting experiment is to simply tap the cavity mirrors, not enough to disturb the lasing, but enough to hear the vibrations of the mirror. The beat note can be heard by simply amplifying it and sending it to a speaker. It is clear that the vibrations of some mirrors lasts significantly longer than others. The worst mirror was sitting on a 'home-made' aluminum mount. Perhaps it is worth the cost to purchase quality mounts for

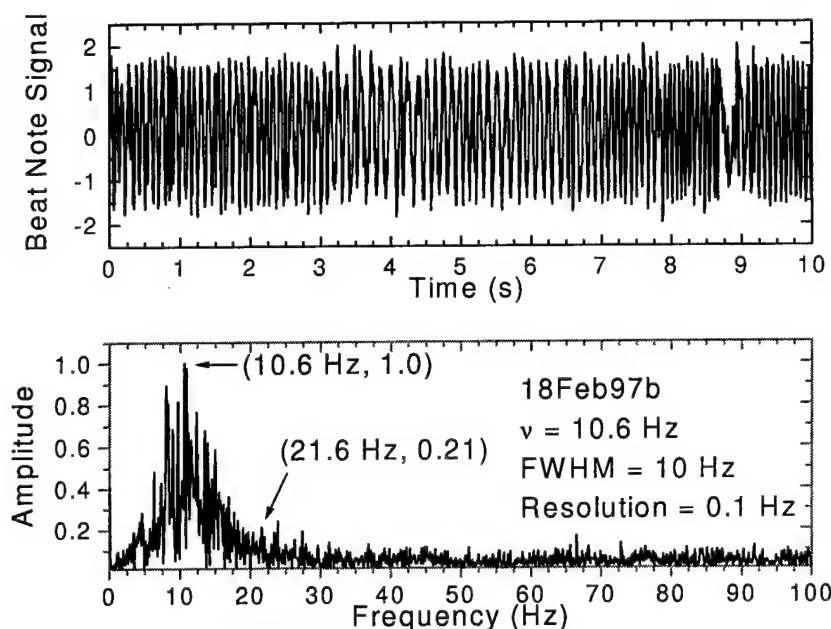


Figure 2.10: Lowest beat note recorded using a Tisapphire laser. The data was taken for 10 seconds, which implies a resolution of 0.1 Hz. Comparison with Figure 2.8 indicates that the broader bandwidth here is to be attributed to random frequency drifts on a time scale of seconds.

a laser cavity.

By inserting a nonlinear crystal, CdS, into the laser at a waist, we are able to detect the complex nonlinear refractive index of the crystal. Because CdS is also a two-photon absorber, the extraction of the nonlinearity is nontrivial. Current experiments are attempting to measure the nonlinear index,  $n_2$ , of fused silica. By translating the sample along the propagation direction, the amount of nonlinear refraction varies as a function of beam waist. The nonlinear refractive index is nonreciprocal because there is a 5% output coupler on one side of the crystal, so the powers are nonreciprocal by 5%. The derivation of the beat frequency resulting from a nonlinearity is derived in Chapter 3. A plot of the beat frequency versus location in the cavity is shown in Figure 2.11.

Table vibrations could also be measured in a similar method. A small tap to the table generates a high pitched, chirping squeal from the speaker. The minimum beat note

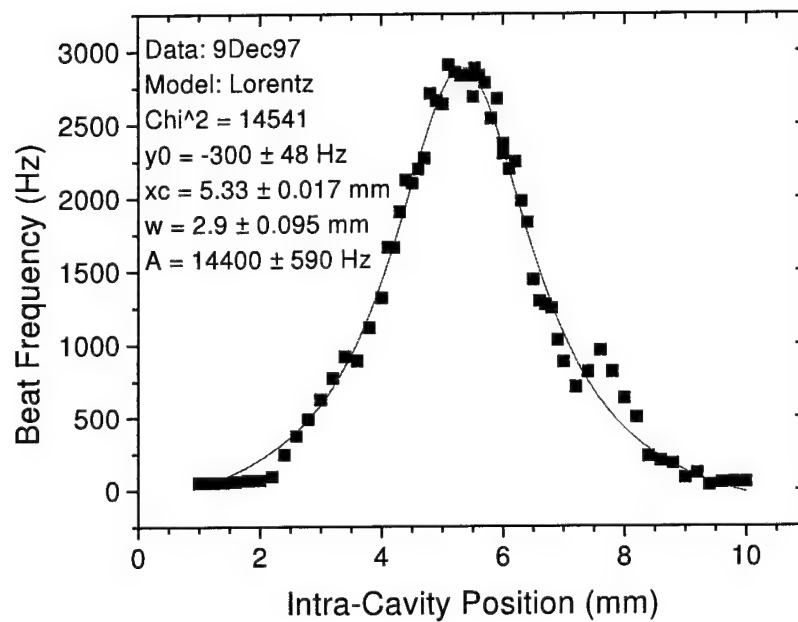


Figure 2.11: Plot of the beat frequency versus the location of CdS inside the cavity.

also depends on the time of day. Data taken after 7:00 PM has a significantly lower beat note. The diurnal variations are likely due to local traffic patterns.

### **2.2.1 Large ring**

It is important to demonstrate scalability of a laser gyro, if it is to be used to measure sensitive rotations like the earth's rotation rate. As the perimeter of laser gyros increases it will become increasingly more difficult for HeNe laser gyros to prevent multi-mode operation because the separation of the longitudinal modes becomes extremely small. The pump power must be carefully controlled in a HeNe laser gyro, such that only one mode reaches threshold[3]. In a mode-locked laser, it should be trivial to scale to longer perimeters as long as the round-trip time is much shorter than the excited-state lifetime. To demonstrate the scalability of the Ti:sapphire laser gyro, we constructed a laser with a perimeter of 10 m. This is 2.5 times the size of the most sensitive laser gyro constructed to this date[3]. For this to be a fair test of this laser, the air-floatation of the table was turned off. The beat signal is shown in Figure 2.12. The noise at 110 Hz is believed to be a result of the water pumps above the lab. Even with a perimeter of 10 meters, the laser is capable of producing a beat frequency of 40 Hz. The earth's rotation would cause a beat frequency of 120 Hz, if this laser had a square perimeter.

## **2.3 Electro-optic dither (theory and experiment)**

### **2.3.1 Introduction**

Since 1967[25] it was recognized that one method to avoid the lock-in of counter-propagating beams was to add an artificial rotation rate. This artificial rotation avoids the dead-band region of a laser gyro and restores linear operation. In a continuous-wave HeNe laser this is accomplished by mounting the laser on springs and driving the spring-mass system with a piezo-electric transducer. Because the frequency of modulation is determined by the spring-mass system, it is not easy to explore the parameter space using a HeNe laser gyro. A big advantage in a pulsed laser gyro is that the modulation rate and amplitude can be changed

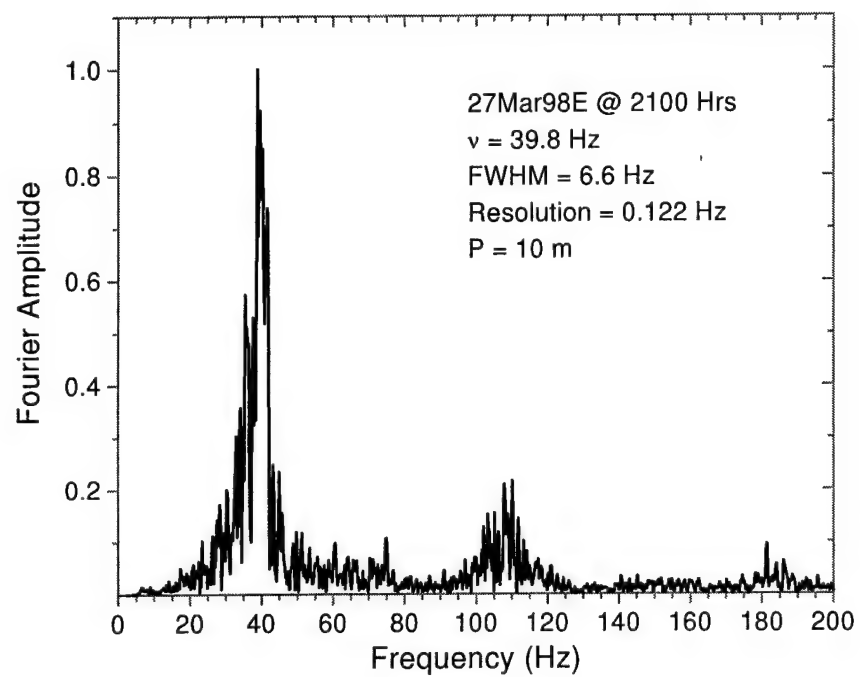


Figure 2.12: FFT of beat signal from 10 meter perimeter ring laser gyro.



very easily and quickly by the use of an electro-optic modulator. The E-O modulator creates the same optical effect as if the gyro was first rotated in the CW direction and then rotated in the CCW direction. In this section, there are three frequencies that will be explored. The modulation frequency determines how often the artificial frequency is switched from CW to CCW. The other two frequencies are associated with the effective CW and CCW rotations. We will determine the optimum modulation frequency dependent on the maximum rotation rate. The experimental results are supported with analytic calculations.

### 2.3.2 Null-bias dithering: experimental

The experimental setup is shown in Figure 2.13. Notice the output of the function generator modulates the RF applied to the  $\text{LiNbO}_3$  which changes the cavity length. The quartz

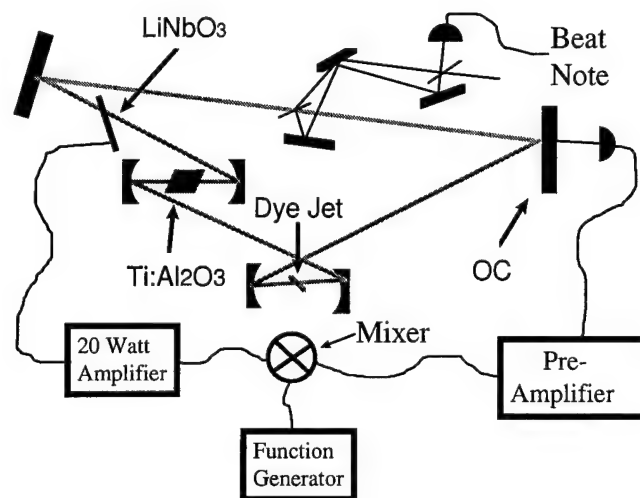


Figure 2.13: Experimental setup for null-bias dithering. A small quartz plate is inserted near the crossing point at Brewster's angle to output couple two beams for the beat note detection.

plate splits off two beams for beat note detection. It is located near the pulse crossing point to minimize the physical size of the interferometer used to detect the beat note. If the output coupled pulses are used for the beat note detection, the interferometer would have to be several meters long which would result in more noise. The output from the function generator is mixed with the RF before the final RF amplification. The RF is at

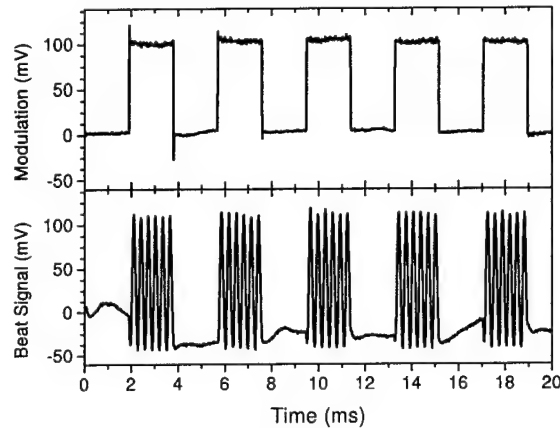


Figure 2.14: Upper plot is the square wave modulation that is applied to the RF signal via an RF mixer. The lower plot is the corresponding beat signal.

the cavity frequency and is used to create a frequency difference between the CW and CCW pulses. The modulation frequency is varied using the function generator. For square wave modulation, the laser will generate two beat frequencies of equal magnitude but opposite in sign. The oscilloscope trace shown in Figure 2.14 should help clarify the modulation and the corresponding beat note. When the modulation is in the low state, there is no RF applied to the E-O modulator and therefore the beat signal is close to zero. When the modulation is in the high state, the RF power is at a maximum and the beat note is at a maximum. As the modulation frequency is increased, eventually the cavity will not respond to the modulation. If the cavity is not responding to the modulation, it should "average" out the modulation. Assuming a perfect square wave modulation, this means the beat note should eventually disappear because the average would be zero. If the modulation is not a perfect square wave (i.e. the beat notes are not equal, but are opposite in sign), then the beat note will roll off to a constant frequency at the average of the two beat frequencies. For example if the beat note for a positive modulation is  $\omega_1$  and the negative modulation is  $\omega_2$  then the beat note when the cavity is no longer responding will be  $\frac{\omega_1 + \omega_2}{2}$ .

By putting the beat note into a spectrum analyzer, it is easy to monitor the amplitude of one of the beat frequencies,  $\omega_1$ , as a function of the modulation frequency. The plot of

the amplitude at  $\omega_1$  as a function of the modulation frequency is shown in Figure 2.15. Note that it is roughly exponential, but there is a faint sinusoidal modulation.

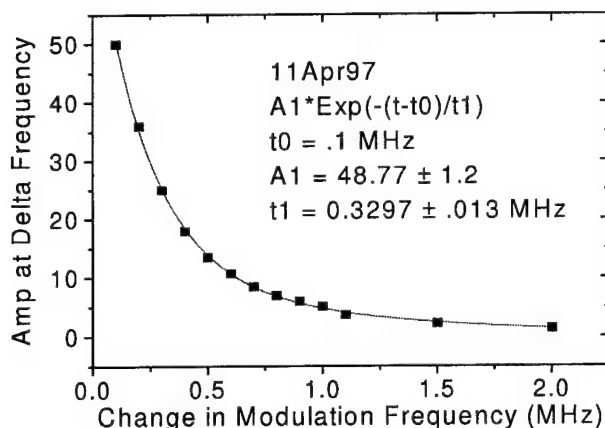


Figure 2.15: Amplitude of  $\omega_1$  beat note as a function of the modulation frequency. The data is fit to an exponential decay.

While varying the modulation frequency near the roll-off point, the beat note goes through some strange resonances. Eventually the beat note rolls-off to the average frequency. In between the roll-off and the slow modulation, the beat signal would appear to contain structure at the average frequency. Figure 2.16 is a time trace demonstrating the modulation of the beat note. The average frequency is just beginning to appear in this oscilloscope trace. Figure 2.17 shows the beat signal when the frequencies  $\omega_1$  and  $\omega_2$  have almost disappeared and all that is left is  $\omega_{ave}$ . Instead of monitoring the decay of the beat frequency  $\omega_1$ , we monitored the average frequency ( $\omega_{ave} = \frac{\omega_1 + \omega_2}{2}$ ). This produced the smoothly varying curve shown in Figure 2.18. Figure 2.18 illustrates the fit to an inverse sinc(x) function. This function is the sinc(x), but the argument is inverted (i.e.  $f_{mod}P1 \sin(\frac{P2}{f_{mod}})$ ; where  $P1$  and  $P2$  are constants). If the amplitude was plotted versus the modulation period,  $T$ , the graph would have been immediately recognized as the sinc(x) function.

By varying the beat frequencies,  $\omega_1$  and  $\omega_2$ , the functional dependence of the width of the inverse sinc(x) constant  $P2$  are determined. Not only was the amplitude of the beat notes varied, but also the sum and difference. Only when the width is plotted versus the

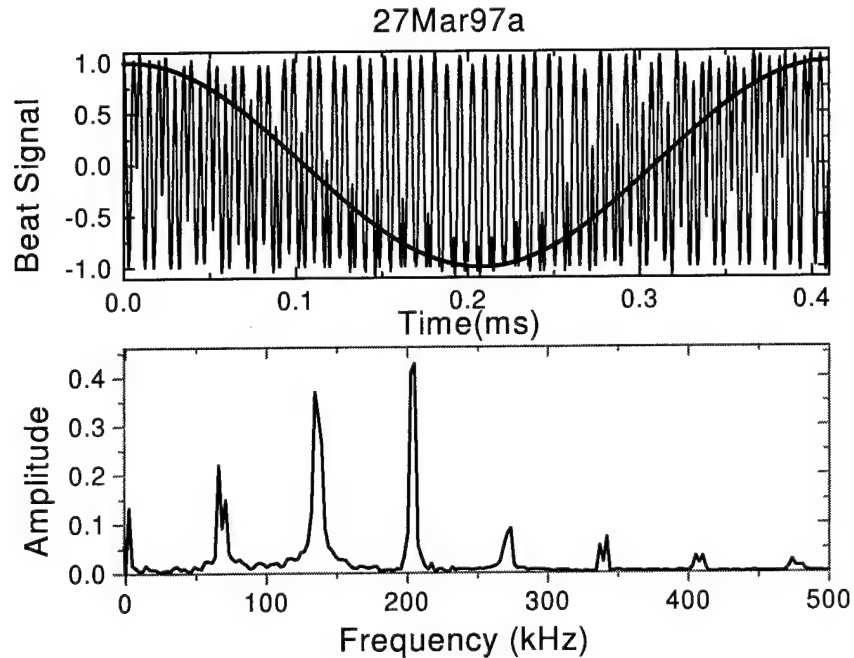


Figure 2.16: Upper: Beat signal as seen on the oscilloscope. The low frequency modulation is highlighted by the curve. Below: FFT of the beat signal.

difference in beat frequencies, did a linear dependence appear (see Figure 2.19). All other plots showed no correlation.

### 2.3.3 Derivation of modulation spectrum

Great care has to be taken when analyzing the phase difference of the modulated laser. When the modulation changes state, the slope of the phase is discontinuous while the phase must be continuous. By writing down the analytic description of the phase and taking the Fourier transform, we obtained an equation which fit the experimental data extremely well. It turns out that the continuity of phase was the crucial parameter.

There is a very simple explanation of the averaging phenomena at work in this system. If you take 100 steps forward and then take 99 steps backward; you have moved forward one step. If you take the steps fast enough, it will appear as if you are simply moving forward

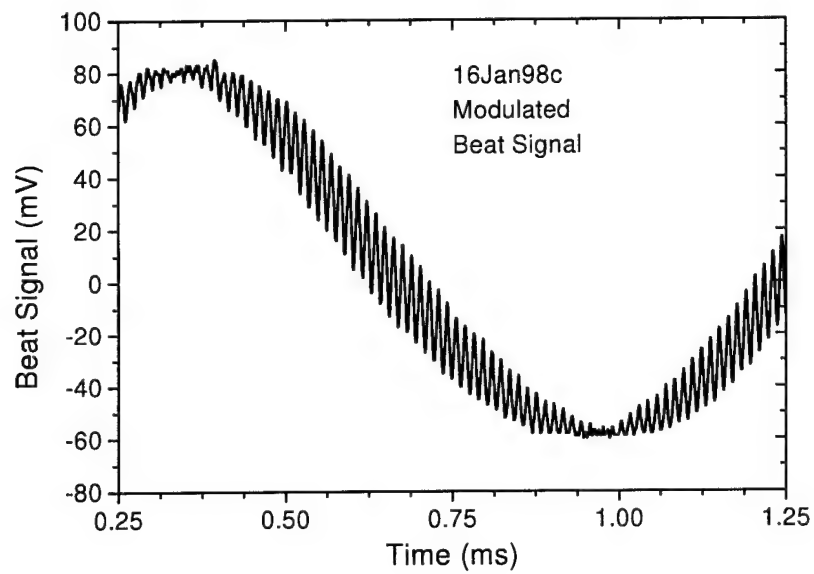


Figure 2.17: Beat signal demonstrating the roll-off to  $\omega_{ave}$ . Notice in this plot that the beat signals at  $\omega_1$  and  $\omega_2$  are barely visible.

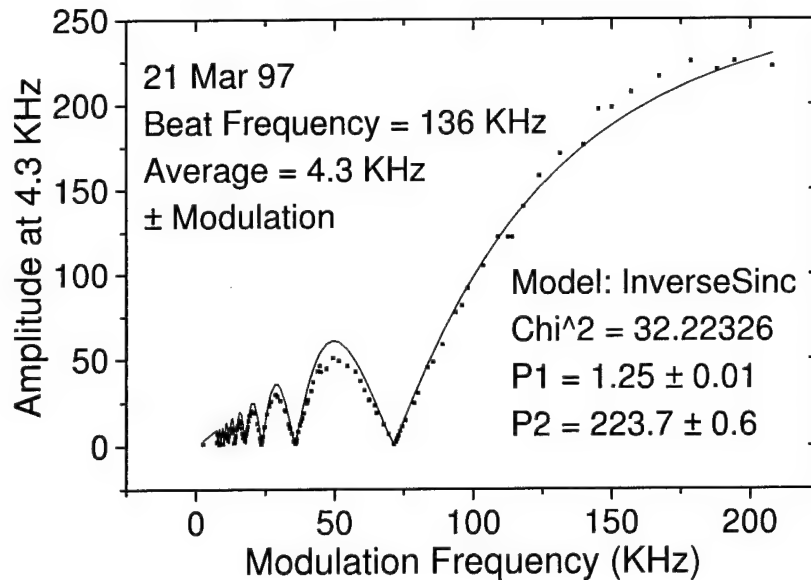


Figure 2.18: Amplitude of average frequency as a function of modulation frequency. The model is  $f_{\text{mod}} * P1 * \sin(P2/f_{\text{mod}})$ .

one step at a time. Notice that it is the one step difference at the end of the iteration that makes all the difference in your forward progress. You might also be wondering why is it a  $\text{sinc}(x)$  function? Why does the forward progress periodically go to zero? This is also very easy to explain. If the 'step' that is left over is equal to  $\pi$ , then you are actually back where you started. You can think of it like this: if you are taking your steps on a circle, then the value of  $\pi$  puts you on the other side of the circle and if your ruler is measuring only the absolute distance in the x-direction, then you are back where you started. Remember that in the experimental setup, the measured beat note has an ambiguity of sign.

The analytic solution is derived below in the following steps: 1) write out the phase as a function of time. 2) Setup the Fourier transform and evaluate it at  $\omega_{\text{ave}} = \frac{\omega_1 + \omega_2}{2}$ . 3) Ratio the Fourier transform by the maximum possible signal. 4) Take limit as time goes to infinity.

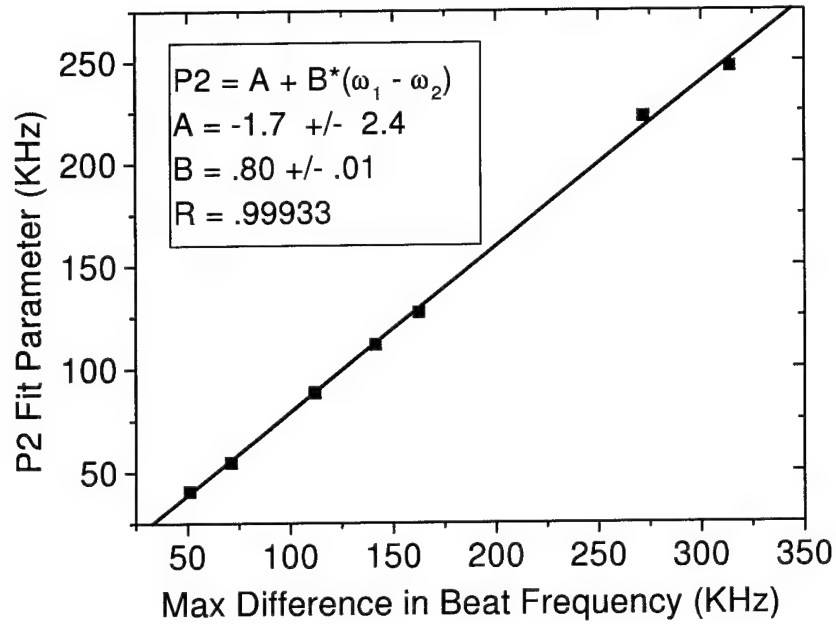


Figure 2.19: Plot of P2 fit parameter versus the beat frequency difference. The slope of the straight line is predicted by theory to be  $\frac{\pi}{4}$ .

### Step 1: Finding the phase as a function of time.

This is not as easy as it sounds. The assumptions are that the phase is continuous, but discontinuous in slope at intervals of  $T$ . Figure 2.20 below should help visualize the time dependence of the phase.

Starting from  $t = 0$ , the phase is:

$$\phi_1 = \omega_1 t \text{ for } 0 \leq t \leq T$$

$$\phi_2 = \omega_2 t + T(\omega_1 - \omega_2) \text{ for } T \leq t \leq 2T$$

$$\phi_1 = \omega_1 t + T(\omega_2 - \omega_1) \text{ for } 2T \leq t \leq 3T$$

$$\phi_2 = \omega_2 t + 2T(\omega_1 - \omega_2) \text{ for } 3T \leq t \leq 4T$$

$\vdots$

$$\phi_1(n, t) = \omega_1 t + (n-1)T(\omega_2 - \omega_1) \text{ for } 2(n-1)T \leq t \leq (2n-1)T$$

$$\phi_2(n, t) = \omega_2 t + nT(\omega_1 - \omega_2) \text{ for } (2n-1)T \leq t \leq 2nT$$

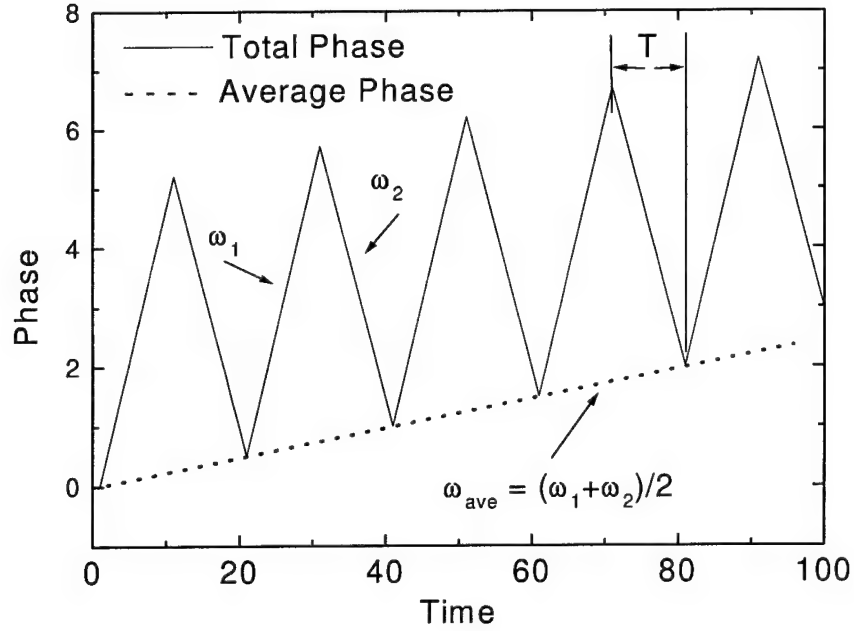


Figure 2.20: Plot of the phase as a function of time. The phase is continuous, but discontinuous in slope. The dotted line is the average phase. The modulation period is  $2T$ .

$$\phi(t) = \sum_{n=1}^{\infty} \left[ \begin{array}{l} \phi_1(n, t) \delta(2(n-1)T \leq t \leq (2n-1)T) + \\ \phi_2(n, t) \delta((2n-1)T \leq t \leq 2nT) \end{array} \right] \quad (2.4)$$

The last expression may look complicated, but it is setup for piecewise integration. The Kronecker-Delta function will form the limits of the piecewise integration. Notice that the phase term is always changing in order to maintain continuity of total phase, even when the slope changes from  $\omega_1$  to  $\omega_2$ . Figure 2.20 was plotted using the equation above to ensure that the total phase is continuous. Next the  $\sin(\phi(t))$  was plotted to see if the beat note would look similar to the experimental data. Figure 2.21 and Figure 2.22 are two generated beat signals. Figure 2.22 is modulated ten times faster than Figure 2.21. Notice the transition to  $\omega_{ave}$  as the modulation frequency is increased. Compare these plots with



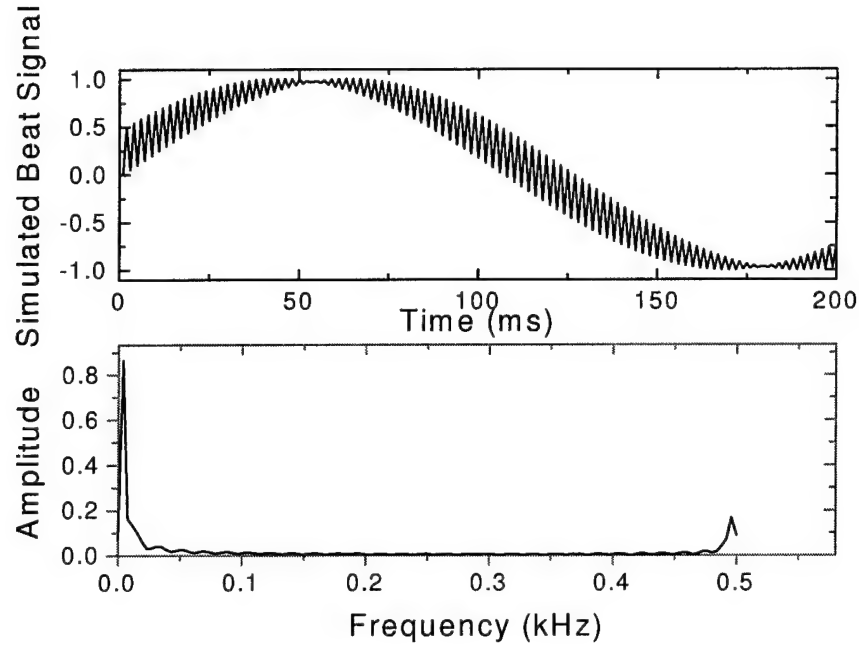


Figure 2.22: Generated beat signal. The modulation frequency is 10,  $\omega_1$  is 5.2 and  $\omega_2$  is -4.7. Here we see the rolloff toward  $\omega$  is almost complete, there is only a small modulation at the original beat frequencies. The time scale is different from the graph above.

we take the limit as  $m \rightarrow \infty$ .

### Denominator

$$denom = \int_0^{\infty} \sin^2 \left( \frac{(\omega_1 + \omega_2)t}{2} \right) dt \quad (2.5)$$

$$denom = \sum_{n=1}^{\infty} \left[ \int_{2(n-1)T}^{2nT} \sin^2 \left( \frac{(\omega_1 + \omega_2)t}{2} \right) dt \right] \quad (2.6)$$

$$denom = \sum_{n=1}^{\infty} \left\{ \int_{2(n-1)T}^{2nT} \frac{1}{2} [\cos(0) - \cos((\omega_1 + \omega_2)t)] dt \right\} \quad (2.7)$$

$$denom = \sum_{n=1}^{\infty} \frac{1}{2} \left[ T - \frac{\sin((\omega_1 + \omega_2)t)}{(\omega_1 + \omega_2)} \right]_{2(n-1)T}^{2nT} \quad (2.8)$$

$$denom = \lim_{m \rightarrow \infty} \left\{ \sum_{n=1}^m \left[ T + \frac{\sin(2(n-1)(\omega_1 + \omega_2)T) - \sin(2n(\omega_1 + \omega_2)T)}{2(\omega_1 + \omega_2)} \right] \right\} \quad (2.9)$$

The finite sum to the arbitrary number  $m$  was accomplished on Mathematica.

$$denom = \lim_{m \rightarrow \infty} \left\{ mT - \frac{\sin(2m(\omega_1 + \omega_2)T)}{2(\omega_1 + \omega_2)} \right\} \quad (2.10)$$

#### $\omega_1$ sine-integral

$$\omega_1 part = \int_0^{\infty} \sin\left(\frac{(\omega_1 + \omega_2)t}{2}\right) \sin(\phi_1(t)) dt \quad (2.11)$$

$$\omega_1 part = \sum_{n=1}^{\infty} \left[ \int_{2(n-1)T}^{(2n-1)T} \sin\left(\frac{(\omega_1 + \omega_2)t}{2}\right) \sin(\omega_1 t + (n-1)T(\omega_2 - \omega_1)) dt \right] \quad (2.12)$$

$$\omega_1 part = \frac{1}{2} \sum_{n=1}^{\infty} \left[ \int_{2(n-1)T}^{(2n-1)T} \cos\left((n-1)(\omega_2 - \omega_1)T + \frac{(\omega_1 - \omega_2)t}{2}\right) - \cos\left((n-1)(\omega_2 - \omega_1)T + \frac{(3\omega_1 + \omega_2)t}{2}\right) dt \right] \quad (2.13)$$

$$\omega_1 part = \sum_{n=1}^{\infty} \left[ \frac{\sin((n-1)(\omega_2 - \omega_1)T + \frac{(\omega_1 - \omega_2)t}{2})}{(\omega_1 - \omega_2)} - \frac{\sin((n-1)(\omega_2 - \omega_1)T + \frac{(3\omega_1 + \omega_2)t}{2})}{3\omega_1 + \omega_2} \right]_{2(n-1)T}^{(2n-1)T} \quad (2.14)$$

$$\omega_1 part = \lim_{m \rightarrow \infty} \left\{ \begin{aligned} & \sum_{n=1}^m \left[ \frac{\sin\left(\frac{(\omega_1 - \omega_2)T}{2}\right)}{(\omega_1 - \omega_2)} \right] + \\ & \sum_{n=1}^m \left[ \frac{\sin(2(n-1)(\omega_1 + \omega_2)T)}{(3\omega_1 + \omega_2)} \right] + \\ & \sum_{n=1}^m \left[ \frac{\sin\left(\frac{(\omega_1 + 3\omega_2)T}{2} - 2nT(\omega_1 + \omega_2)\right)}{(3\omega_1 + \omega_2)} \right] \end{aligned} \right\} \quad (2.15)$$

The finite sum to the arbitrary number  $m$  was accomplished on Mathematica.

$$\omega_1 part = \lim_{m \rightarrow \infty} \left\{ \begin{aligned} & \frac{\sin\left(\frac{(\omega_1 - \omega_2)T}{2}\right)}{(\omega_1 - \omega_2)} m + \\ & \frac{\sin(m(\omega_1 + \omega_2)T) \sin((\omega_1 + \omega_2)T(m-1))}{(3\omega_1 + \omega_2) \sin((\omega_1 + \omega_2)T)} + \\ & \frac{\sin(mT(\omega_1 + \omega_2)) \sin\left(\frac{(\omega_1 + 3\omega_2)T - 2T(\omega_1 + \omega_2)(m+1)}{2}\right)}{(3\omega_1 + \omega_2) \sin(T(\omega_1 + \omega_2))} \end{aligned} \right\} \quad (2.16)$$

$$\frac{\omega_1 part}{denom} = \lim_{m \rightarrow \infty} \left\{ \begin{aligned} & \frac{m \sin\left(\frac{(\omega_1 - \omega_2)T}{2}\right)}{(\omega_1 - \omega_2) \left[ mT - \frac{\sin(2m(\omega_1 + \omega_2)T)}{2(\omega_1 + \omega_2)} \right]} + \\ & \frac{\sin(m(\omega_1 + \omega_2)T) \sin((\omega_1 + \omega_2)T(m-1))}{(3\omega_1 + \omega_2) \sin((\omega_1 + \omega_2)T) \left[ mT - \frac{\sin(2m(\omega_1 + \omega_2)T)}{2(\omega_1 + \omega_2)} \right]} + \\ & \frac{\sin(mT(\omega_1 + \omega_2)) \sin\left(\frac{(\omega_1 + 3\omega_2)T - 2T(\omega_1 + \omega_2)(m+1)}{2}\right)}{(3\omega_1 + \omega_2) \sin(T(\omega_1 + \omega_2)) \left[ mT - \frac{\sin(2m(\omega_1 + \omega_2)T)}{2(\omega_1 + \omega_2)} \right]} \end{aligned} \right\} \quad (2.17)$$

divide top and bottom by  $m$ :

$$\frac{\omega_1 part}{denom} = \lim_{m \rightarrow \infty} \left\{ \frac{\sin\left(\frac{(\omega_1 - \omega_2)T}{2}\right)}{(\omega_1 - \omega_2) \left[T - \frac{\sin(2m(\omega_1 + \omega_2)T)}{m2(\omega_1 + \omega_2)}\right]} + \right. \\ \left. \frac{\sin(m(\omega_1 + \omega_2)T) \sin((\omega_1 + \omega_2)T(m-1))}{m(3\omega_1 + \omega_2) \sin((\omega_1 + \omega_2)T) \left[T - \frac{\sin(2m(\omega_1 + \omega_2)T)}{m2(\omega_1 + \omega_2)}\right]} + \right. \\ \left. \frac{\sin(mT(\omega_1 + \omega_2)) \sin\left(\frac{(\omega_1 + 3\omega_2)T - 2T(\omega_1 + \omega_2)(m+1)}{2}\right)}{m(3\omega_1 + \omega_2) \sin(T(\omega_1 + \omega_2)) \left[T - \frac{\sin(2m(\omega_1 + \omega_2)T)}{m2(\omega_1 + \omega_2)}\right]} \right\} \quad (2.18)$$

All terms but the first involve  $\lim_{x \rightarrow \infty} \frac{\sin(x)}{x}$ , which goes to zero in the limit. Therefore only the first term survives:

$$\frac{\omega_1 part}{denom} = \frac{\sin\left(\frac{(\omega_1 - \omega_2)T}{2}\right)}{T(\omega_1 - \omega_2)} \quad (2.19)$$

The  $\omega_2$  sine-integral yields the same result and is not included. The cosine-integral for  $\omega_2$  is included below:

### $\omega_2$ cosine-integral

Although the  $\omega_2$  cosine-integral is similar in structure to the  $\omega_1$  sine-integral there are enough differences that it is worthwhile to go completely through the derivation. Notice in particular that the phase term in the  $\omega_1$  integral is  $(n-1)T(\omega_2 - \omega_1)$  and in the  $\omega_2$  integral it is  $nT(\omega_1 - \omega_2)$ .

$$\omega_2 part = \int_0^{\infty} \cos\left(\frac{(\omega_1 + \omega_2)t}{2}\right) \sin(\phi_2(t)) dt \quad (2.20)$$

$$\omega_2 part = \sum_{n=1}^{\infty} \left[ \int_{(2n-1)T}^{2nT} \cos\left(\frac{(\omega_1 + \omega_2)t}{2}\right) \sin(\omega_2 t + nT(\omega_1 - \omega_2)) dt \right] \quad (2.21)$$

$$\omega_2 part = \frac{1}{2} \sum_{n=1}^{\infty} \left[ \int_{(2n-1)T}^{2nT} \sin\left(\frac{(\omega_1 + 3\omega_2)t}{2} + nT(\omega_1 - \omega_2)\right) - \right. \\ \left. \sin\left(\frac{(\omega_2 - \omega_1)t}{2} - nT(\omega_1 - \omega_2) + \right) dt \right] \quad (2.22)$$

$$\omega_{2part} = \sum_{n=1}^{\infty} \left[ \frac{\cos\left(\frac{(\omega_1+3\omega_2)t}{2} + nT(\omega_1-\omega_2)\right)}{\omega_1+3\omega_2} - \frac{\cos\left(\frac{(\omega_1-\omega_2)t}{2} - nT(\omega_1-\omega_2)\right)}{(\omega_1-\omega_2)} \right] \frac{2nT}{(2n-1)T} \quad (2.23)$$

$$\omega_{2part} = \lim_{m \rightarrow \infty} \left\{ \sum_{n=1}^m \left[ \frac{1}{(\omega_1-\omega_2)} \right] - \sum_{n=1}^m \left[ \frac{\cos\left(\frac{(\omega_1-\omega_2)T}{2}\right)}{(\omega_1-\omega_2)} \right] - \sum_{n=1}^m \left[ \frac{\cos(2nT(\omega_1+\omega_2))}{(\omega_1+3\omega_2)} \right] + \sum_{n=1}^m \left[ \frac{\cos\left(2nT(\omega_1+\omega_2) - \frac{(\omega_1+3\omega_2)T}{2}\right)}{(\omega_1+3\omega_2)} \right] \right\} \quad (2.24)$$

The finite sum to the arbitrary number  $m$  was accomplished on Mathematica.

$$\omega_{2part} = \lim_{m \rightarrow \infty} \left\{ \frac{m}{(\omega_1-\omega_2)} - \frac{m \cos\left(\frac{(\omega_1-\omega_2)T}{2}\right)}{(\omega_1-\omega_2)} - \frac{\cos(m(\omega_1+\omega_2)T) \cos((\omega_1+\omega_2)T(m+1))}{(3\omega_1+\omega_2) \cos((\omega_1+\omega_2)T)} - \frac{\cos(mT(\omega_1+\omega_2)) \cos\left(\frac{(\omega_1+3\omega_2)T-2T(\omega_1+\omega_2)(m+1)}{2}\right)}{(3\omega_1+\omega_2) \cos(T(\omega_1+\omega_2))} \right\} \quad (2.25)$$

divide top and bottom by  $mT$ :

$$\frac{\omega_{2part}}{denom} = \lim_{m \rightarrow \infty} \left\{ \frac{1}{(\omega_1-\omega_2)T} - \frac{\cos\left(\frac{(\omega_1-\omega_2)T}{2}\right)}{T(\omega_1-\omega_2)} - \frac{\cos(m(\omega_1+\omega_2)T) \cos((\omega_1+\omega_2)T(m+1))}{mT(3\omega_1+\omega_2) \cos((\omega_1+\omega_2)T)} - \frac{\cos(mT(\omega_1+\omega_2)) \cos\left(\frac{(\omega_1+3\omega_2)T-2T(\omega_1+\omega_2)(m+1)}{2}\right)}{mT(3\omega_1+\omega_2) \cos(T(\omega_1+\omega_2))} \right\} \quad (2.26)$$

Once again, all terms but the first two involve  $\lim_{x \rightarrow \infty} \frac{\cos(x)}{x}$ , which goes to zero in the limit.

Therefore only the first two terms survives:

$$\frac{\omega_{2part}}{denom} = \frac{1}{(\omega_1 - \omega_2)T} - \frac{\cos\left(\frac{(\omega_1-\omega_2)T}{2}\right)}{T(\omega_1 - \omega_2)} \quad (2.27)$$

To find the magnitude of the Fourier component, we add the squares of the real and imaginary parts:

$$\begin{aligned}
\text{soln} &= \sqrt{\left(\frac{2 \sin\left(\frac{(\omega_1 - \omega_2)T}{2}\right)}{T(\omega_1 - \omega_2)}\right)^2 + \left(\frac{2}{(\omega_1 - \omega_2)T} - \frac{2 \cos\left(\frac{(\omega_1 - \omega_2)T}{2}\right)}{T(\omega_1 - \omega_2)}\right)^2} \\
\text{soln} &= \frac{2}{T(\omega_1 - \omega_2)} \sqrt{\sin^2\left(\frac{(\omega_1 - \omega_2)T}{2}\right) + \left(1 - \cos\left(\frac{(\omega_1 - \omega_2)T}{2}\right)\right)^2} \\
\text{soln} &= \frac{2}{T(\omega_1 - \omega_2)} \sqrt{4 \sin^2\left(\frac{(\omega_1 - \omega_2)T}{4}\right) \cos^2\left(\frac{(\omega_1 - \omega_2)T}{4}\right) + 4 \sin^4\left(\frac{(\omega_1 - \omega_2)T}{4}\right)} \\
\text{soln} &= \frac{4}{T(\omega_1 - \omega_2)} \sqrt{\sin^2\left(\frac{(\omega_1 - \omega_2)T}{4}\right) \left(\cos^2\left(\frac{(\omega_1 - \omega_2)T}{4}\right) + \sin^2\left(\frac{(\omega_1 - \omega_2)T}{4}\right)\right)} \\
\text{soln} &= \frac{4 \left| \sin\left(\frac{(\omega_1 - \omega_2)T}{4}\right) \right|}{T(\omega_1 - \omega_2)} = \left| \text{sinc}\left(\frac{(\omega_1 - \omega_2)T}{4}\right) \right| = \left| \text{sinc}\left(\frac{(\omega_1 - \omega_2)}{8f_{\text{mod}}}\right) \right|
\end{aligned}$$

But  $\omega_1$  and  $\omega_2$  are not in units of Hertz. To yield a result which will be useful in the lab, we define  $2\pi f_1 = \omega_1$  and  $2\pi f_2 = \omega_2$ .

$$\text{soln} = \left| \text{sinc}\left(\frac{\pi(f_1 - f_2)}{4f_{\text{mod}}}\right) \right| \quad (2.28)$$

where all frequencies are in Hertz. The value of  $\frac{\pi}{4} \simeq 0.79$  is within the margin of error of the experimental result of  $0.80 \pm 0.01$ , which is extracted from the slope of Figure 2.19.

## 2.4 Solid-state saturable absorber

The solid-state saturable absorber is a simple extension of the picosecond ring laser gyro presented above. The dye jet is simply replaced with a solid-state saturable absorber such as Schott Glass RG-830. The schematic of the system is shown in Figure 2.23.

The choice of a solid-state saturable absorber is based on the characteristics of the ring dye laser discussed earlier in this chapter: the sample must absorb about 2% at the lasing wavelength and the sample must be saturable. Since most of the Schott glasses have lifetimes in the picosecond region[80, 81], they should be capable of producing picosecond pulses. A potential problem with this system is two photon absorption. Most of these glass filters are simply an amalgam of semiconductors. The Red Glass series, RG, is a mixture of CdTe, CdS and CdSe. Because the glass consists of small spheres (radius = 5.3 nm at a volume fraction of .0016 for RG-830) [82] of these semiconductors, the glasses will have

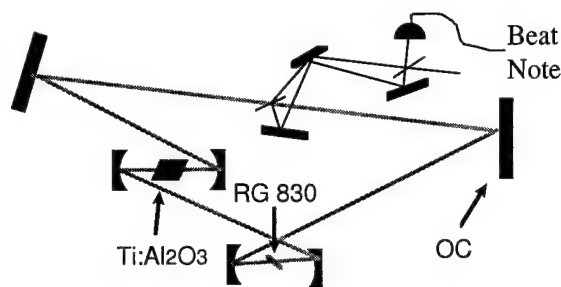


Figure 2.23: Setup of solid-state absorber experiments. Several absorber were tried, including the RG-830 that is displayed.

similar absorption features as the semiconductors. Most of these II-VI semiconductors have indirect gaps with parabolic bands and a long absorption tail, so the energy of 2 photons would be strongly absorbed by the solid-state glass. The long absorption tail should enable us to engineer a device with minimal absorption at the lasing wavelength.

Sarakura et al[83] used a piece of HOYA IR 76 to initiate Kerr-lens mode-locking in a Ti:sapphire laser. They ground the glass down to  $90\text{ }\mu\text{m}$  to simulate the thickness and absorption of a dye. They were successful in the implementation, but discovered that thermal effects in the glass led to instabilities in the laser output. To verify that it was in fact a thermal problem, they noted that blowing dry nitrogen on the glass increased the output of the laser. Our setup is similar to Sarakura's but sans prisms because we are not particularly interested in short pulses in this preliminary demonstration. We initially chose a 1-mm thick piece of RG-780 because it gives an absorption of 3% at 800 nm. This glass did not result in mode-locked operation. After checking the wavelength of the laser, we discovered that the wavelength had simply shifted to longer wavelengths where the absorption of the glass was lower. Since we have no way of controlling the wavelength of the laser, we selected a 1-mm thick piece of RG-830. With the laser operating at about 850 nm, this setup produces bidirectional, mode-locked pulses. If both the CW and CCW pulses are about as long as the glass, the mutual saturation should be optimized while minimizing the

2-photon loss. However, the pulses were much longer than the thickness of the glass; greater than 20 ps. Unfortunately the CW and the CCW directions were locked to one another therefore the beat note was zero and would not respond to mild rotations of the table. This is actually not surprising considering the theoretical work by Wax, Chodorow, Buholz and Chesnoy[35, 84, 85, 9] on lock-in in pulsed laser gyros.

Only when the table is rocked violently does the laser produce a beat note and then only for a short time before the laser locks once again. We also noticed the thermal problems that Sarakura mentioned. Because of these disadvantages, this system was not pursued.

### 2.4.1 Lock-in

There has been a lot of discussion about why the femtosecond dye laser does not lock. The three theories with widest acceptance are Doppler shifting, randomizing the scattering centers and four-wave mixing. The Doppler shift theory claims that scattered light is frequency shifted because of the longitudinal motion of scattering objects in the dye. The four-wave mixing theory states that the light scattered by the nonlinear grating is  $90^\circ$  out of phase with the opposing pulse and therefore will not interact with the opposing pulse (although this is true, it doesn't prevent the linear scattering from locking the laser). The random-scattering theory states that the phase of the scatters is randomized by the motion of the dye, which is identical to random, null-bias dithering (see Chapter 1).

Unfortunately in previous laser systems it has been impossible to separate the phenomena because they all occur in the dye jet. The solid-state system offers the unique ability to separate the phenomena because the Doppler shift can be set to zero by having a stationary sample. Also four-wave mixing occurs in an absorbing glass similar to the dye jet. In the preliminary experiments, the sample was stationary and the system locked. This indicates that it is the motion of the dye jet that causes the pulses to be independent. These results are preliminary and require a more systematic study to be conclusive. In an attempt to elucidate the problem, we mounted the glass on a moving audio speaker. This resulted in a beat note, which would seem to indicate that the CW and CCW pulses are decoupled; however, the motion of the speaker was not purely transverse to the optical path and contained a significant amount of wobble in the longitudinal direction. As discussed



earlier, a longitudinal motion will result in a false beat note. Because the beat note was exceedingly erratic with a bandwidth equal to the beat note of about 25 kHz, no positive conclusions can be drawn. Perhaps in future experiments the glass can be moved using a smoother piezo driven system (see Chapter 4) and finally clear up the question about why a mode-locked dye laser gyro doesn't lock.

## 2.5 Conclusion

In conclusion, this chapter introduced the world's first solid-state ring laser (albeit with a dye-jet absorber) that is not locked and requires no bias. Also a novel linear cavity design was unveiled and its use as a tool to measure optical nonlinearities was demonstrated. A new method of measuring the average beat note in a null-bias system was derived analytically and demonstrated experimentally. The flexibility of dithering a pulsed ring laser gyro was demonstrated, opening the doors to a plethora of experiments concerning the dithering of ring laser gyros. Finally, an all solid-state laser gyro was attempted. Modelocked pulses were achieved in the all solid-state laser gyro, unfortunately the counter-propagating modes were locked.

In the next chapter, Kerr-lens modelocking is explored as a method to achieve a pulsed laser gyro. The first setup also uses a saturable absorbing dye-jet, but in this case the dye-jet is used to initiate pulses and to define a crossing point. The mechanism that leads to femtosecond pulses is shown to be the Kerr-lens effect.

## Chapter 3

# Kerr-lens Mode-locked Ti:sapphire Laser

This chapter reports the first Kerr-lens mode-locked ring laser gyro. The chapter is divided into two different methods for defining the pulse crossing point: saturable absorber and mutual Kerr-lens. In the saturable absorber section, a novel method uses the Kerr-lens in the Ti:sapphire for both positive and negative feedback. In the second section, the use of mutual Kerr-lensing is demonstrated to define the pulse crossing point in a pulsed ring laser gyro.

### 3.1 Introduction

Since the advent of Ti:sapphire and Cr:LiSAF lasers there has been a move to eliminate the dye laser by replacing it with these new solid state materials. Perhaps the chief factor motivating this migration is the messiness of dealing with dye lasers, but there are other reasons including longer upper level lifetime and broader bandwidth, which result in higher power and shorter pulses. One motivation for this work is to demonstrate a solid-state femtosecond (fs) laser gyro, similar to the fs ring dye laser [13]. However, operation of a solid state ring laser with two uncoupled beams circulating in opposite directions is more challenging than it may appear, for the reasons outlined below.

In a continuous wave ring laser, bidirectional operation is only possible with inhomogeneously broadened gain media such as HeNe and CO<sub>2</sub>. In most lasers that have homogeneously broadened gain media such as dyes and solid-state lasers, the larger mutual gain saturation (as compared to self saturation) prevents bidirectional operation. Another problem with condensed matter lasers is that the "lock-in" or "dead band" problem plaguing most laser gyros tends to be exacerbated (larger scattering from condensed matter than from a gas). In most commercial laser gyros, operation within the dead band is prevented by giving the laser a constant motion (dithering).

Throughout this chapter we will use the following terms, which are defined here for clarity. Feedback refers to a coupling between a parameter of the laser pulse and the cavity losses. "Positive feedback" is a mechanism that causes the peak intensity of the laser to increase. "Negative feedback" is a mechanism that causes the peak intensity of the laser to decrease. The word "passive" refers to a device that is not actively driven by an external source. "Kerr-lens mode-locking" is an example of positive feedback. The Kerr-lens is a result of intensity dependent index of refraction. The Kerr-lens is positive for most crystals, which results in a positive lens. If an aperture is placed at the maximum decrease in beam waist due to the Kerr-lens, a positive feedback mechanism will result. This is the typical situation for Kerr-lens mode-locked lasers (i.e. Ti:sapphire, Nd:YAG and Cr:LiSaF). If an aperture is placed at the maximum increase in beam waist due to the Kerr-lens, a negative feedback mechanism will result. For the Ti:sapphire laser, the pulse energy remains roughly constant for different pulsewidths. Therefore a positive feedback mechanism that increases the peak pulse intensity will also decrease the pulsewidth. Likewise, for the Ti:sapphire laser, negative feedback will result in longer pulses.

## **3.2 Preventing phase coupling between counter-propagating beams**

The problem of injection locking between the two counter-propagating beams has been solved in the case of the dye laser by replacing continuous wave operation by ultrashort pulse

operation. There is no scattering of the clockwise circulating pulse into the counter-clockwise, if these pulses do not meet near a scattering medium. The pulses collide in the absorbing jet and opposite the jet in air. The same solution applies to a mode-locked Ti:sapphire laser, provided the following conditions can be satisfied: (i) bidirectional operation with two counter propagating pulse trains of the same intensity, and (ii) amplitude coupling without phase coupling away from any scattering surface to accurately define the pulse crossing points. A saturable absorber, similar to dye lasers, provides the required coupling: the pulse trains originate from standing wave noise spikes saturating the dye.

### 3.3 Preventing unidirectionality

A first approach to passively mode-locking the Ti:sapphire ring laser is through the use of saturable absorbers. Stable bidirectional operation was obtained using the dye IR-140. The pulse duration was approximately 1 ps. This is nearly a direct extension of the dye laser technology, with two quantitative differences. First, the Ti:sapphire and the dye absorber saturate at intensities that differ by three orders of magnitude. Therefore, the gain medium stores more energy than the absorber can saturate (typical dyes have a saturation energy density:  $w_s = \frac{h\nu}{\sigma} = 1 \text{ mJ/cm}^2$ , as opposed to  $1.2 \pm 0.15 \text{ J/cm}^2$  for Ti:sapphire[86]). Second, the amplitude modulation resulting in mode-locking is only applied to the leading edge of the pulse. Saturable absorbers are often referred to as a slow nonlinearity (the recovery time of the bleached dye is longer than the pulse duration), as opposed to the fast nonlinearity introduced by Kerr-lens mode-locking.

In the case of the dye laser, the dynamics of the gain and absorber in the mode-locked dye laser are carefully tuned such that the absorber eats away at the leading edge of the pulse and the gain eats away at the trailing edge by gain saturation. The lifetime of most dyes are on the order of nanoseconds (ns) while Ti:sapphire has a lifetime of  $3.2 \mu\text{s}$ . The lifetime is crucial because it determines the recovery time of the gain medium.

In the case of Kerr-lens mode-locking, the factor of 1000 ratio in lifetimes would appear to be an insurmountable problem since the system will want to operate such that the energy extracted is the greatest. A more intense single pulse will have more Self-

Phase Modulation (SPM) inside the Ti:sapphire, which will result in shorter pulses when there is negative Group Velocity Dispersion (GVD) inside the cavity (a result of the prism pairs). With an aperture in the cavity promoting Kerr-lens mode-locking; a shorter and more intense single pulse will experience less loss and therefore dominate over bidirectional pulses. A solution to this problem is to limit the intensity of the pulse. In the following sections we describe two successful implementations of passive negative feedback: (i) optical limiting using negative feedback through Kerr-lensing in Ti:sapphire (resulting in continuous bidirectional pulse trains) and (ii) optical limiting using an intracavity two-photon absorber, resulting in Q-switched mode-locked bidirectional operation.

### 3.4 Experimental setup

Figure 3.1 is a sketch of the experimental arrangement. The flat mirrors are either 0.1% or

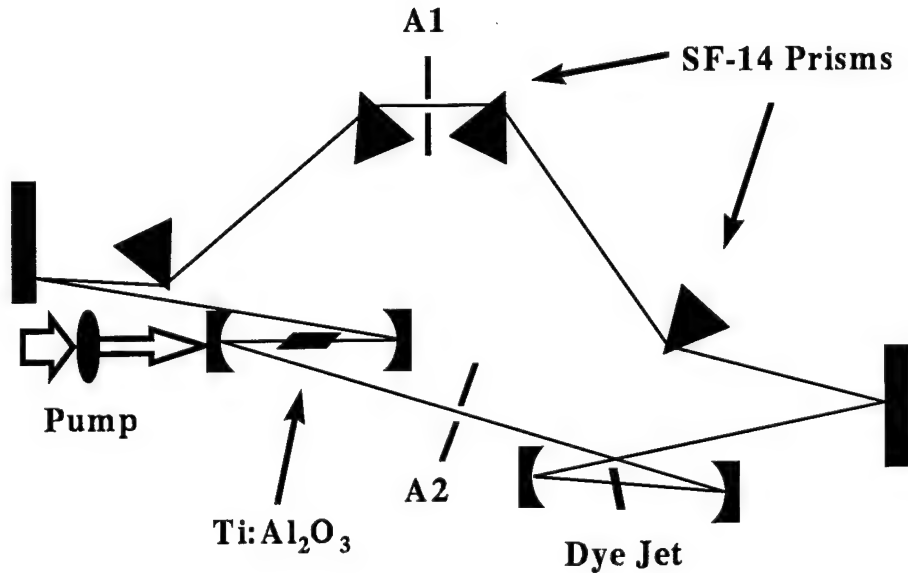


Figure 3.1: Experimental setup. A1 and A2 are apertures. Curved mirrors have radii of 10 cm. Flat mirrors have reflectivities 0.999 (left) and 0.987 (right). Brewster-cut 8 mm Ti:sapphire rod.

1.3% output coupling at 800 - 900 nm at zero degrees incidence. The curved mirrors have 10 cm radius of curvature. An angle of incidence of 10.5 degrees is chosen at the mirrors surrounding the gain medium to compensate for the astigmatism of the Brewster angled Ti:sapphire crystal. Since no astigmatism compensation can be obtained for the 40  $\mu\text{m}$  thick saturable absorber jet, the angle of incidence on the corresponding focusing mirrors is minimized. Four SF-14 prisms with 37 cm spacing between prism pairs are used to achieve an adjustable positive to negative GVD [87, 53]. The total perimeter of the ring is 253 cm resulting in pulses every 8.4 ns. The pump is a Coherent Innova 200 Ar<sup>+</sup> running on all lines and pumping at about 10 Watts. The high pump power is used to overcome the loss through a two photon absorber (i.e. 2 mm of CdS). Apertures A1 and A2 are vertical razor blades and are not used in all experiments. A1 is used for Kerr-lens mode-locking and A2 is used for passive negative feedback. A small amount of IR-140 dye was dissolved in ethylene glycol for the saturable absorber. Other dyes (i.e. HITCI and NDI) have also been used and do not seem to affect the pulse duration in the case of Kerr-lens mode-locked operation.

### 3.5 Unidirectional mode-locked pulses

The procedure for attaining mode-locked pulses is very simple. First close down the A1 aperture until it begins to affect the continuous wave output, and then realign for maximum power. Repeating this process will eventually lead to mode-locked pulses. This procedure was developed by theoretically analyzing the linear and nonlinear waists inside the cavity. The theoretical model is discussed later in this chapter. Using this procedure we are able to achieve between 125 - 140 fs pulses (autocorrelation width 220 fs). We did not optimize for the shortest pulses, since this is not a crucial aspect of this experiment. The outputs (CW and CCW) from the max-R reflector are detected on p-i-n photodiodes and are plotted in Figure 3.2. Based on the discussion above, it is not too surprising that the laser is unidirectional. What is surprising; however, is that the laser randomly switches direction. The characteristic switching time can be varied from hundreds of microseconds to seconds, depending on alignment, absorber dye concentration, and the number of bubbles in the dye jet. Notice that the CW and CCW beams are never on at the same time and therefore there

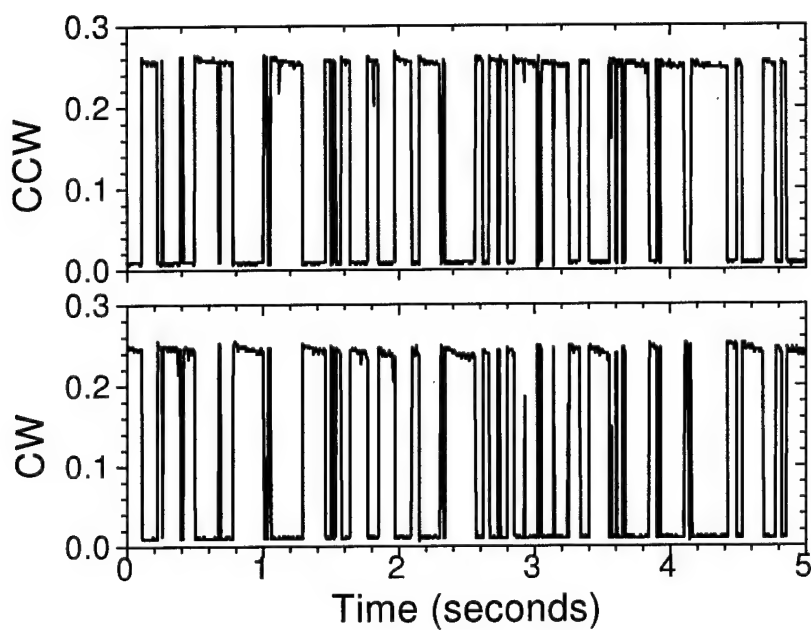


Figure 3.2: CCW (upper) and CW (lower) outputs of laser demonstrating switching of laser output. Note the laser is unidirectional at all times. Detectors are p-i-n photodiodes with a bandwidth of 1 GHz, although the digitizing oscilloscope's bandwidth is 1 MHz.

is never a standing wave saturation in the dye. The average output power is approximately the same in the CW and CCW directions at about  $175 \pm 10$  mW.

### 3.6 Q-switched mode-locked pulses

Increasing the dye concentration results in an increase of the ratio of saturable to linear losses. Therefore, one might expect to achieve bidirectional operation by increasing the concentration of the absorber solution. Over an extremely large range, adding dye had no qualitative effect to the output of the laser, which has been reported previously[56, 88, 89]. Eventually the continuous wave power began to decrease and finally shut off completely when the losses exceeded the gain. At this level of dye concentration, the laser begins pulsating rather erratically. By adjusting aperture A1 the output becomes more periodic, but the output on the photodiode was a factor of ten larger! In fact the output is Q-switched mode-locked as can be seen in Figure 3.3. The inset of Figure 3.3 shows the mode-locked pulse train underneath one of the Q-switched pulses. Notice that the Q-switched train is alternating in each direction (one train clockwise, followed by a counterclockwise train, etc.). The alternating output does not have a gyro response because the laser is unidirectional at any given period of time. The autocorrelation width is 3.3 ps, corresponding to a pulse duration of 2.3 ps (assuming Gaussian shaped pulses). The envelope of the Q-switched mode-locked trains is 0.6  $\mu$ s and they are separated by about 4  $\mu$ s. Since the lifetime of Ti:sapphire is 3.2  $\mu$ s, the Q-switching is most likely a result of relaxation oscillations. Krausz[57] analyzed the typical Ti:sapphire laser and came to the conclusion that it should not Q-switch. Our cavity has increased linear and nonlinear losses which is significantly different than the theoretical cavity analyzed by Krausz. Xing[90] has reported Q-switched mode-locked operation in a Ti:sapphire laser that has a Q-switch period that is dependent on the translation of a curved focusing mirror. Xing believes that the translation of this mirror affects the losses in the cavity and therefore changes the cavity lifetime.



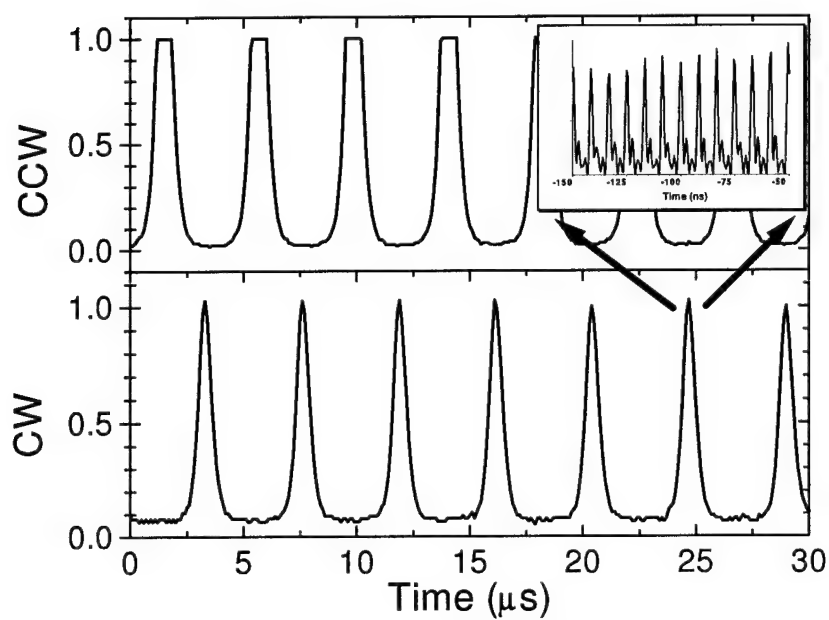


Figure 3.3: CCW (upper) and CW (lower) pulses demonstrating Q-switch pulses. The period of pulses varied from 4 to 7  $\mu\text{s}$ . The inset shows a subset of the mode-locked pulse train within the Q-switch envelope.

### 3.6.1 Passive negative feedback

One standard technique to stretch the Q-switched mode-locked train, while compressing the individual pulses, is passive negative feedback [91]. As an alternative to the GaAs used as a two-photon absorber in the Nd:YAG laser [91] we placed a 2-mm thick sample of CdS in the cavity (see Figure 3.4) for an energy limiter. The 2-photon fluorescence of the CdS is

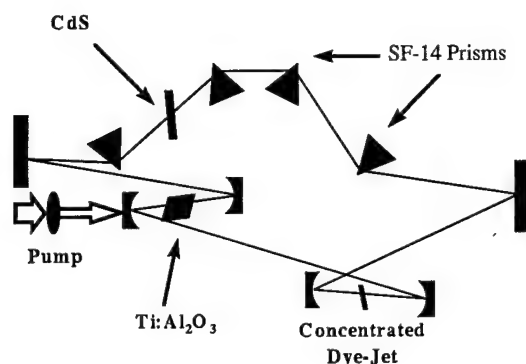


Figure 3.4: Experimental arrangement for bidirectional Q-switched mode-locked pulses.

clearly visible to the naked eye in a well lit room. With the highest dye concentration and the energy limiter (CdS), the two pulse trains from each direction are in phase, see Figure 3.5. The photodiode measurement cannot resolve the crossing point of each pulse train. One method to determine if the pulses are crossing in the dye is to combine the CW and CCW outputs onto a detector and look for a beat signal. Initially a beat note of 2 kHz with a 2 kHz bandwidth was observed; after a significant amount of work and a clean dye solution a beat note of 100 Hz was obtained, see Figure 3.6. This mode of operation has synchronized pulse trains in opposite directions, and a gyro response. It may be of interest in experiments requiring probing of samples with high intracavity peak powers. It is rather surprising that the laser is able to 'remember' the phase between the CW and CCW pulse trains in between Q-switched pulses. Recent theoretical results[92] predict that the laser is still mode-locked in between the Q-switched pulse, albeit at a very small amplitude. These mode-locked pulses in between the Q-switched pulses has also been confirmed experimentally[93]. Another mode of operation, with continuous mode-locked trains, is described in the next section.

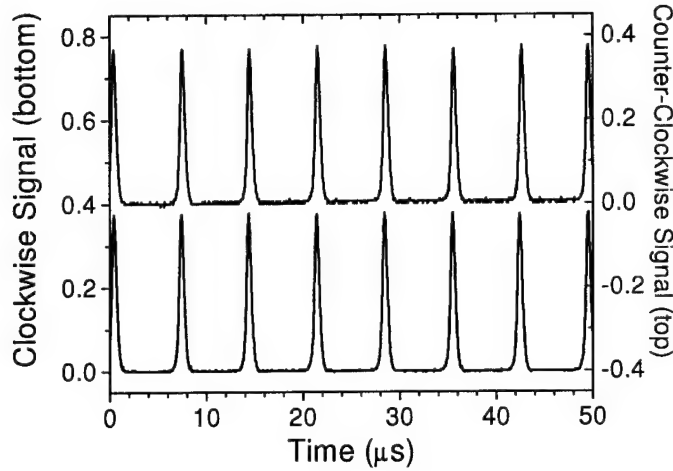


Figure 3.5: CW and CCW outputs in Q-switched operation are temporally overlapped.

## 3.7 Continuously mode-locked bidirectional operation

### 3.7.1 Cavity analysis

Kerr-lensing itself can be used to achieve negative as well as positive feedback. We use a simple ABCD method to model the laser and include the nonlinearity of the sapphire by inserting a lens matrix of the appropriate focal length[74]:

$$f_{nl} = \frac{1}{a} \frac{n_0 \pi w_0^4}{8 n_2 P d} \quad (3.1)$$

where  $w_0$  is the waist in the sapphire,  $n_2$  is the nonlinear index of refraction,  $P$  is the peak power,  $d$  is the length of the crystal and  $a$  is a constant on the order of 1 to 4. The constant,  $a$ , is a result of approximating the Gaussian beam profile to a parabolic lens equation. If a one-to-one correspondance is made in the Taylor series expansion, then the  $a$ -factor is 1. A recent empirical fit found the value of  $a$  to be 1.723 [1, 2]. Figure 3.7 is a plot of the waist in the 8 mm Ti:sapphire crystal. Clearly using the waist,  $w_0$ , is not a good approximation over the length of the crystal. We want to keep the analysis as simple as possible for rapid calculations, so we would like to use only one thin lens to approximate the nonlinearity. Equation 3.1 is a good approximation for small nonlinearities ( $P < P_{cr}$  (critical power)) and

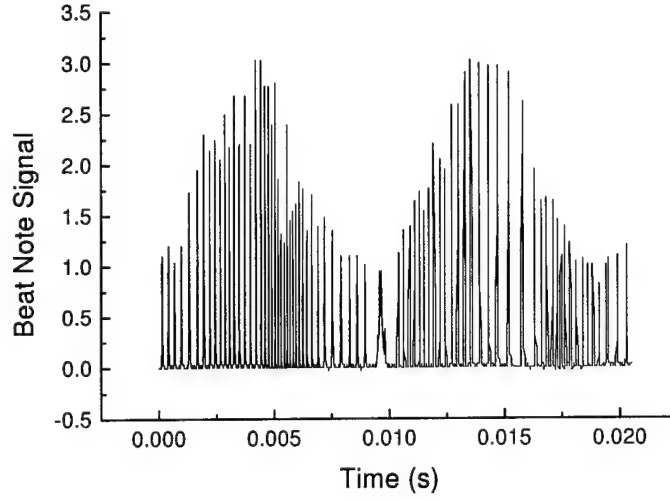


Figure 3.6: Beat note of Q-switched pulses. Coupling is DC because the signal is pulsed. Notice the contrast is 60%. There are more than 3000 pulses in this plot and only 2048 data points. This undersampling explains the aperiodic nature of Q-switched pulses.

thin ( $d < z_0$  (Rayleigh range)) samples. For an infinitesimal slab,  $dz$ , the nonlinear lens is given by:

$$f_{nl} = \frac{n_0 \pi w^4(z)}{a 8 n_2 P} \frac{1}{dz} \quad (3.2)$$

$$\frac{1}{f_{nl}} = \frac{a 8 n_2 P}{n_0 \pi w^4(z)} dz \quad (3.3)$$

The ABCD matrix method calculates the  $\frac{1}{q}$  beam parameter. From the beam parameter, we extract the radius of curvature of the beam,  $R_1$ , and the beam waist,  $w_1$ . The rest of the beam characteristics can be calculated:

$$\begin{aligned} z_1 &= \frac{R_1}{\left(\frac{\lambda R_1}{n_0 \pi w_1^2}\right)^2 + 1} \\ w_0 &= \frac{w_1}{\sqrt{1 + \left(\frac{n_0 \pi w_1^2}{\lambda R_1}\right)^2}} \\ z_0 &= \frac{n_0 \pi w_0^2}{\lambda} \\ w(z) &= w_0 \sqrt{1 + \left(\frac{z}{z_0}\right)^2} \end{aligned}$$

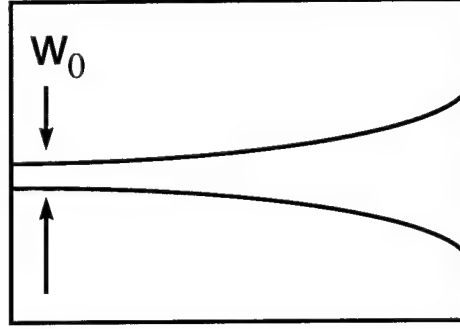


Figure 3.7: Plot of the beam waist in the Ti:sapphire crystal. The length of the crystal is about 10 times longer than the confocal parameter.

Integration over the length of the crystal,  $d$ , from  $z_1$  to  $z_2$  yields:

$$\begin{aligned} \frac{1}{f_{nltotal}} &= \frac{a8n_2P}{n_0\pi} \int_{z_1}^{z_2} \frac{dz}{w^4(z)} = \frac{8n_2P}{n_0\pi w_0^4} \int_{z_1}^{z_2} \frac{dz}{\left(1 + \left(\frac{z}{z_0}\right)^2\right)^2} \\ \frac{1}{f_{nltotal}} &= \frac{a8n_2P}{n_0\pi w_0^4} \frac{z_0}{2} \left( \frac{z_0 z_2}{z_0^2 + z_2^2} + \arctan\left(\frac{z_2}{z_0}\right) - \frac{z_0 z_1}{z_0^2 + z_1^2} - \arctan\left(\frac{z_1}{z_0}\right) \right) \\ \frac{1}{f_{nltotal}} &= \frac{a8n_2P}{n_0\pi w_0^4} d_{eff} \end{aligned}$$

Where  $d_{eff}$  is the effective length of the crystal. It is instructive to plot  $d_{eff}$  as a function of crystal length. Figure 3.8 assumes  $w_0 = .001$  cm and  $z_1 = 0$ , which means that the waist is at the left edge of the crystal. For lengths longer than the Rayleigh range, the nonlinearity approaches a constant. Typically the beam waist is near one edge of the crystal, such that small changes in the beam parameters can translate into large changes in the nonlinear lens.

So far only the strength of the nonlinear lens has been discussed. As with any lens, the location of the lens will also play an important role in determining the beam waist. The location,  $\bar{z}$ , of the nonlinear lens in the crystal is determined by calculating the centroid of

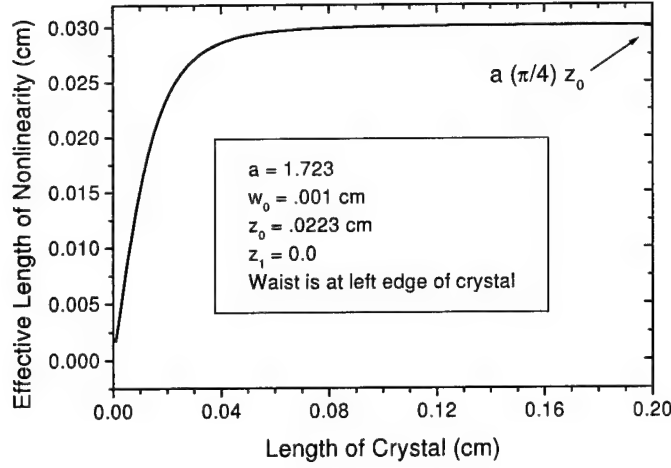


Figure 3.8: Plot of effective crystal length versus actual crystal length. Note for lengths longer than the Rayleigh range, the effective length is approximately a constant.  $a$  is an empirically determined constant[1, 2].

the nonlinear lens:

$$\begin{aligned}
 \bar{z} &\equiv \frac{\int \frac{z}{w(z)^4} dz}{\int \frac{1}{w(z)^4} dz} \\
 \bar{z} &\equiv \frac{\int_{z_1}^{z_2} \frac{z}{\left(1 + \left(\frac{z}{z_0}\right)^2\right)^2} dz}{\int_{z_1}^{z_2} \frac{dz}{\left(1 + \left(\frac{z}{z_0}\right)^2\right)^2}} \\
 \bar{z} &\equiv \frac{\frac{z_0^4}{2(z_0^2 + z_1^2)} - \frac{z_0^4}{2(z_0^2 + z_2^2)}}{\frac{z_0}{2} \left( \frac{z_0 z_2}{z_0^2 + z_2^2} + \arctan\left(\frac{z_2}{z_0}\right) - \frac{z_0 z_1}{z_0^2 + z_1^2} - \arctan\left(\frac{z_1}{z_0}\right) \right)} \\
 \bar{z} &\equiv \frac{\frac{z_0^4}{2(z_0^2 + z_1^2)} - \frac{z_0^4}{2(z_0^2 + z_2^2)}}{d_{eff}}
 \end{aligned}$$

Figure 3.9 is a plot of  $(\bar{z} - z)$ , the location of the nonlinear lens with respect to the center of the crystal, as a function of the location of the crystal with respect to the beam waist.

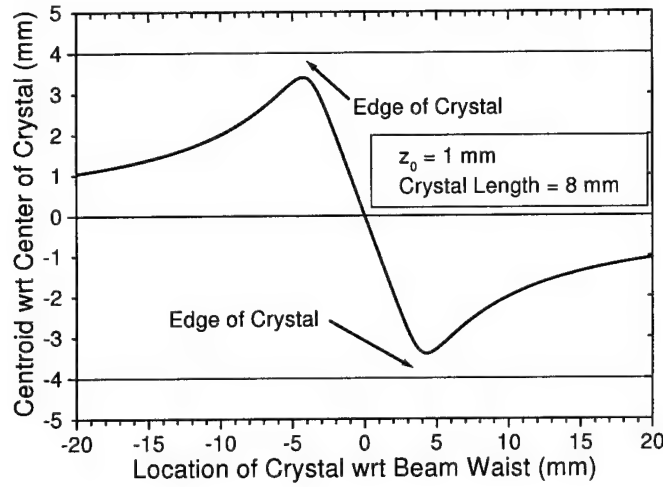


Figure 3.9: Location of the nonlinear lens plotted as a function of the location of the crystal with respect to the beam waist.

Notice that the location of the nonlinear lens is always within the crystal.

Although the calculation can be accomplished by only using one set of beam parameters, we feel that the calculation is easier with two sets, one at the entrance to the crystal ( $z_1$ ) and the other at the exit ( $z_2$ ). To within 1% of error in beam waist, the nonlinearity can be ignored when the waist,  $w(z)$ , is calculated. An iterative approach can be used where the waist is first calculated ignoring the nonlinearity and then the waist in the cavity is recalculated using the new waist. This waist can then be recalculated until the desired precision is reached. There is; however, no reason to iterate more than once, as can be seen in Figure 3.10. Notice that the first iteration produces a correction of less than 0.5% from the waist calculated without the nonlinearity. After the first iteration, the change is less than the accuracy of the first order approximation used in equation 3.1. Figure 3.11 is a plot of the waist inside the cavity starting and ending in the middle of the Ti:sapphire. The abscissa is the distance from the center of the Ti:sapphire rod as you walk around the perimeter of the laser in a CCW direction. The solid line is the calculation without the nonlinearity and the dashed line includes the nonlinear focus. The dimensions used in the numerical model are taken directly from the laser in the laboratory (within the margins of

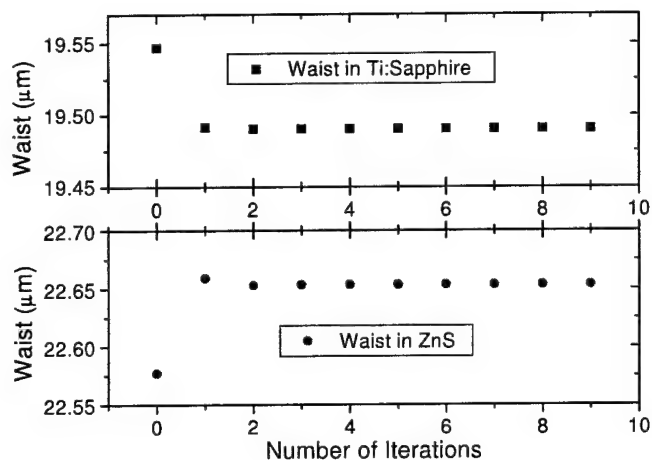


Figure 3.10: Beam waist in the nonlinear crystals, Ti:sapphire and ZnS, as a function of the number of computer iterations.

error). Notice that the numerical model correctly predicts the nonlinear waist to be smaller than the linear waist at the aperture A1, which is required for Kerr-lens mode-locking. This waist was verified experimentally by scanning a pinhole across the beam at several locations outside the cavity. The experimental value of  $0.033 \pm .005$  cm is reasonably close to the computer model (larger by about  $11 \mu\text{m}$ ), especially when you consider all of the approximations made in the model and the difficulty in accurately measuring the dimensions of the cavity and the circulating power. As you can see from Figure 3.11, a second aperture located virtually anywhere in the cavity can act as an optical limiter because the nonlinear waist is larger than the linear waist everywhere in the cavity except at A1. For example an aperture at A2 will induce larger losses for a more intense pulse because it will have a larger waist at A2.

### 3.7.2 Experimental results

Before we tried the aperture at A2, we replaced the dye with a new dilute solution of IR-140. Then we reestablished unidirectional mode-locking by closing the slit at A1 and then aligning for maximum power. Repeating this procedure eventually leads to mode-locked



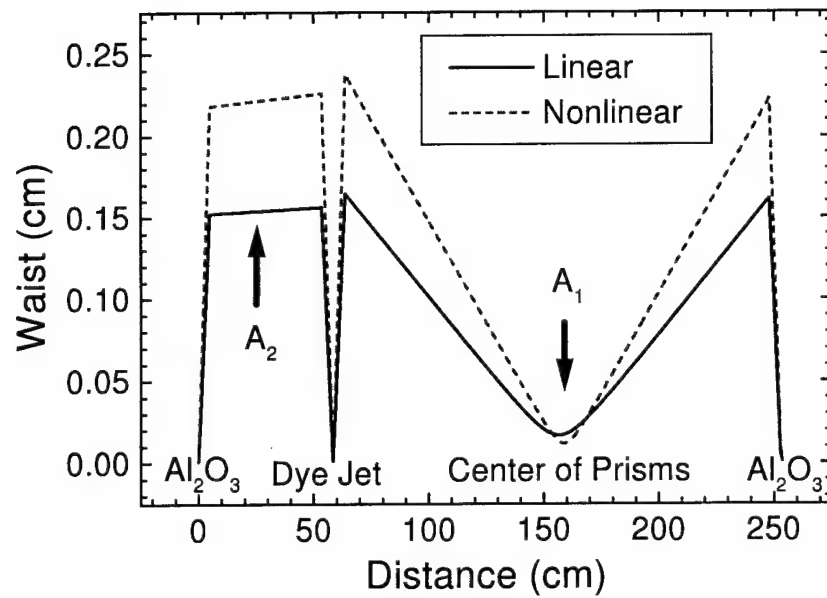


Figure 3.11: Theoretical graph of linear and nonlinear cavity waists plotted versus distance in the cavity. The distance is measured from the center of the Ti:sapphire rod in the CCW direction. A1 is the location of the Kerr-lens aperture. A2 is the location of the aperture for passive negative feedback. The plot begins and ends in the Ti:sapphire crystal.

pulses. It should be pointed out that the location of A1 is chosen very carefully, such that the continuous-wave waist and the mode-locked waist occur in the same location in the cavity. This procedure will only work for the setup specified in Figure 3.11. As the aperture at A2 is closed the autocorrelation decreases in height and increases in width, just as predicted. Suddenly the autocorrelation will drop to fixed lower level and become more stable. The laser is now operating bidirectionally. The autocorrelation traces shown in Figure 3.12 were obtained immediately after one another with the only change in the experiment being the closing of aperture at A2 by about 0.05 cm, which results in bidirectional operation. Notice

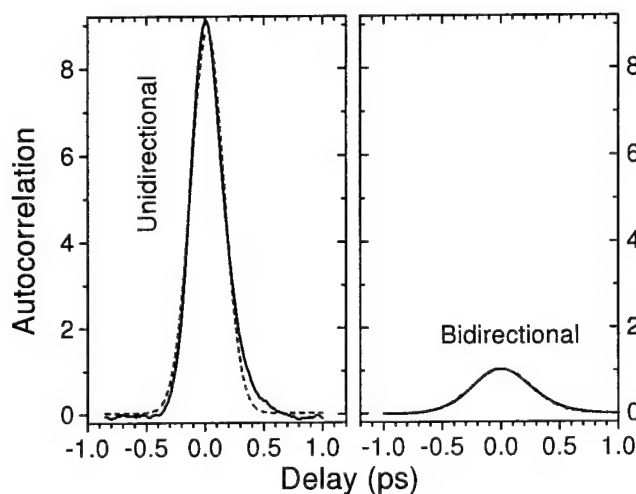


Figure 3.12: Background free intensity autocorrelation. Traces obtained immediately after one another, only slit A2 was closed by 0.05 cm for bidirectional operation. The dashed lines are a Gaussian fit to the autocorrelation. The Gaussian pulsewidths are 220 fs for unidirectional and 420 fs for bidirectional.

that the pulsewidth has increased a factor of 2 (measured to be 420 fs) and the pulse height has decreased by a factor of 9. The autocorrelator was a type-II KDP crystal configured for background free intensity autocorrelations. The output of the photodiodes is shown in Figure 3.13 in stark contrast to the unidirectional output in Figure 3.2. There are still about a dozen dropouts in 5 seconds, but this is acceptable for many applications. The dropouts are a result of the laser switching to unidirectional operation, which may be a result of intensity fluctuations. Replacing the hard apertures (razor blades) with apodized

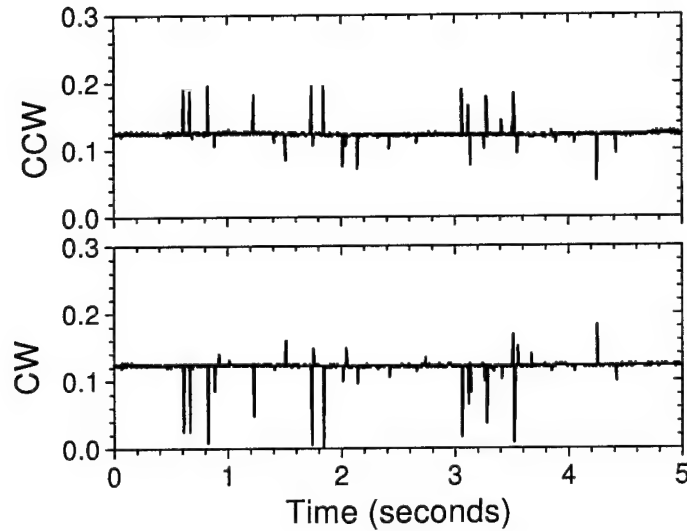


Figure 3.13: CCW (upper) and CW (lower) output demonstrating the lack of switching as compared with Figure 3.2. The detectors and time base are the same as Figure 3.2. The dropouts are a result of unidirectional operation, which explains why the spikes are negatively correlated.

apertures may result in more stable operation. We also verified that A2 could be located at two other locations in the cavity: at 70 cm and at 120 cm (see Figure 3.11).

Our application is to use the ring laser for sensitive intracavity phase measurements[94, 76]. So we once again measured the beat note by combining the CW and CCW pulses on a slow detector. The beat note demonstrated good sinusoidal character (see Figure 3.14) for short periods of time (milliseconds); however, a 15 minute average collected on a frequency spectrum analyzer showed a bandwidth of 10 kHz. To our surprise the beat frequency was about 70.8 kHz in Figure 3.14 and could be varied from about 20 kHz to 150 kHz depending on alignment. The high beat note is surprising because we had earlier measured a beat note of 100 Hz in a Ti:sapphire linear cavity[94, 95] and 10 Hz in a Ti:sapphire ring dye laser (see Chapter 2).

We again returned to the numerical model and assumed that the energy in each pulse increased by 10-20% as it passed through the gain medium. The figure of 10-20% is estimated by measuring the power reflected off of all Brewster surfaces inside the cavity and

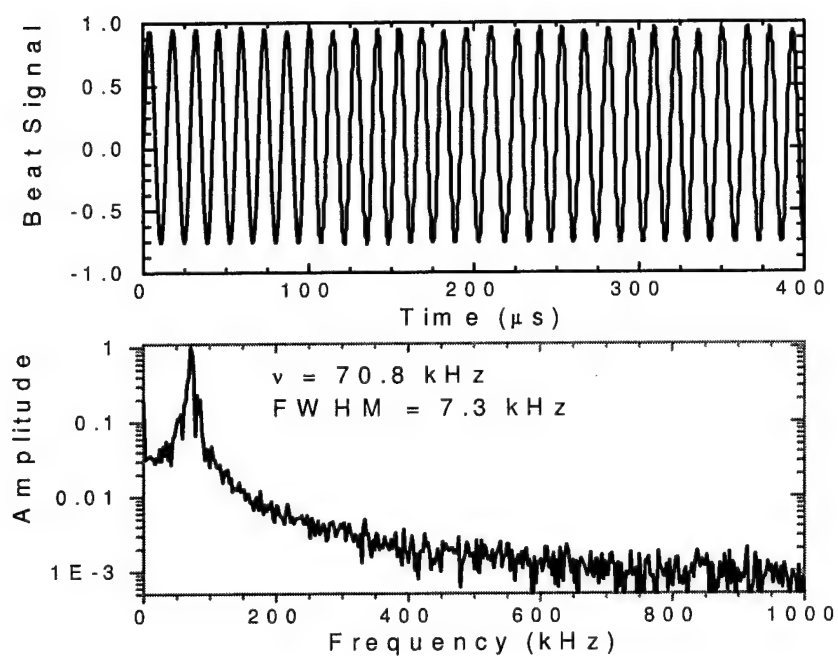


Figure 3.14: Difference frequency of the combined CW and CCW pulses. The Brewster reflections from two prisms are recombined after an appropriate delay onto a slow detector.

assuming 5-10% scattering loss from the mirrors, absorber jet, prisms and apertures. For Kerr-lens mode-locking, the waist has to be located asymmetrically within the gain medium to optimize the nonlinear lens. Because both the power and the waist vary as the pulse travels through the gain, the change in the index of refraction will be different for the CW and the CCW pulse. Figure 3.15 will help clarify the difference in the nonlinear phase

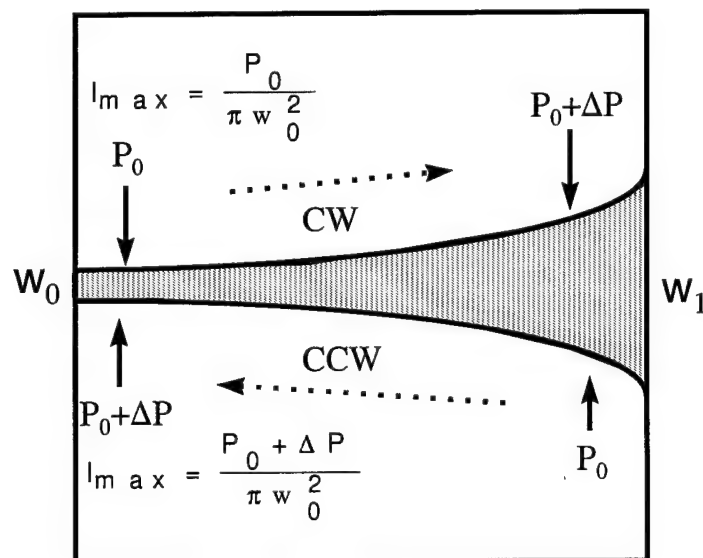


Figure 3.15: Beam waist in Ti:sapphire crystal. The upper equations apply for the CW pulse, and the lower equations are for the CCW pulse. Because of the asymmetry, the peak intensity will be less for the CW pulse.

shifts. The equations in Figure 3.15 that are above the beam waist are for the CW pulse and the equations below the waist are for the CCW pulse. Notice that the peak intensity is greater for the CCW pulse than for the CW pulse, which translates into a greater change in index for the CCW pulse. This slight difference in the index of refraction will result in a slight difference in the optical path length of the cavity, which shifts the longitudinal mode spacings. The beat frequency,  $\Delta\nu$ , resulting from a change in the perimeter,  $\Delta P$ , of a ring laser is given by:

$$\frac{\Delta\nu}{\nu} = \frac{\Delta P}{P}$$

$$\Delta\nu = \frac{\nu}{P} n_2 \Delta I_{peak} \ell$$

$$\begin{aligned}
\Delta\nu &= \frac{\nu n_2 \Delta P_{peak} \ell}{P \pi w_0^2} \\
\Delta\nu &= \frac{\nu n_2 \Delta P_{peak} 2.7 z_0}{P \frac{\pi w_0^2}{\lambda} \lambda} \\
\Delta\nu &= \frac{2\nu n_2 \Delta P_{ave} \tau_{round-trip}}{P \lambda \frac{\tau_{pulse}}{P}} \\
\Delta\nu &= \frac{2\nu n_2 \Delta P_{ave}}{\lambda P c} \frac{P}{\tau_{pulse}} \\
\Delta\nu &= \frac{2n_2 \Delta P_{ave}}{\lambda^2 \tau_{pulse}} \\
\Delta\nu &= \frac{2 \left( 3 \times 10^{-16} \frac{cm^2}{W} \right) (0.22W)}{(8 \times 10^{-5} cm)^2 (4 \times 10^{-12} s)} \sim 70 \text{ kHz}
\end{aligned}$$

where  $\nu$  is the optical frequency and  $P$  is the perimeter of the ring cavity. The numerical model predicts a beat frequency of 50 - 150 kHz for the cavity described above, which agrees well with the beat note observed in the laboratory. The beat frequency in the numerical model was strongly dependent on the cavity parameters, as was the laser in the laboratory.

The fact that a first-order cross-correlation produces a beat note, implies that the pulses are crossing in the dye jet. The first-order cross-correlation does not give much information about the jitter in the crossing point. To determine the jitter in the crossing point we used a second-order non-interferometric cross-correlation. It is convenient to use the pulses from the first-order cross-correlator (the beat note detector) for the second-order auto and cross-correlations, see Figure 3.16 for the experimental arrangement. When the  $\lambda/2$  waveplate is in position A, the CW (CCW) autocorrelations can be recorded by blocking the CCW (CW) beam in the first-order autocorrelator. To record the second-order cross-correlation, the  $\lambda/2$  waveplate is moved to position B. The second-order cross-correlation is shown in Figure 3.17 as the solid line. Also plotted in Figure 3.17 are the CCW and CW autocorrelations. Although this graph doesn't resolve the differences in the pulsewidths, an average of many pulsewidths showed the CW pulse to be slightly shorter than the CCW pulse and the cross correlation was on average in between the CW and the CCW pulses. This implies that there is very little jitter in the crossing point of the CW and CCW pulses.

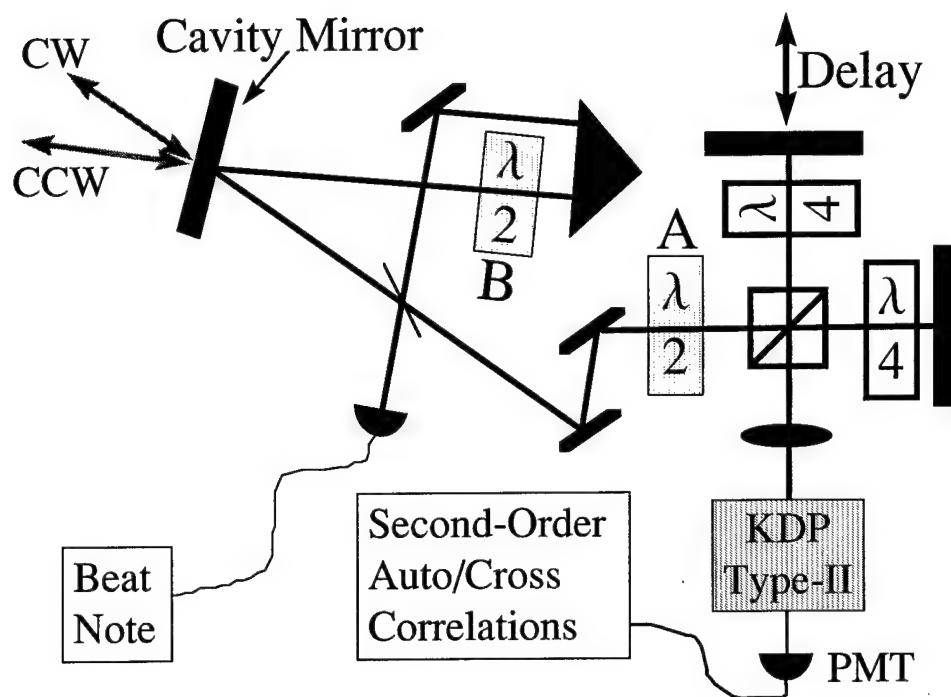


Figure 3.16: Setup for beat note detection, auto and cross correlations. The  $\lambda/2$  waveplate at locations A and B control the auto and cross correlations, respectively. The beam combiner for the beat note detection is a 50/50 beam splitter, while the beam splitter/combiner for the auto/cross correlator is a polarizing beam splitter.

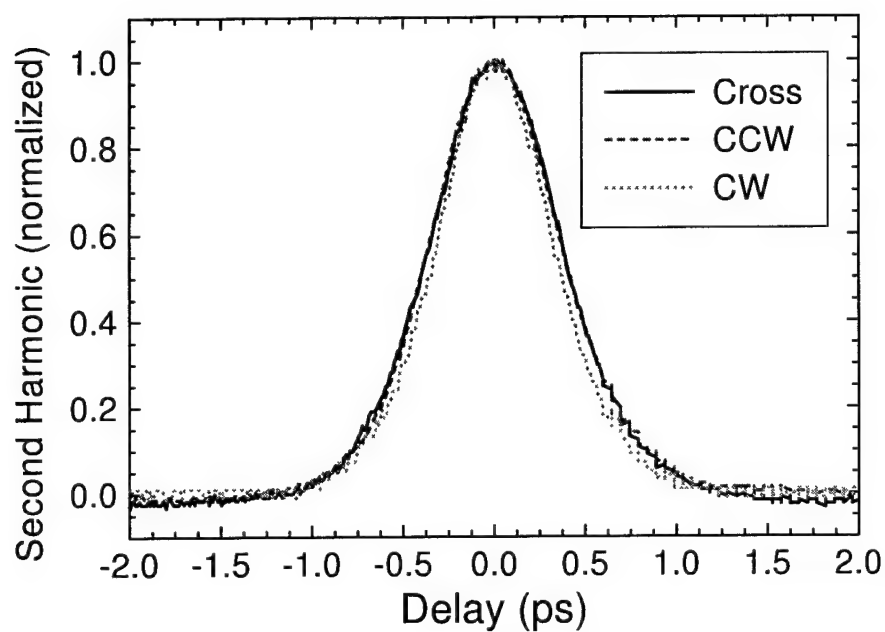


Figure 3.17: Auto and cross correlations of CW and CCW pulses. The cross correlation lies between the autocorrelations of the CW and CCW pulses, which implies no timing jitter between the pulses with a margin of error of 30 fs.



The maximum amount of jitter is 30 fs, which is a statistical error from the fluctuations in the individual pulsewidths. If we assume Gaussian pulses with durations  $\tau_1$  and  $\tau_2$ , the cross-correlation is given by:

$$\int_{-\infty}^{\infty} e^{-2\left(\frac{t}{\tau_1}\right)^2} e^{-2\left(\frac{t-\tau}{\tau_2}\right)^2} dt = e^{-2\frac{\tau^2}{\tau_1^2 + \tau_2^2}}$$

Notice that if  $\tau_1 = \tau_2$ , we recover the autocorrelation and the  $\sqrt{2}$  factor in the pulsewidth. For our experiment, we define:

$$\begin{aligned} \text{CW Autocorrelation width} &\equiv \sqrt{2} \tau_{cw} \\ \text{CCW Autocorrelation width} &\equiv \sqrt{2} \tau_{ccw} \\ \text{Cross-correlation width} &\equiv \sqrt{\tau_{cw}^2 + \tau_{ccw}^2} \end{aligned}$$

If  $\tau_{cw} < \tau_{ccw}$  then the order of correlation widths will be CW-autocorrelation < cross-correlation < CCW-autocorrelation.

This concludes the study of the first Kerr-lens mode-locked femtosecond ring laser gyro. In the next section, we will remove the absorbing dye jet and replace it with a nonlinear crystal. This new method of establishing a crossing point in a Kerr-lens mode-locked ring laser is called the mutual Kerr-lens effect.

## 3.8 Mutual Kerr-lens mode-locked

### 3.8.1 Introduction

The absorbing dye jets discussed in the previous chapters and sections have a few disadvantages compared to an all solid-state system. It is not practical to put a dye jet into a remote object (like a satellite) for rotation sensing because of the high maintenance of the dye. The dye jet is a thin ( $< 100 \mu m$ ) ribbon that is free to move. A moving dye jet can result in increased noise in the beat note, and can limit the ultimate sensitivity of the device.

Another disadvantage to the dye jet is called pulse dropout, which is a result of bubbles in the dye jet which cause the laser to shut off for a moment. Pulse dropouts will also limit the sensitivity of the device. The laser may turn off for  $\mu s$  to  $ms$ . When the laser reaches

threshold again, there is no memory of the phase of the previous beat note. Therefore, at every pulse dropout there will be an arbitrary phase jump in the beat note. These arbitrary phase jumps will limit the device's sensitivity by adding bandwidth to the beat note.

For these reasons it would be advantageous to move to a solid-state laser system. Since all of the experiments in this dissertation involve an  $\text{Ar}^+$  laser, none of these systems are 'all solid-state.' However, most of the experiments presented here could be moved to an all solid-state system by replacing the  $\text{Ar}^+$  with a solid state system such as: a diode pumped, frequency doubled, continuous wave, Nd:YAG laser; a diode pumped, mode-locked, Nd:YAG laser; a diode pumped Cr:LiSAF laser; or perhaps simply a diode system. One solid-state system has already been presented in Chapter 2, the solid-state saturable absorber. Next we will discuss the solid-state system that uses and mutual Kerr-lens mode-locking to stabilize the pulse crossing point. The OPO is also an all solid-state design, but because no experimental data was recorded for the OPO during this dissertation work, the OPO design will be discussed in Chapter 4.

### 3.8.2 Theory

The formation of multiple pulses in the Ti:sapphire laser is well documented[96, 97] and was observed in our lab[97]. Multiple pulses are difficult to control experimentally, but seem to depend on having low output coupling, because the soliton model predicts a quantization of the soliton amplitude. The multiple pulses have previously been reported as higher order solitons[96], which also supports our experimental findings that multiple pulse operation requires low output coupling. Jeff Nicholson recently modeled some experimental work done by Ming Lai concerning multiple pulses inside the laser cavity[97]. His simulations showed that it is possible to have an enhanced Kerr-lens if the pulses collide in the Ti:sapphire. Another group has also verified this same theoretical result[98]. This is a surprising result because the mutual Kerr-lens should be much smaller than the self Kerr-lens. In air a 100 fs pulse is  $30\text{ }\mu\text{m}$  long, which will be stretched to  $53\text{ }\mu\text{m}$  inside the sapphire. The colliding pulses will only have an interaction length of  $100\text{ }\mu\text{m}$ . When you compare this to the 8 mm length of the crystal, the colliding term should only be approximately 2.5% of the single

pulse interaction.

$$\frac{\Delta n_{colliding}}{\Delta n_{single-pulse}} \sim \frac{interaction\ length}{crystal\ length} \frac{2Intensity}{Intensity} \sim \frac{0.1}{8} 2 = 2.5\%$$

The factor of 2 is a result of averaging the electric fields interfering in the crystal (the intensity periodically varies from  $4 \times Intensity$  to zero). Since the Kerr-lens has only a small effect on the cavity parameters, it is hard to believe that an additional 2.5% would have any noticeable effect.

A complete analysis will require the ABCD matrix calculation and a little more care than the estimation above. For bidirectional operation to be stable, we require bidirectional pulses to experience less loss than: 1) single-pulses, 2) continuous-wave operation, 3) double-pulses in the same direction. Because the lifetime of Ti:sapphire is much longer than the round-trip time, it is assumed that the total energy extracted from the cavity in one round-trip is constant regardless of the mode of operation. For a 'best-case' scenario, let us further assume that the pulsewidths are equal (from the previous work this is not such a good assumption). Together these assumptions require that the peak power in the bidirectional case be less than half the power in the single-pulse case. The nonlinear index is also modified by the colliding pulses:

$$\Delta n_{ccw} = n_2 (I_{ccw} + 2I_{cw})$$

$$\Delta n_{cw} = n_2 (I_{cw} + 2I_{ccw})$$

The factor of 2 in front of the counter-propagating beam is a result of the pulses being distinguishable[99, 100]. By assuming: 1) equal intensity in the counter-propagating fields, 2) similar waists and 3) the pulsewidth is approximately the width of the crystal yields:

$$\Delta n_{bidirectional} \sim \frac{3}{2} \Delta n_{single}$$

Therefore there is ample room in the nonlinearity to distinguish between single-pulse operation and bidirectional operation. For a laser gyro, we require that the pulses cross outside of the gain medium to prevent lock-in from scattering off a gain grating in the Ti:sapphire. To enhance the mutual Kerr-effect, we chose a high  $n_2$  crystal, ZnS, which has a nonlinear index

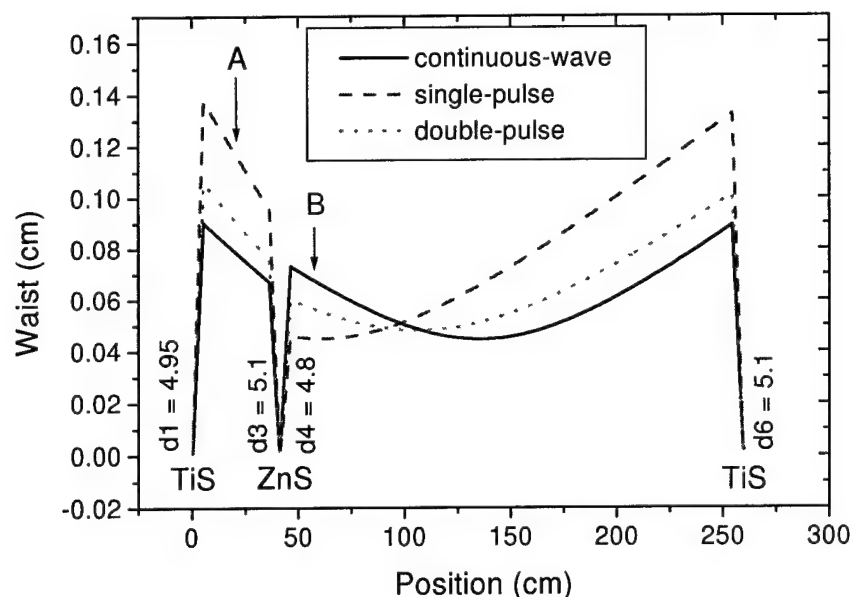


Figure 3.18: Beam waist as a function of position in the cavity. The calculation begins and ends in the Ti:sapphire crystal, TiS. Three different cases are plotted: continuous-wave, single-pulse and bidirectional pulses.

about 50 times that of Ti:sapphire. We return to the ABCD matrix method to determine where the slits should be located for bidirectional operation. We expect the simulation to only yield qualitative results because of the numerous approximations. Figure 3.18 is a plot of the beam waist as a function of position in the cavity. Notice that a slit at position B will increase the losses for continuous-wave operation (positive feedback) and slits at position A will limit single-pulse operation (negative feedback). Judicious use of these two slits should yield bidirectional pulses.

There are differences in the linear laser analyzed theoretically[98, 97] and a bidirectional laser. Often when the output coupling is low, pulse splitting can be observed in a Kerr-lens mode-locked laser. The satellite pulse separates from the main pulse because its effective group velocity is lower[97]. Eventually, the satellite pulse will meet the main pulse in the Ti:sapphire crystal. The mutual Kerr-lens effect will stabilize the satellite pulse, such that it collides with the main pulse in the Ti:sapphire crystal. This situation is very different

from a bidirectional laser with the pulses colliding in the Kerr medium. We do not expect the system to evolve from a single pulse regime to a bidirectional regime. The bidirectional laser must be initiated in the bidirectional operation. For this reason, we tested the mutual Kerr-lens mode-locking in the linear cavity first.

### 3.8.3 Experimental results

In the linear cavity discussed in Chapter 2, we replace the dye jet with a 3 mm crystal of ZnS. From earlier experiments with Z-scan in optics lab, it was determined that ZnS has the highest nonlinearity with the lowest 2-photon absorption at  $\lambda = 800$  nm. The nonlinear loss is low because the bandgap is at 3.6 eV which is beyond the 2-photon energy of the Ti:sapphire pulses (3 eV). The close proximity of the two-photon energy to the bandgap enhances the effective  $\chi^3$ , although the interaction remains parametric (no energy is transferred to the crystal)[101]. We expect the laser to mode-lock easily, since Radwicz at Oklahoma State University[102] showed that ZnS is an excellent crystal to use for Kerr-lens mode-locking. Because the ZnS is used to mode-lock the laser, the Ti:sapphire crystal is allowed to be tuned independently for maximum power. Also the  $\chi^3$  nonlinearity in ZnS is roughly 50 times the nonlinearity for sapphire, which means the mode-locking threshold will be much lower. After establishing mode-locking, we search for double pulses by scanning the end mirror, which is mounted on a translation stage (see Figure 3.19).

Double pulses were observed over a broad range of end cavity placements (up to 0.5 cm). Although it is easier to achieve double pulses in this experimental setup (in comparison to the dye jet), they were less stable and the pulse train typically had approximately a 10%-20% ripple. With careful alignment and the use of slits to control the spectrum, a very quiet mode of operation is attained. Although the noise was not measured, it appears to be a result of the fluctuations of the  $\text{Ar}^+$  laser. Unfortunately this mode of operation is close to lock-in, so the observed beat note varies from zero (locked) to several kHz (strongly pulled) depending on alignment. Only when the table is violently rocked (creating a frequency difference of several kHz), does a beat note appear for a short period of time. There is a significant amount of blue second-harmonic generated by the ZnS, some of these beams were at odd angles to the ZnS. In particular, a blue beam emanates from the ZnS at normal

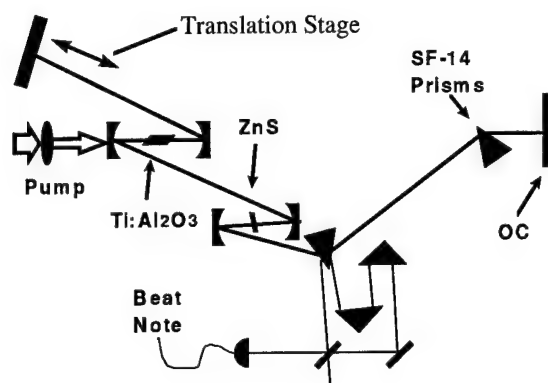


Figure 3.19: Experimental setup for mutual Kerr-lens mode-locking in ZnS. The ZnS crystal is 3 mm long and at Brewster's angle. The cavity fold mirrors all have a radius of curvature of 10 cm.

incidence only when the pulses are colliding in the ZnS. This unexpected blue beam aids in the alignment for bidirectional operation.

The bidirectional ring laser (see Figure 3.20) is more difficult to align and typically

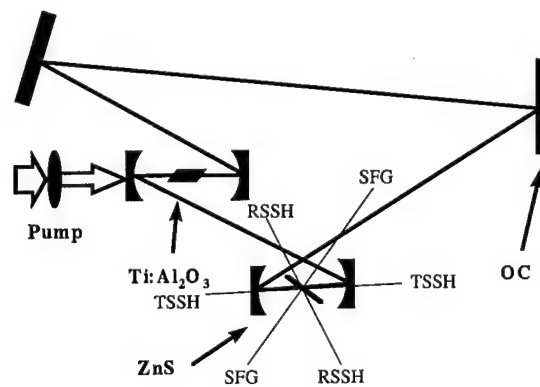


Figure 3.20: Experimental arrangement for mutual Kerr-lens mode-locking. The bidirectional pulses meet in the ZnS crystal.

requires a 'kick' to start the laser in the bidirectional mode, although self-starting operation was also observed. Operation with and without prisms was demonstrated in two different lasers. The laser is aligned by maximizing the blue light normal to the ZnS crystal. When

the laser is not mode-locked the blue beams are barely visible, but when it mode-locks bidirectionally, the blue beams can be seen even with the room lights on. Once the bidirectional operation is achieved, slit A in Figure 3.18 is closed slightly to stabilize the bidirectional pulses.

The beat note is difficult to locate and initially consisted of what sounded like 'white noise.' Further alignment and closing of slit B resulted in a more stable pulse train and a discernible beat note as shown in Figure 3.21. In Figure 3.22 the top plot is the CCW intensity and the bottom is the beat signal. Notice that the beat frequency appears in the CCW intensity. This modulation of the intensity is predicted in the lock-in equation when the beat frequency is close to the lock-in frequency.

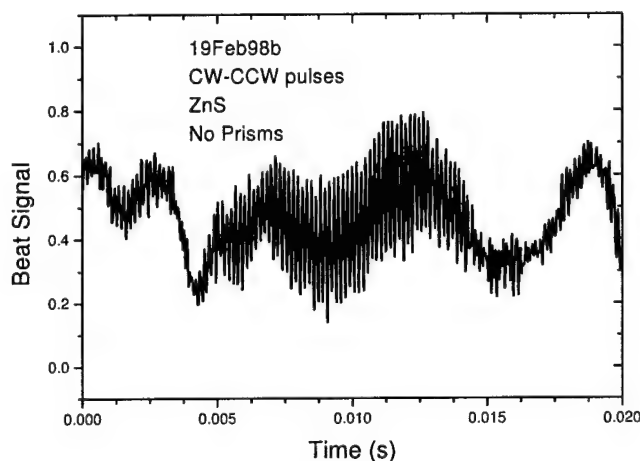


Figure 3.21: Beat signal versus time demonstrates the evolution of the interferogram from locked to a frequency of about 8 kHz.

Figure 3.23 is a plot of the normalized FFT of the beat signal shown in Figure 3.22. Even though the quality of the beat signal looks poor, the FWHM of the beat frequency is only 85 Hz. The second harmonic of the beat signal is easily identified, yielding a geometric ratio,

$$r \equiv \frac{\text{Amplitude of 2nd Harmonic}}{\text{Amplitude of Fundamental}} = 0.032$$

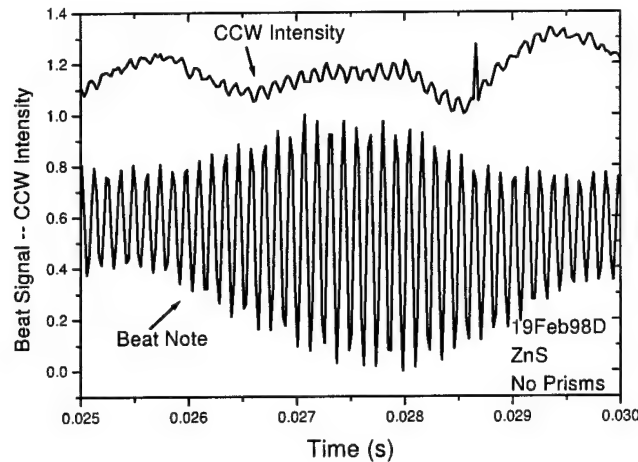


Figure 3.22: CCW signal (top) and beat note (bottom). Notice that the beat frequency appears as an amplitude modulation on the CCW pulse train.

The lock-in frequency is calculated to be:

$$\ell = \frac{2pr}{(1 - r^2)} = 500 \text{ Hz}$$

Recall from Chapter 1 that  $p$  is the pulled frequency. The calculated lock-in frequency appears too low, because the intensity is modulated (see Figure 3.22) at the beat frequency (8 kHz) which normally only occurs near the lock-in frequency. The modulation could be a result of nonlinear dynamics other than lock-in; perhaps a result of the large Kerr nonlinearity in the ZnS. Perhaps another explanation might be the large self-phase modulation, SPM, in the ZnS, which can generate new frequencies at both the upper and lower end of the pulse's spectrum. To check the stability of the pulse crossing point, auto/cross correlations were performed on the laser. The geometry used for the correlations is the same as Figure 3.16. The pulsewidths of the CCW and CW pulses trains are  $18.6$  and  $22.6 \text{ ps} \pm 0.13 \text{ ps}$ , respectively. These are, to the best of our knowledge, the longest Kerr-lens mode-locked pulses ever reported. Based on the autocorrelations, the minimum cross-correlation is  $29 \text{ ps}$ , which is slightly larger than the actual cross-correlation of  $28.1 \text{ ps} \pm 0.1 \text{ ps}$ . Systematic errors on the order of  $0.5 \text{ ps}$  can explain why the cross-correlation is less than the minimum predicted by the autocorrelations. A possible source of these errors is the fact that the laser



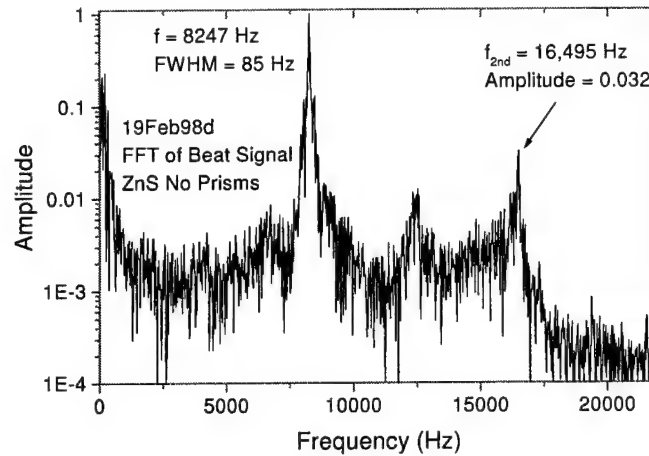


Figure 3.23: Normalized FFT of the beat signal in Figure 3.22. The second harmonic of the beat signal is easily identified and yields a geometric series ratio,  $r = .032$ .

turned off and had to be restarted at least twice while the data was recorded. Because of the strange dynamics, we also recorded the spectra of the CW and CCW pulses, see Figure 3.27. The spectra are a little surprising because the average wavelengths differ by almost 2 nm. Because the beat note detection compares only the same longitudinal modes, the shift in the spectra will not prevent the device from measuring a gyro response. The wavelength offset is, in fact, rather serendipitous because it will allow us to determine the origin of the mysterious blue light. The frequency difference can only be the result of a nonreciprocal optical element in the laser. Since the ZnS is the only new element, the nonreciprocal frequency shift must originate in the ZnS crystal. Perhaps the four-wave mixing (discussed in Chapter 1), which is frequency shifted by the frequency difference is the culprit. If this laser is deemed a viable laser gyro, then the frequency shift will need to be investigated further. The widths of the spectra are:  $2.65$  and  $2.5 \text{ nm} \pm .04 \text{ nm}$  for the CCW and CW pulse trains; however, the resolution of the monochromator was only  $0.4 \text{ nm}$ . The deconvolution of the spectra with the monochromator resolution yields a frequency bandwidth of:  $1.24$  and  $1.17 \text{ THz}$  for the CCW and CW pulses. The time-bandwidth products are:  $23.0$  and  $26.4 \pm .2$  for the CCW and CW pulses, these time-bandwidth products are an amazing 55 times the transform limit for Gaussian pulses. Again a possible explanation is the large amount of SPM in the ZnS

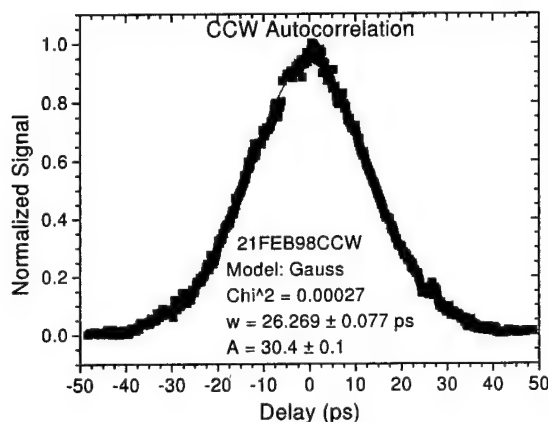


Figure 3.24: Autocorrelation of the CCW pulse train. The pulse width is calculated to be  $18.6 \pm .08$  ps.

which would push the frequency away from line center. We are currently working on an experiment to mount the ZnS on a piezo-electric transducer, in order to randomize the phase of the scattering elements. This motion is perpendicular to the beam, similar to the motion of the dye jet. Theory [29] predicts that randomizing the phase of the scatters is identical to a random, null-bias dither (see Chapter 1).

### 3.8.4 The mysterious blue light

A total of 8 beams of blue light was seen by the naked eye to emanate from the ZnS. ZnS has cubic symmetry, so the index of refraction in the crystalline planes is nearly identical and therefore birefringent phase matching is not possible. We used two crystals for these experiments, the first is a 3 mm polycrystal and the second a 1 mm X-cut single crystal. For the picosecond laser without prisms, the 3 mm crystal works much better because of the greater nonlinearity. Figure 3.28 is a sketch of the geometry of the blue beams. The ZnS crystal is at Brewster's angle inside the Ti:sapphire cavity. The beams labeled RSSH and TSSH correspond to reflected and transmitted surface second-harmonic [103]. Collinear, non-phased matched second-harmonic is beyond the critical angle for total internal reflection and is trapped inside the crystal. The beams labeled SFG are much brighter (about a factor

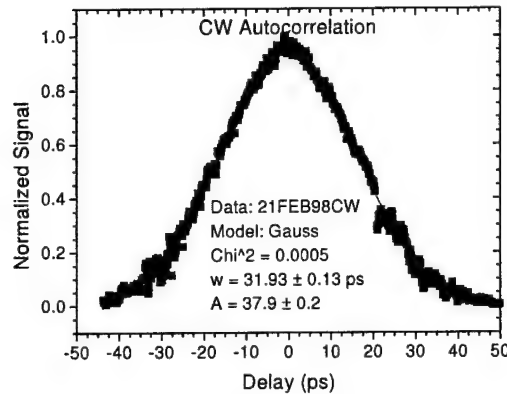


Figure 3.25: Autocorrelation of the CW pulse train. The pulsewidth is calculated to be  $22.6 \pm .13$  ps.

of 100) when lasing bidirectional compared to continuous-wave lasing. The SFG beams completely disappear when the laser is running unidirectional. The SFG beams provide a convenient means to monitor the bidirectionality of the laser. For the 3 mm crystal, there are actually two beams at the SFG that are separated by about  $6.4^\circ$ , the secondary beam is a result of a small wedge in the crystal. To within a few degrees, the SFG signal emanated normal to the surface of the ZnS. The SFG beams are a result of the mixing of the fundamental in one direction with the Brewster's reflection from the other direction. This explanation resolves all of the mysteries associated with the SFG beams: 1) they only appear when bidirectional, 2) they emanate normal to the crystal, 3) the SFG beams from the fs laser were significantly weaker than the picosecond laser (the pulses are not colliding at the surface). Figure 3.29 is a schematic of the beams generating the SFG beams. To confirm that the mechanism is sum frequency generation, we compared the spectra of the surface-second harmonic to the SFG. Figure 3.30 is a plot of the spectra of the SSHG from the CW and CCW beams and the spectrum of the SFG beam. Notice the SFG lies in between the SSHG signals. This plot verifies that the beams are indeed a result of SFG. As a precautionary measure, all possible four-wave mixing geometries were also considered. A total of 12 different possible (not probable) wavevectors were compared for energy and

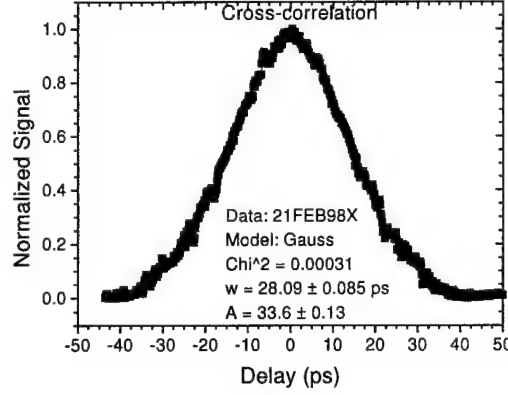


Figure 3.26: Cross-correlation between the CW and CCW pulses. The minimum width predicted from the autocorrelations is 29 ps.

momentum conservation.

$$\vec{k}_4 = \vec{k}_1 + \vec{k}_2 + \vec{k}_3$$

The closest match had a wavevector mismatch of  $|\frac{\Delta k}{k}| \sim 0.2$ , which is a bit too large to be probable.

### 3.9 Conclusions

We demonstrated the first Kerr-lens, optically limited femtosecond ring laser, where the Kerr-lens is used both for Kerr-lens mode-locking and for optical limiting. A simple numerical model correctly predicts the proper location for the Kerr-lens aperture and the aperture for optical limiting. The model also correctly describes the observed beat frequency and the location of the third waist in the cavity. We also report the first beat note from a Q-switched mode-locked laser, which was attained by using a saturable absorbing dye jet in conjunction with a solid-state 2-photon absorber. We also note that the Q-switched operation may be an efficient way to obtain higher peak energies from a Ti:sapphire laser[104].

A novel method, called mutual Kerr-lens mode-locking, is demonstrated for the first time. Mutual Kerr-lens mode-locking defines the crossing point of the counter-propagating

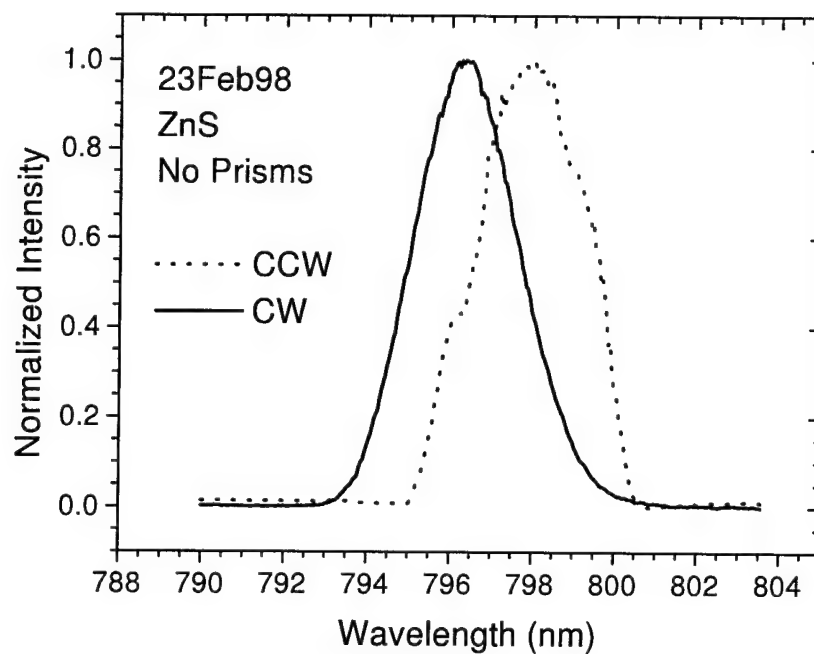


Figure 3.27: Spectra of CW and CCW pulse trains. The FWHMs are 2.5 and  $2.65 \pm .04$  nm for the CW and CCW pulses. The resolution of monochromator is 0.4 nm.

waves in a ring laser gyro without the use of a saturable absorber. We have also discovered that SFG can be used to monitor the bidirectionality of the mutual Kerr-lens mode-locked ring laser.

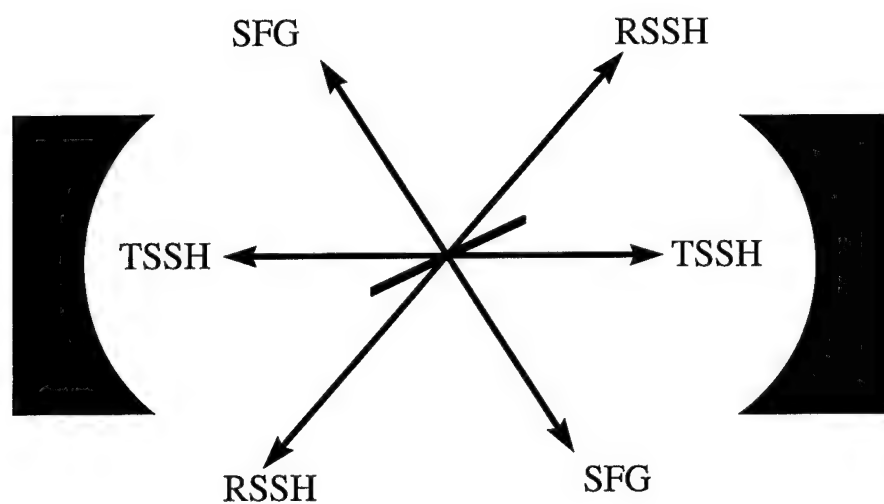


Figure 3.28: Schematic of blue beams emanating from ZnS crystal. The beams are identified as: reflected surface second-harmonic (RSSH), transmitted surface second-harmonic (TSSH) and sum-frequency generation (SFG).

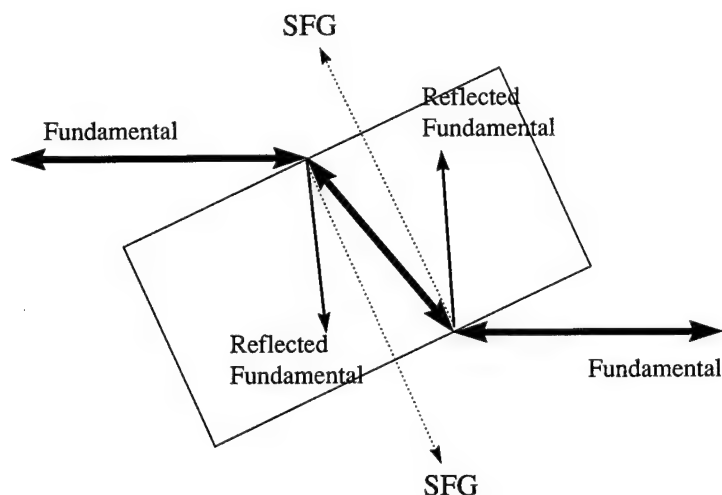


Figure 3.29: Wave vectors involved in SFG (Sum Frequency Generation). The beams are mixed in the intracavity ZnS crystal. The larger beams are the strong, intracavity fundamental beams. The weaker solid beams are the surface reflection of the fundamental. The dotted lines are the SFG beams.

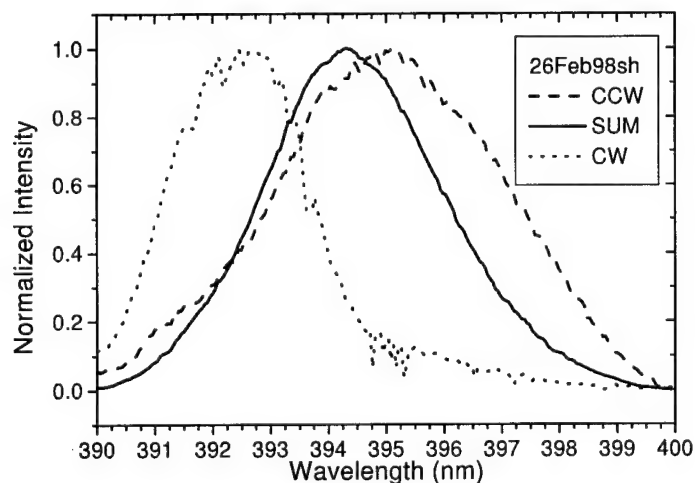


Figure 3.30: Spectra of CW and CCW surface second-harmonic and the spectrum of sum frequency generated normal to the ZnS crystal.

# Chapter 4

## Future Work

The previous chapters highlighted many of the difficulties in developing a solid-state laser gyro. Our efforts in building a pulsed solid-state laser gyro paved the way for modern solutions to some of the problems facing the solid-state laser gyro. The principle problems are interaction of the counter-propagating pulses in the gain medium and removal of the arbitrary bias. The gain problem is solved by an OPO, which has a lifetime equal to the pump pulse duration, and therefore no interaction between pulses. The bias problem is resolved by a novel method of removing the bias using a switchable figure-8 laser. This chapter also contains other experiments that could be explored with a pulsed ring laser gyro. Many would make excellent Master's Degree thesis and others could be (or are being) used for Ph.D. dissertations. Some, like the Ti:sapphire initiator and the Bidirectional OPO Ring Gyro (BORG), have been researched quite extensively and have been submitted for patents. Because the OPO has the potential to exceed the limits of the current HeNe lasers, most of this chapter is devoted to the design of the BORG. The chapter ends with a postmortem of experiments that didn't turn out like we had planned.



## 4.1 OPO

### 4.1.1 Introduction

The seemingly insurmountable problem with bidirectional pulsed ring lasers is gain competition. If the lifetime of the gain medium is greater than the cavity round-trip time, then there will be an interaction between the two pulses. The pulses will be competing for the same gain. Since most solid-state lasers have a long lifetime, it would seem that the phrase, bidirectional solid-state, must be an oxymoron. Only when extreme measures of controlling the pulse energy are put in place (see Chapter 3), can there be any hope of achieving a bidirectional solid-state laser. Does a solid-state system exist that has a lifetime much shorter than the cavity round-trip time? Yes, Optical Parametric Oscillators (OPO) have the unique characteristic of almost no lifetime. The gain in an OPO is present only when the pump pulse is present. Although an OPO is technically not a laser, because the gain is not a result of stimulated emission, but rather a result of frequency down-conversion, it still behaves like a laser. The frequency of the signal and idler pulses in an OPO are determined by the phase matching condition AND by the cavity modes of the OPO. This is similar to a laser where the overall gain bandwidth is defined by the atomic or molecular transitions and the actual lasing frequency is matched to the cavity mode. OPOs have also demonstrated less noise than the Ti:sapphire laser pump[105], squeezed states[106] and simple stabilization schemes[107]. All of these could be beneficial to a sensitive gyroscope.

There are several different ways to implement bidirectional pulses in an OPO. The simplest is to split the pump beam using a 50/50 beam splitter and pump the nonlinear crystal from both directions. One of the pump pulses can be delayed with respect to the other such that the pulses in the OPO meet ONLY in air. This is in sharp contrast to all other methods presented in this dissertation. The methods mentioned earlier all required that the pulses collide in either a saturable absorber or in a Kerr medium. Because there is no gain competition and crossing points only in air, the OPO system will work reliably with no coupling between the CW and CCW modes.

Although any synch-pumped[108] OPO would work, there are some special considerations for short pulse operation. We will concentrate our efforts on a noncritically phase-

matched[105] system because these are easier to align. Possible crystals include KTP[109] and its isomorphs (CTA[110] and RTA[111]),  $\text{LiB}_3\text{O}_5$  [112, 113],  $\text{KNbO}_3$  [114] and more recently PPLN[115, 116].

### 4.1.2 Spatial walk-off

Spatial walk-off occurs when the Poynting vector is not parallel to the  $\mathbf{k}$ -vector[117]. Perhaps a better way to say the same thing is that the energy of the pulse travels in a different direction than the phase front. Or there is a tilted phase front. All of these statements say the same thing. Spatial walk-off reduces the gain in an OPO because the spatial overlap between the three interacting waves becomes smaller as one or more of the pulses moves laterally away from the other pulses. Spatial walk-off is particularly detrimental when the beams are tightly focused. One way to completely avoid spatial walk-off is to use noncritical phase matching. Noncritical phase matching occurs when all of the polarizations line up on principal axes. For example in a negative uniaxial crystal the pump's polarization might be along the fast axis and travel as  $n_e$  while the signal and the idler would be along the optical axis and travel as  $n_o$ . Note that the pump is traveling as  $n_e$  not as  $n_e(\theta)$ , because  $\theta = 90^\circ$  and the wave travels purely as an extraordinary ray. In a biaxial crystal, such as KTP, noncritical phase matching can occur by having the pump and signal's polarization along the  $n_y$  principal axis and the idler along the  $n_z$  principal axis.

### 4.1.3 Temporal walk-off

Temporal walk-off occurs in a short pulse OPO when the group velocities of the pump, signal and idler are different[118]. Because one pulse is traveling faster than the other two, the overlap integral of the pulses will diminish as the pulses propagate through the material. It is possible to delay or advance the resonant signal pulse such that its overlap with the pump will create pulse shortening. The effective length of the crystal is reduced by the temporal walk-off. To calculate the effective length of the interaction, simply calculate how far the pulses travel for the temporal separation to be equal to the pump pulse width. Note that this is an approximation and it tends to calculate an interaction length that is 30% too small.

One explanation is that the pulsewidth of the signal is often square shaped and significantly longer than the pump pulse. A longer signal pulse would lead to a longer interaction length.

$\tau_{pulse} \equiv$  pump pulse width

$v_{g1} \equiv$  group velocity of the pump, signal or idler

$v_{12} \equiv$  inverse group velocity difference between waves 1 and 2

$$v_{12} \equiv \frac{1}{v_{g1}} - \frac{1}{v_{g2}}$$

$$L_{eff} = \frac{\tau_{pulse}}{v_{12}}$$

In the case of noncritically phased matched KTP:

$L_{eff} = .051$  cm between the pump and signal

$L_{eff} = .055$  cm between the pump and idler

$L_{eff} = .035$  cm between the idler and signal

#### 4.1.4 Spectral bandwidth

A short pump pulse will have a wide spectrum. It is important to consider the phase matching bandwidth. A 100 fs Ti:sapphire pulse will have a bandwidth of about 10 nm. Since we are considering noncritical phase matching, spectral bandwidth is not a problem as can be seen in the tuning curve, Figure 4.1.

#### 4.1.5 Tuning

The major disadvantage to noncritical phase matching is that the tuning is difficult and is typically accomplished by tuning the pump wavelength. Figure 4.1 is a plot of the signal wavelength as a function of the pump wavelength for noncritical phase matching.

#### 4.1.6 Alignment

Alignment is easy for a noncritically phase matched OPO because the pump, signal, idler and non-phase matched second harmonic are all collinear. The non-phase matched second harmonic is visible to the naked eye and can be threaded through the OPO cavity. The difficult part is to match the cavity length of the OPO to the cavity length of the pump for synchronous operation. This is accomplished by careful measurement of the cavity lengths

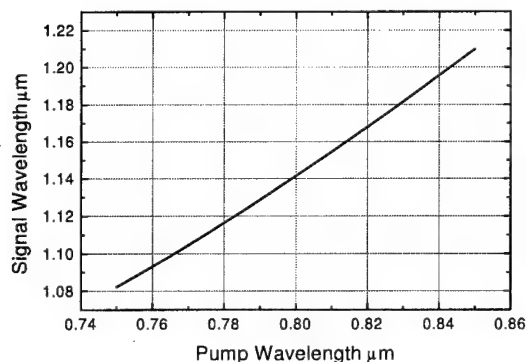


Figure 4.1: Tuning curve of signal wavelength as a function of pump wavelength for noncritical phase matching in KTP

and then translating one of the mirrors to achieve threshold. It is possible to see fringes in the generated blue second-harmonic when the cavity length of the OPO matches the cavity length of the Ti:sapphire laser, although this region is only as long as the pulsewidth.

#### 4.1.7 Double pulse operation

For experiments that are measuring a change in the index of refraction of a medium, such as those discussed in Chapter 2, it is not necessary to have bidirectional operation. In fact there are some advantages to using a double pulsed cavity, see Chapter 2. For the OPO, double pulses are trivial to attain - simply make the OPO cavity twice as long as the pump cavity. This can be implemented in either a ring (see Figure 4.2) or in a linear cavity (see Figure 4.3). One disadvantage to the linear cavity is that the internal loss is twice the loss of the ring because the signal passes through the nonlinear crystal without the pump on the way back. Other pump schemes could be employed which could use a pump pulse to pump a nonlinear sample (see experiments below).

#### 4.1.8 Bidirectional operation

The simplest way to obtain bidirectional operation is to split the pump beam using a 50/50 beamsplitter and pump the nonlinear crystal from both directions (see Figure 4.4). If the

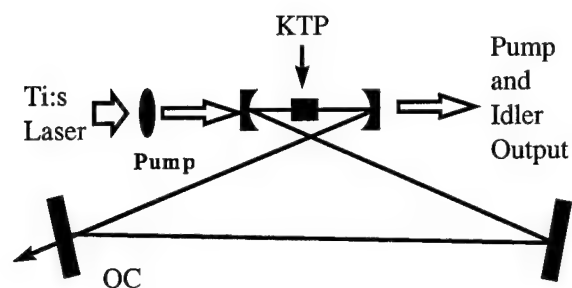


Figure 4.2: The cavity perimeter is 4 times the length of the pump cavity, which produces two OPO pulses in the OPO cavity. The ROC of the curved mirrors is 10 cm concave. The curved mirrors are max-R at the signal wavelength and high-T at the pump and idler wavelength.

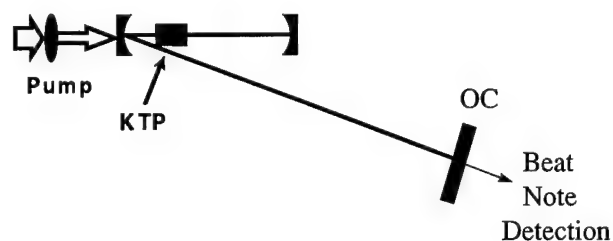


Figure 4.3: The OPO cavity is twice as long as the pump cavity, therefore there will be two pulses in the OPO cavity. ROC of curved mirrors is 10 cm concave. The curved mirrors are max-R for the signal and high-T for the pump and idler.

threshold of the OPO is higher than half the output power of the pump, then a modulator can be employed to use the full pump power in each direction (see Figure 4.5).

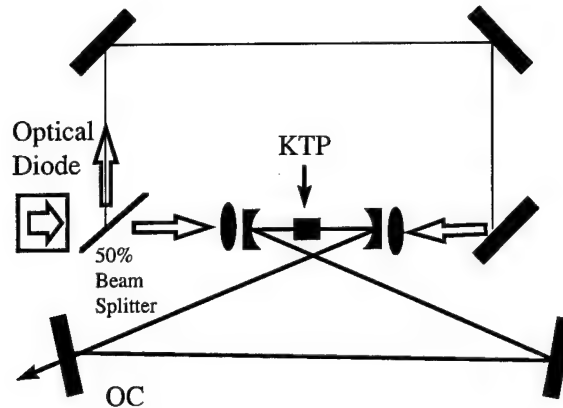


Figure 4.4: A 50/50 beamsplitter divides the pump pulse into two beams. The split off beam is delayed such that the CW and CCW pulses meet only in air. The radius of curvature of the curved mirrors is 10 cm concave. The curved mirrors are max-R at the signal wavelength and high-T at the pump and idler wavelengths.

## 4.2 OPO pump-probe experiments

These are very similar to the experiments with the Ti:sapphire laser, with two exceptions. The ring gyro is now an OPO and the pump is the direct output of the Ti:sapphire laser. Using the amplitude modulator, we can select every other Ti:sapphire pulse to pump the OPO and then the sample. This has the huge advantage of being able to use all of the pump pulse instead of having to frequency double the output. Also the Ti:sapphire laser has less amplitude noise and two orders of magnitude more peak power available to pump experiments. Basically all experiments mentioned in this chapter that deal with a pump-probe laser gyro could be accomplished using an OPO with 100 times the peak power. The schematic for this general class of experiments is shown in Figure 4.6.

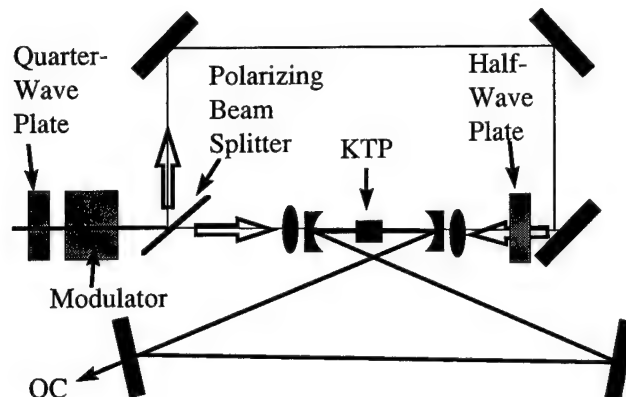


Figure 4.5: Similar to the double ring cavity in Figure 4.2. The second pulse is split off and pumps the KTP crystal from the opposite direction. The advantage is that the full pump pulse is used in each direction. The disadvantage is that the cavity perimeter must be 4 times the cavity length of the pump.

### 4.3 Stopping the earth

The second problem with pulsed ring laser gyros is the arbitrary bias beat note. This bias beat note can vary and result in an unreliable measuring device. What is needed is a way to calibrate the gyro periodically to check if the beat note is a result of nonlinearities in the cavity or if it is a result of a rotation. Of course one way to do this is to periodically stop all rotations - including the earth, and measure the bias beat note. Although it is impossible to stop the rotations, it is possible to not measure the rotations. This is done by a clever switching between a figure-8 laser geometry which doesn't measure rotations and an oval laser geometry which does measure rotations. The difference in beat frequency between the two is a result of pure rotation. Since this method can be employed in any pulsed system, only a schematic of the layout is drawn in Figure 4.7.

### 4.4 Bragg reflector vibrations

Laser induced acoustics is a large field of study[119, 120]. In the typical experiment a bicell is used to detect the angular deflection caused by a physical deformation of the surface[121].

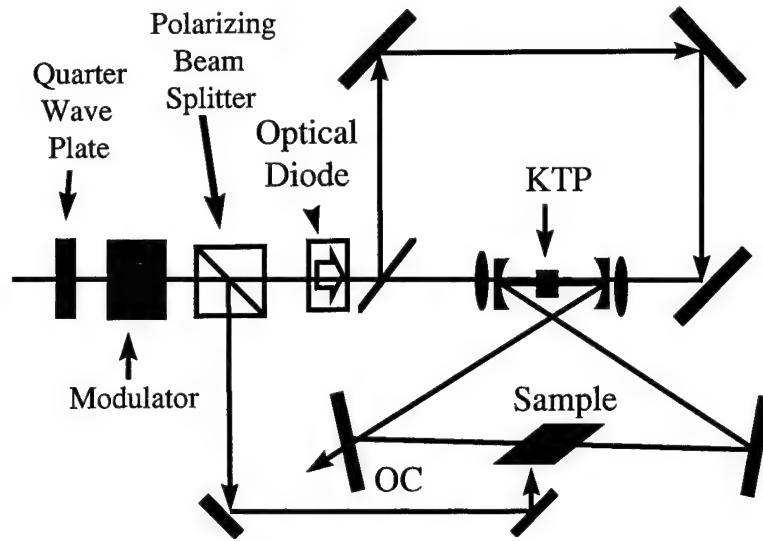


Figure 4.6: Bidirectional ring with modulated pump pulse. Every other pump pulse is selected to pump sample. The OPO pump is split by a 50/50 beam splitter.

The deformation is generated by an acoustic wave that is launched in the material by a laser. The bump can be as large as 10-20 pm[122]. This amount of deflection should be barely detectable using the Ti:sapphire laser. One of the end mirrors in the Ti:sapphire laser is replaced with a AlAs/AlGaAs multilayer stack (or Bragg mirror). The output of the laser is frequency doubled and modulated as discussed earlier. Every other blue pulse excites an acoustic wave in the Bragg mirror[123]. See Figure 4.8 below. The deflection is then detected by the intracavity pulse. The bandgap of the semiconductor material is slightly higher in energy than the intracavity pulse, so linear absorption of the intracavity pulse is minimal while the absorption of the second-harmonic pulse is very strong.

## 4.5 Differential optical path meter

This experiment also uses the phase difference between two pulses inside a laser gyro to measure a change in the difference in optical path length. Instead of measuring the longitudinal change in optical path, this experiment measures the spatial change in optical thickness of a sample. The application is similar to the Twyman-Green interferometer and the Fizeau in-



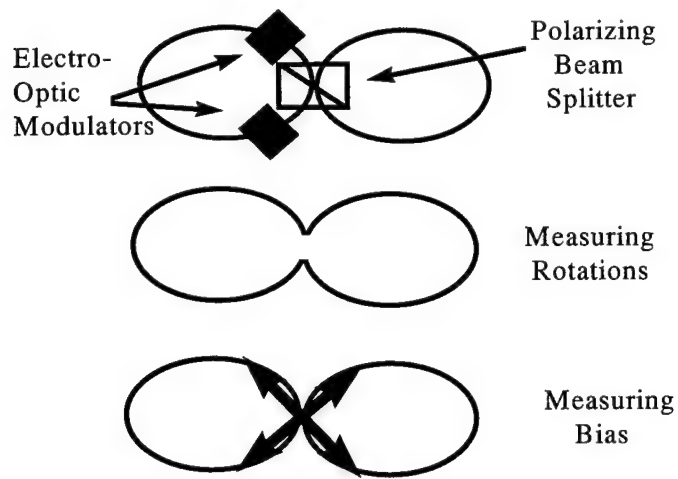


Figure 4.7: The top schematic shows the layout of the modulators and polarizing beam splitter. The middle schematic shows the optical path when the device is measuring a rotation. The bottom schematic shows the optical figure-8 path when the device is measuring the bias beat note.

terferometer used for testing optical elements and the thickness of films; except this method is capable of detecting surface changes on the order of  $\lambda/800,000$ ! The experiment is easy to set up - simply replace one of the prisms with a material that can be used for an electro-optic modulator. By applying a voltage at a frequency of  $c/2L$ , every other pulse will be deflected at the sample (see Figure 4.9). Every other pulse measures a differential change in optical path length. The sample is then scanned in the x-y plane to yield a 2-d image of the optical thickness of the sample.

## 4.6 Metal detector

The same laser gyro can also be configured to be a metal detector. This scheme is similar to an FM mode-locker. A phase modulator is placed in the cavity that shifts every other pulse a full  $\pi$ . Any phase difference other than exactly  $\pi$ , will be measured as a beat note. A tank circuit is commonly used to achieve such large phase changes. The tank circuit consists of a coil of wire and the nonlinear crystal (see Figure 4.10). Any ferrous material

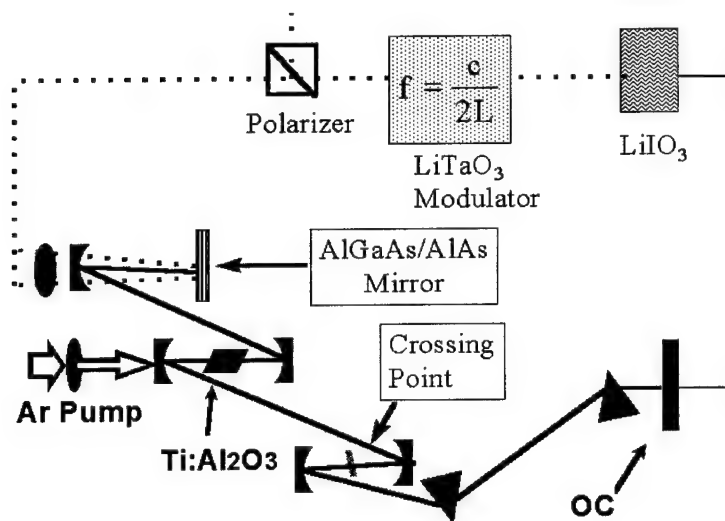


Figure 4.8: End mirror of typical Ti:sapphire cavity is replaced with a concave mirror which focuses the beam onto the semiconductor end mirror. The beams must be focused to achieve the maximum modulation. The  $\text{LiIO}_3$  crystal generates the second-harmonic. The  $\text{LiTaO}_3$  is an electro-optic modulator.

that enters the field pattern emitted by the coil, will change the  $Q$  of the tank circuit. It will also shift the resonance of the circuit, which can result in an even larger change in voltage applied to the nonlinear crystal. The change in voltage applied to the nonlinear crystal will result a change in the beat note. The static phase difference was chosen to be  $\pi$ , but in principle any multiple of  $\pi$  will also work; every multiple of  $\pi$  multiplies the sensitivity of the device. Another method is called the emitter-detector method. In this scheme an RF wave is propagated into the ground and the reflected RF energy is detected.

## 4.7 Decoupling of mutual Kerr-lens mode-locking

The schematic of mutual Kerr-lens mode-locking was discussed in Chapter 3. This method produces mode-locked pulses, but the pulses are coupled to one another by scattering in the  $\text{ZnS}$ . If the Kerr medium is put in constant motion, then the phase of the scattered light will be randomized and prevent lock-in, as was discussed in Chapter 1. Two piezos can be

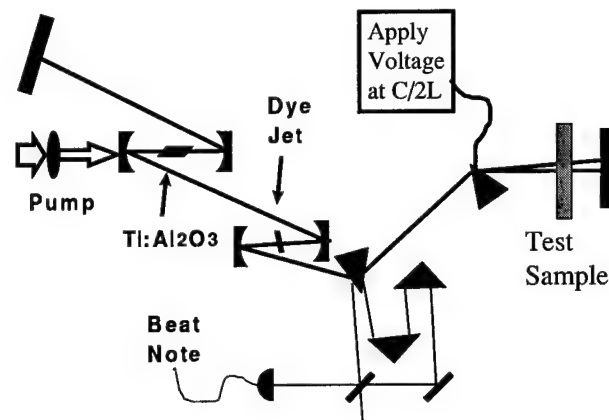


Figure 4.9: Schematic for testing optical elements. Every other pulse is deflected at the sample, yielding a differential measurement of its thickness.

connected such that a sine wave applied to one and a cosine wave to the other will produce circular motion, similar to a Lissajous pattern. This experiment is important not only for the possible applications, but also because it could answer the fundamental question of why the femtosecond ring dye laser does not lock.

## 4.8 Saturable Bragg reflector

Similar to the Schott glass idea discussed in Chapter 2, this method of mode-locking is reported to produce 20 fs pulses. For this reason, it would be interesting to build a ring laser gyro using a saturable Bragg reflector, or one of the other semiconductor mode-lockers developed by Professor Ursula Keller[61, 62, 72]. These devices will probably lock the CW and CCW pulses and therefore also require some method to unlock the two pulses like randomizing the phase of the scattered light.

## 4.9 Ti:sapphire initiator

Mode-locked lasers are a very important tool for a variety of applications; however, most suffer from a self-starting problem. The Kerr-lens mode-locking employed by the laser

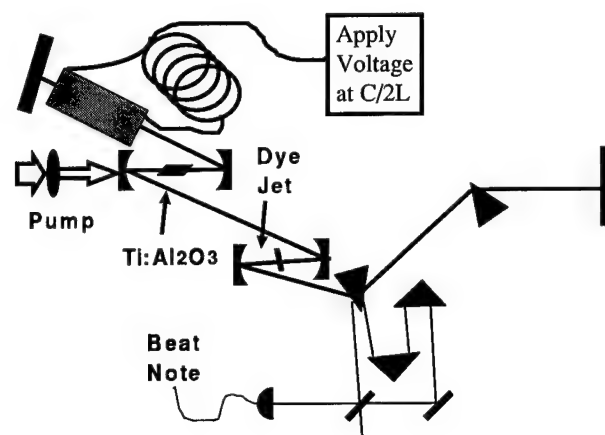


Figure 4.10: Schematic of a laser gyro metal detector. Any ferrous material that enters the field emitted by the coil will be detected as a change in beat note.

requires a kick or a noise spike for the mode-locking to start. There are many methods to initiate mode-locking, but they all have disadvantages. Most require an extra element to be added to the cavity, or a physical knocker added to one of the mirrors. By sending an acoustic wave through the Ti:sapphire crystal at the repetition rate of the laser, the intensity of the light in the laser will be modulated and result in initiating Kerr-lens mode-locking. The method of using an acoustic optic modulator for mode-locking is not new and is called regenerative feedback. Because the acoustic modulator would be the gain medium, there are no additional parts required.

## 4.10 Mapping the stability region of a Kerr-lens mode-locked ring laser

Many excellent papers have been written on the stability curves for the linear Kerr-lens mode-locked Ti:sapphire laser. The linear cavity is easy to analyze because the curvature of the Gaussian beam must match the curvature of the end mirrors. There is no such requirement in the ring cavity. This is an extremely difficult system to model because there is an extra degree of freedom in the system, which of course implies an extra dimension in

the parameter space to explore. The linear cavity was solved with only 2 degrees of freedom by simply stepping through all possible values. A similar method for the ring laser would be very time consuming. A combination of mapping the global parameter space coupled with a routine to find minimums will yield an accurate mapping of the stability region for the Kerr-lens mode-locked Ti:sapphire laser.

## 4.11 Postmortem examination of failed experiments

Most experimental results are typically preceded by numerous failures. Just because an experiment does not produce reproducible data does not mean that it is a failure, often valuable lessons can be learned.

### 4.11.1 Cross phase modulation in Ti:sapphire

The enhanced Kerr-effect due to colliding pulses was discussed in Chapter 3. Instead of colliding pulses, this experiment uses orthogonally polarized, collinear pulses. This experiment involves taking the output of the Ti:sapphire laser, putting it through a quarter-wave plate, an electro-optic modulator and finally a polarizing beamsplitter (see Figure 4.11). The

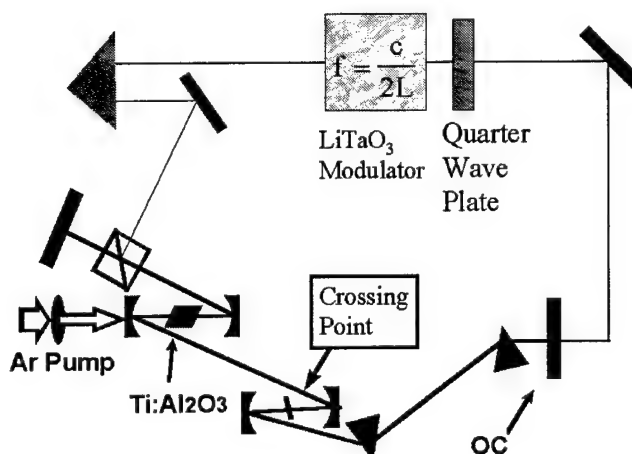


Figure 4.11: The polarizing beam splitter separates the s and p polarizations. The s polarization is injected back into the cavity. The modulator selects every other pulse to be injected back into the cavity by switching the pulses between s and p polarization.

s-polarization output from the beamsplitter is injected into the Ti:sapphire crystal. The experiment can also be accomplished using a ring cavity and a half-wave plate. The delay of this injected pulse can be varied while monitoring the beat note of the laser. The injected pulse should not couple to the cavity because its polarization is at  $90^\circ$  to the light that is resonating. The injected pulse will create a moving index in the sapphire. The intracavity pulse will 'surf' on this index wave and result in a phase shift.

This experiment was attempted using a polarizing beam splitter and a half-wave plate in a ring cavity. The injected pulse invariably locked the laser. The half-wave plate was of pretty good quality (manufacturer was Casix), so we do not believe that it was the source of the problem. The polarizing beam splitter was an air-gap calcite borrowed from a Nd:YAG laser. We believe the polarizer did not have a high enough of a rejection ratio and thus a small amount of the horizontal polarization is coupled back into the laser.

#### 4.11.2 Phase multiplier

Many organic optical materials have a yellow tinge[124]. This means that the material is absorbing light in the blue part of the spectrum. The frequency doubled output of a Ti:sapphire laser at 400 nm would be an ideal pump of these materials. The experimental setup is shown below in Figure 4.12. The output of the Ti:sapphire is frequency doubled and amplitude modulated as described above. Every other pulse strikes the organic sample at the same time that an intracavity pulse is in the dove prism. The excitation of the organic material will change its refractive index. The change in refractive index at the location where the intracavity pulse is totally internally reflected will result in a large phase change. This phase change will then be detected by the beat frequency.

This experiment was attempted with a ring cavity. There are several problems plaguing this experiment. First it requires the generation of the second-harmonic with high efficiencies. Because of the problems associated with short-pulse ring lasers mentioned in Chapters 2 and 3, we were not able to generate more than a few milliwatts of second-harmonic because the pulses in the stable geometry are typically in the picosecond region. The second problem was that the organic samples were optically thin, having only a few percent absorption. Several samples were attempted including Iodine dyes, Coumarin 500

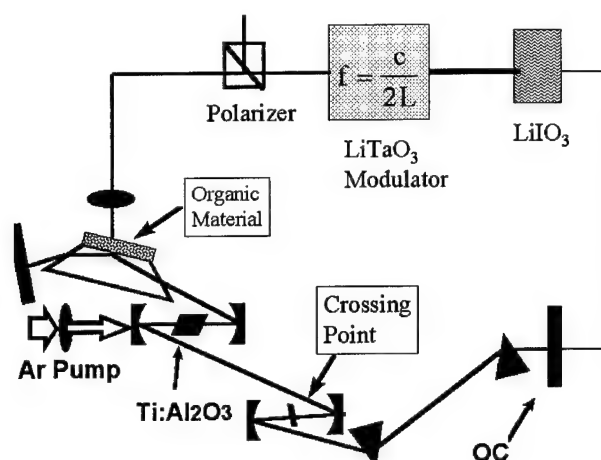


Figure 4.12: The intracavity beam is incident on the dove prism such that it is always totally internally reflected. The modulator selects every other pulse out of the Ti:sapphire laser. The  $\text{LiIO}_3$  crystal generates the second-harmonic. The  $\text{LiTaO}_3$  crystal is an electro-optic modulator.

and  $\text{Re}(\text{CO})_3(\text{bpy})\text{Br}$  from New Mexico Highlands University.

### 4.11.3 Pump/probe experiments with Schott glass

These experiments were very similar to the organic experiments discussed above. Again this experiment required the generation of copious amounts of blue second-harmonic, which we were not able to produce because of the long pulsewidths. Another problem with this experiment is the thermal instabilities associated with the glass, which was reported in Chapter 2. The success of the experiment required that the glass be placed at a tightly focused beam waist in the cavity. Since glass is a poor conductor of heat, the smallest amount of absorption at the fundamental results in instabilities in the laser output.

## 4.12 Conclusions

This dissertation studied the Ti:sapphire laser as a pulsed ring laser gyroscope. Numerous new discoveries were made, which will be listed in the order that they appeared in this dissertation. A novel linear cavity with two pulses in the cavity was used for the first time

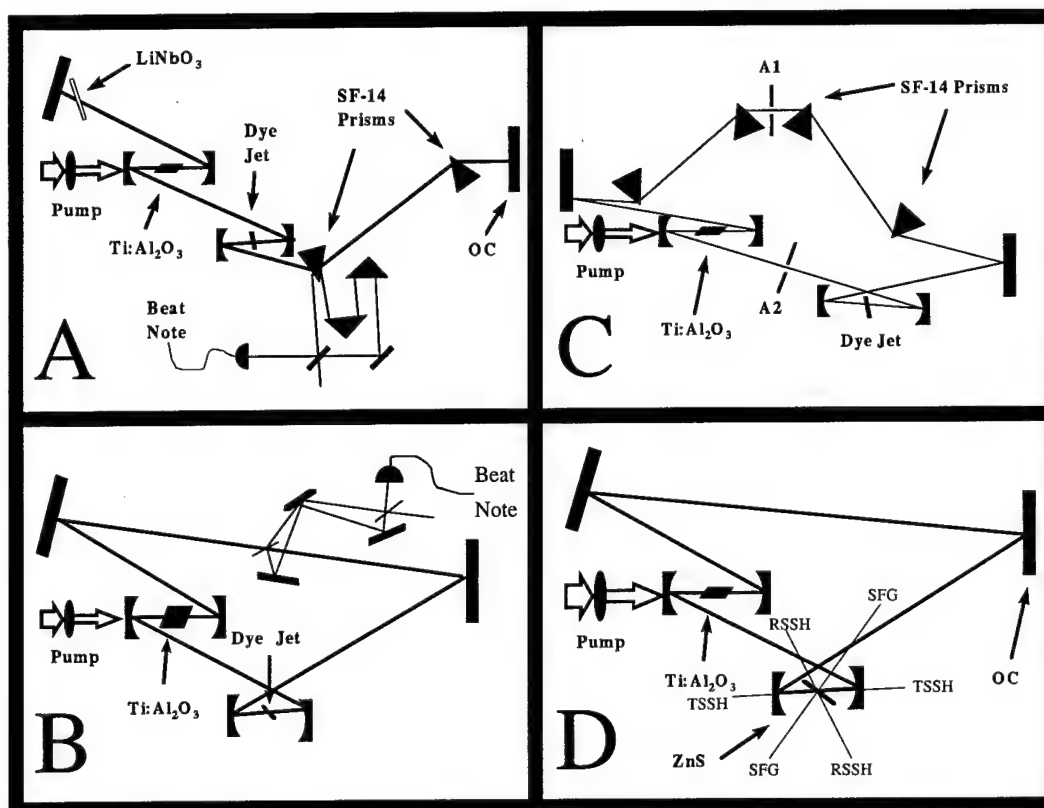


Figure 4.13: A) Linear cavity: no bias beat frequency. B) Saturable absorber mode-locked ring gyro: measured low beat frequencies. C) Kerr-lens mode-locked ring gyro: femtosecond pulses. D) Mutual Kerr-lens mode-locked: all solid-state.



to measure electro-optic coefficients (see Figure 4.13A). This laser can be analyzed in the same manner as a ring laser, with the difference being that the pulses are indistinguishable whereas in the ring the CW and CCW pulses are easily separable. Next a solid-state ring laser gyroscope using a dye-jet saturable absorber was studied (see Figure 4.13B). This laser produced the lowest beat frequencies recorded in a pulsed laser (10 Hz with a 10 Hz bandwidth) and also the narrowest beat note bandwidth at 0.85 Hz. Null-bias dithering was demonstrated for the first time using an electro-optic modulator. A new method of extracting the average beat frequency from a dithered laser was discovered and the experimental result was verified with an analytic solution. In Chapter 3, Kerr-lens mode-locking was used for the first time in a ring laser gyro (see Figure 4.13C). This laser employed both passive negative and positive feedback in the same Kerr element. A novel method of stabilizing the crossing point in ring laser was demonstrated by using mutual Kerr-lens mode-locking (see Figure 4.13D). Finally the design of a Bidirectional OPO Ring Gyro (BORG) was discussed in Chapter 4. The BORG has the potential to exceed the quantum limit of HeNe laser gyros because it solves the problem of gain competition. Also presented is a novel method of removing the bias in a laser gyro. These designs forecast an exciting future for research in pulsed laser gyroscopes.

# Bibliography

- [1] M. Sheik-Bahae and M. Ebrahimzadeh. Measurements of nonlinear refraction in the second-order  $\chi(2)$  materials  $\text{KTiOPO}_4$ ,  $\text{KNbO}_3$ ,  $\beta\text{-BaB}_2\text{O}_4$ , and  $\text{LiB}_3\text{O}_5$ . *Optics Communications*, 142:294–298, October 1997.
- [2] E.W. Van Stryland and M. Sheik-Bahae. Z-scan measurements of optical nonlinearities. In *CRC Handbook of Nonlinear Optics*. CRC Press, Boca Raton, 1998.
- [3] G. E. Stedman. Ring-laser tests of fundamental physics and geophysics. *Rep. Prog. Phys.*, 60:615–688, 1997.
- [4] A. D. Kersey, A. Dandridge, and W. K. Burns. Fiber optic gyroscope technology. *Optics News*, (11):12–19, November 1989.
- [5] V. Rautenberg, H.-P. Plag, M. Burns, G. E. Stedman, and H.-U. Juttner. Tidally induced Sagnac signal in a ring laser. *Geophys. Res. Lett.*, 24:893–896, 1997.
- [6] G. E. Stedman, H. R. Bilger, Z. Li, M. P. Poulton, C. H. Rowe, I. Vetharaniam, and P. V. Wells. Canterbury ring laser and tests for nonreciprocal phenomena. *Aust. J. Phys.*, 46:87–101, 1993.
- [7] H. R. Bilger, G. E. Stedman, U. Schreiber, and M. Schneider. Ring laser for geodesy. *IEEE Transactions on Instrumentation and Measurement*, 44(2):468–470, April 1995.
- [8] Scott Diddams. *Phase Measurements inside Mode-locked ring lasers*. PhD thesis, University of New Mexico, December 1996.
- [9] N. Buholz and M. Chodorow. Acoustic wave amplitude modulation of a multimode ring laser. *IEEE J. of Quantum Electronics*, 3(11):454–459, November 1967.

- [10] A. V. Dotsenko and E.G.Lariontsev. Conditions for cw stimulated emission from a solid-state ring laser with a nonlinear absorber. *Sov. J. Quantum Electron.*, 9(5):576–579, May 1979.
- [11] E. L. Klochan, L. S. Kornienko, N. V. Kravtsov, E. G. Lariontsev, and A. N. Shelaev. Oscillation regimes in a rotating solid-state ring laser. *Sov. Phys.-JETP*, 38(4):669–674, April 1974.
- [12] D. Gnass, N. P. Ernsting, and F. P. Schäfer. Sagnac effect in the colliding-pulse-mode-locked dye ring laser. *Appl. Phys. B*, 53:119–120, 1991.
- [13] M. L. Dennis, J.-C. Diels, and M. Lai. The femtosecond ring dye laser: a potential new laser gyro. *Optics Letters*, 17:529 – 531, 1991.
- [14] W. R. Christian and M. J. Rosker. Picosecond pulsed diode ring-laser gyroscope. *Optics Letters*, 16(20):1587–1589, October 1991.
- [15] F. Aronowitz. *Laser Applications*. Academic, New York, 1971.
- [16] W. F. Parks and J. T. Dowell. Fresnel drag in uniformly moving media. *Physical Review A*, 9(1):565–567, January 1974.
- [17] R. T. De Carvalho and J. Blake. Slow-flow measurements and fluid dynamics analysis using the Fresnel drag effect. *Applied Optics*, 33(25):6073–6077, 1 September 1994.
- [18] G. A. Sanders and S. Ezekiel. Measurement of Fresnel drag in moving media using a ring-resonator technique. *J. Opt. Soc. Am. B.*, 5(3):674–678, March 1988.
- [19] M. Vallet, N. H. Tran, P. Tanguy, A. L. Floch, and F. Bretenaker. Ring-laser gyro with spatially resolved eigenstates. *Optics Letters*, 19(16):1219–1221, August 15 1994.
- [20] M. Vallet, F. Bretenaker, N. H. Tran, P. Tanguy, and A. L. Floch. Spatially resolved eigenstates for traveling and standing waves in ring lasers. *J. Opt. Soc. Am. B.*, 12(1):146–154, January 1995.
- [21] M. L. Dennis and J.-C. Diels. Analysis of a ring-laser gyroscope with intracavity phase-conjugate coupling. *Applied Optics*, 33(4):1659–1672, 20 March 1994.

- [22] G. E. Stedman, Z. Li, C. H. Rowe, A. D. McGregor, and H. R. Bilger. Harmonic analysis in a large ring laser with backscatter-induced pulling. *Physical Review A*, 51(6):4944–4958, June 1995.
- [23] F. Aronowitz and R. J. Collins. *Appl. Phys. Lett.*, 9:55, 1966.
- [24] J. R. Wilkinson. Ring lasers. *Prog. Quant. Elect.*, 11:1–103, 1987.
- [25] J. Killpatrick. The laser gyro. *IEEE Spectrum*, 4:44, October 1967.
- [26] A. Bambini and S. Stenholm. Analysis of nonlinear response in a body dithered ring laser gyro. *Optics Communications*, 49(4):269–274, 15 March 1984.
- [27] A. Bambini and S. Stenholm. Theory of a dithered-ring-laser gyroscope: A Floquet-theory treatment. *Physical Review A*, 31(1):329–337, January 1985.
- [28] A. Bambini and S. Stenholm. Theory of a dithered-ring-laser gyroscope. II Cayley transformations and square-wave dithering. *Physical Review A*, 31(6):3741–3749, June 1985.
- [29] A. Bambini and S. Stenholm. Random dither modulation of a ring-laser gyroscope. *J. Opt. Soc. Am. B.*, 4(2):148–163, February 1987.
- [30] W. T. Coffey, Y. P. Kalymkov, and E. S. Massawe. Effective-eigenvalue approach to the nonlinear Langevin equation for the Brownian motion in a tilted periodic potential. II. Application to the ring-laser gyroscope. *Physical Review E*, 48(2):699–704, August 1993.
- [31] W. Schleich and P. Dobiasch. Noise analysis of ring-laser gyroscope with arbitrary dither. *Optics Communications*, 52(1):66–69, 1 November 19.
- [32] D. A. Andrews and T. A. King. Sources of error and noise in a magnetic mirror gyro. *IEEE J. Quantum Electronics*, 32(3):543–548, March 1996.
- [33] G. E. Stedman, M. T. Johnsson, Z. Li, C. H. Rowe, and H. R. Bilger. T violation and microhertz resolution in a ring laser. *Optics Letters*, 20(3):324–326, February 1 1995.

- [34] H. R. Bilger, G. E. Stedman, M. P. Poulton, C. H. Rowe, Z. Li, and P. V. Wells. Ring laser for precision measurement of nonreciprocal phenomena. *IEEE Transactions on Instrumentation and Measurement*, 42(2):407–411, April 1993.
- [35] J. Chesnoy. Picosecond gyrolaser. *Optics Letters*, 14(18):990–992, September 15 1989.
- [36] J.-C. Diels and I. C. McMichael. Degenerate four-wave mixing of femtosecond pulses in an absorbing dye jet. *J. Opt. Soc. Am. B*, 3(4):535–543, April 1986.
- [37] R. W. Boyd. *Nonlinear Optics*. Academic Press, Boston, MA, 1992.
- [38] M. Aoyama and K. Yamakawa. Noise characterization of and all-solid-state mirror-dispersion-controlled 10-fs Ti:sapphire laser. *Optics Communications*, 140(25):255–258, 1 August 1997.
- [39] J. Son, J. V. Rudd, and J. F. Whitaker. Noise characterization of a self-mode-locked Ti:sapphire laser. *Optics Letters*, 17(10):733–735, May 15 1992.
- [40] D. E. Spence, J. M. Dudley, K. Lamb, W. E. Sleat, and W. Sibbett. Nearly quantum-limited timing jitter in a self-mode-locked Ti:sapphire laser. *Optics Letters*, 19(7):481–483, April 1 1994.
- [41] C. W. Siders, E. W. Gaul, M. C. Downer, A. Babine, and A. Stepanov. Self-starting femtosecond pulse generation from a Ti:sapphire laser synchronously pumped by a pointing-stabilized mode-locked Nd:YAG laser. *Rev. Sci. Instrum.*, 65(10):3140–3144, October 1994.
- [42] M. J. Bohn and J. G. McInerney. Bistable output of an optically pumped vertical-cavity surface-emitting laser. *J. Opt. Soc. Am. B*, 14(12):3430–3436, December 1997.
- [43] R. Kiyon, S. K. Kim, and B. Y. Kim. Bidirectional single-mode Er-doped fiber-ring laser. *IEEE Photonics and Technology Letters*, 8(12):1624–1626, December 1996.
- [44] I. P. Christov, H. C. Kapteyn, and M. M. Murnane. Comment on sub-10-fs mirror-dispersion-controlled Ti:sapphire laser and ultrabroadband ring oscillator for sub-10-fs pulse generation. *Optics Letters*, 22(24):1882–1883, December 15 1997.

- [45] Ch. Spielman, T. Brabec, and F. Krausz. Reply to comment on sub-10-fs mirror-dispersion-controlled Ti:sapphire laser and ultrabroadband ring oscillator for sub-10-fs pulse generation. *Optics Letters*, 22(24):1882–1883, December 15 1997.
- [46] A. C. Scott, F. Y. R. Chu, and D. W. McLaughlin. The soliton: A new concept in applied science. In *Proceedings of the IEEE*, volume 61, pages 1443–1483, October 1973.
- [47] L. F. Mollenauer, R. H. Stolen, and J. P. Gordon. Experimental observation of picosecond pulse narrowing and solitons in optical fibers. *Phys. Rev. Lett.*, 45:1095, 1980.
- [48] S. R. Friberg and W. Jiang. Ultrafast switching using two-color soliton collisions. *International Topical Meeting on Photonic Switching*.
- [49] M. N. Islam. *Ultrafast Fiber Switching Devices and Systems*. Cambridge University Press, New York, 1992.
- [50] W. Dietel, J. J. Fontaine, and J.-C. Diels. Intracavity pulse compression with glass: a new method of generating pulses shorter than 60 femtoseconds. *Optics Lett.*, 8:4–6, 1983.
- [51] J.-C. Diels, W. Dietel, J. J. Fontaine, W. Rudolph, and B. Wilhemi. Analysis of a mode-locked ring laser: chirped-solitary-pulse solutions. *J. Opt. Soc. Am. B.*, 2:680, 1985.
- [52] A. Sanchez, R. E. Fahey, A. J. Strauss, and R. L. Agrawal. Room-temperature cw operation of the Ti:Al<sub>2</sub>O<sub>3</sub> laser. In *Tunable Solid-State Lasers II*. Springer-Verlag, New York, 1986.
- [53] R. L. Fork, O. E. Martinez, and J. P. Gordon. Negative dispersion using pairs of prisms. *Optics Letters*, 9:150–152, 1984.
- [54] J. D. Kafka, M. L. Watts, and J.-W. J. Pieterse. Picosecond and femtosecond pulse generation in a regeneratively mode-locked Ti:sapphire laser. *IEEE J. Quantum Electron.*, 28(10):2151–2161, October 1992.

- [55] H. A. Haus, J. G. Fujimoto, and E. P. Ippen. Analytic theory of additive pulse and Kerr lens mode-locking. *IEEE J. Quantum Electron*, 28(10):2086–2096, October 1992.
- [56] N. Sarakura and Y. Ishida. Ultrashort pulse generation from a passively mode-locked Ti:sapphire laser based system. *IEEE J. Quantum Electron*, 28(10):2134–2141, October 1992.
- [57] F. Krausz, M. E. Fermann, T. Brabec, P. F. Curley, M. Hofer, M. H. Ober, C. Spielmann, E. Wintner, and A. J. Schmidt. Femtosecond solid-state lasers. *IEEE J. Quantum Electron*, 28:2097–2121, October 1992.
- [58] P. F. Curley, Ch. Spielmann, T. Brabec, F. Krausz, E. Wintner, and A. J. Schmidt. Operation of a fs Ti:sapphire solitary laser in the vicinity of zero group-delay dispersion. *Opt. Lett.*, 18:54–57, 1993.
- [59] N. Sarakura and Y. Ishida. Pulse evolution dynamics of a femtosecond passively mode-locked Ti:sapphire laser. *Optics Letters*, 17(1):61–63, 1 January 1992.
- [60] J. Zhou, G. Taft, C. Huang, M. M. Murnane, H. C. Kapteyn, and I. P. Christov. Pulse evolution in a broad-bandwidth Ti:sapphire laser. *Optics Letters*, 19(15):1149–1151, 1 August 1994.
- [61] F. X. Kartner and U. Keller. Stabilization of soliton-like pulses with a slow saturable absorber. *Optics Letters*, 20(1):16–18, 1 January 1995.
- [62] F. X. Kartner, K. Kopf, and U. Keller. Solitary-pulse stabilization and shortening in actively mode-locked lasers. *J. Opt. Soc. Am. B*, 12(3):486–496, March 1995.
- [63] P. F. Curley, Ch. Spielmann, T. Brabec, and F. Krausz. Ultrabroadband femtosecond laser. *IEEE J. Quantum Electron*, 30(4):1100–1114, April 1994.
- [64] P. M. Goorjian, A. Taflove, R. M. Joseph, and S. C. Hagness. Computational modeling of femtosecond optical solitons from Maxwell's equations. *IEEE J. Quantum Electronics*, 28(10):2416–2422, October 1992.

- [65] B. E. A. Saleh and M. C. Teich. *Fundamentals of Photonics*. John Wiley and Sons, New York, 1991.
- [66] M. A. Arbore, M. M. Fejer, M. H. Chou, A. Galvanauskas, and D. Harter. Compression of ultrashort pulses using second harmonic generation in aperiodically poled lithium niobate. In *CLEO 97 Postdeadline Papers*, Washington, D.C., 1997. Optical Society of America.
- [67] Siegman. *Lasers*. University Science Books, Mill Valley, CA., 1986.
- [68] V. E. Zakharov and A. B. Shabat. Exact theory of two-dimensional self-focusing and one-dimensional self-modulation of waves in nonlinear media. *Sov. Phys. JETP*, 34:62–69, 1972.
- [69] A. Stingl, Ch. Spielmann, F. Krausz, and R. Szipocs. Sub-10 fs mirror-dispersion-controlled Ti:sapphire laser. *Optics Letters*, 20:602, 1995.
- [70] L. Xu, Ch. Spielmann, F. Krausz, and R. Szipocs. Ultrabroadband ring oscillator for sub-10-fs pulse generation. *Optics Letters*, 21(16):1259, August 15 1996.
- [71] I. D. Jung, F. X. Kartner, N. Matuschek, D. H. Sutter, F. Morier-Genoud, G. Zhang, and U. Keller. Self-starting 6.5-fs pulses from a Ti:sapphire laser. *Optics Letters*, 22(13), July 1 1997.
- [72] U. Keller, K. J. Weingarten, F. X. Kartner, D. Kopf, B. Braun, I. D. Jung, R. Fluck, C. Honninger, N. Matuschek, and J. Aus der Au. Semiconductor Saturable Absorber Mirrors (SESAM's) for femtosecond to nanosecond pulse generation in solid-state lasers. *IEEE J. of Selected Topics in Quantum Electronics*, 2(3):435–453, September 1996.
- [73] F. X. Kartner, I. D. Jung, and U. Keller. Soliton mode-locking with saturable absorbers. *IEEE J. of Selected Topics in Quantum Electronics*, 2(3):540–556, September 1996.



- [74] J.-C. Diels and W. Rudolph. *Ultrashort Laser Pulse Phenomena*. Academic Press, New York, 1996.
- [75] W. Macek and D. T. M. Davis Jr. Rotation rate sensing with traveling-wave ring lasers. *Appl. Phys. Lett.*, 2:67–68, 1963.
- [76] M. Lai, J.-C. Diels, and M. L. Dennis. Nonreciprocal measurements in femtosecond ring lasers. *Opt. Lett.*, 17:1535–1537, 1992.
- [77] Briggs Atherton, Scott Diddams, and J.-C. Diels. Ultrasensitive phase measurements with femtosecond ring lasers. In F. W. Wise and C. P. J. Barty, editors, *Proceedings of SPIE in Generation, Amplification, and Measurement of Ultrashort Laser Pulses II*, Vol. 2377, Bellingham, WA, 1995.
- [78] Briggs Atherton, Scott Diddams, and J.-C. Diels. Stabilization of a mode-locked ring laser. In *Quantum Electronics Conference, Vol. 16, OSA Technical Digest Series*, pages 8–9, Washington, D.C., 1995. Optical Society of America.
- [79] Amnon Yariv. *Optical Electronics*. Saunders College Publishing, Philadelphia, 4 edition, 1991.
- [80] N. Finlayson, W. C. Banyai, C. T. Seaton, G. I. Stegeman, M. O'Neill, T. J. Cullen, and C. N. Ironside. Optical nonlinearities in CdSxSe(1-x)-doped glass waveguides. *J. Opt. Soc. Am. B*, 6(6):675–684, April 1989.
- [81] Y. Wang, N. Herron, W. Mahler, and A. Suna. Linear- and nonlinear-optical properties of semiconductor clusters. *J. Opt. Soc. Am. B*, 6(4):808–813, April 1989.
- [82] R. L. Sutherland. *Handbook of Nonlinear Optics*. Marcel Dekker, New York, 1996.
- [83] N. Sarakura, Y. Ishida, H. Nakano, and T. Yanagawa. All solid-state cw passively mode-locked Ti:sapphire laser using a colored glass filter. *Appl. Phys. Lett.*, 57:229–230, 1990.
- [84] S. I. Wax. Phase modulation of a ring-laser gyro-Part I: Theory. *IEEE J. of Quantum Electronics*, 8(3):343–351, March 1972.

- [85] S. I. Wax and M. Chodorow. Phase modulation of a ring-laser gyro-part II: experimental results. *IEEE J. of Quantum Electronics*, 8(3):352–361, March 1972.
- [86] F. Estable, F. Salin, M. Allain, P. Georges, and A. Brun. Direct measurement of saturation fluence in Ti:Al<sub>2</sub>O<sub>3</sub>. *Optics Communication*, 72(3,4):235–238, 15 July 1989.
- [87] F. J. Duarte and J. A. Piper. Dispersion theory of multiple prisms beam expanders for pulsed dye lasers. *Optics Comm.*, 43:303–307, 1982.
- [88] C.-L. Pan, C.-D. Hwang, J.-C. Kuo, and J.-M. Shieh. Effect of dye concentration on picosecond and femtosecond cw passively mode-locked Ti:sapphire lasers. *Optics Letters*, 17(20):1444 – 1446, 15 October 1992.
- [89] Ci-Ling Pan F. Ganikhanov, J.-M. Hsieh. Dynamics of the absorption recovery of dyes commonly used as intracavity saturable absorbers in self-starting passively mode-locked Ti:sapphire lasers. *Optics Communications*, 114:289 – 294, 1 February 1995.
- [90] Q. Xing, W. Zhang, and K. M. Yoo. Self Q-switch self mode-locked Ti:sapphire laser. *Optics Communications*, 119:113–116, 1995.
- [91] A. Agnesi, A. Del Corno, P. Di Trapani, M. Fogliani, G. C. Reali, C.-Y. Yeh J.-C. Diels, X. M. Zhao, and V. Kubecek. Generation of extended pulse trains of minimum duration by passive negative feedback applied to solid-state Q-switched lasers. *IEEE Journal of Quantum Electronics*, 28(3):710 – 719, March 1992.
- [92] V. L. Kalashnikov, N. I. Zhavoronkov, I. G. Poloyko, V. P. Mikhailov, and D. von der Linde. Regular, quasi-periodic, and chaotic behavior in continuous-wave solid-state Kerr-lens mode-locked lasers. *J. Opt. Soc. Am. B*, 14(10):2691–2695, October 1997.
- [93] J. Jasapara. Confirmed mode-locked pulses in between Q-switched pulses in a Ti:sapphire laser. *Personal Communication*, 1997.
- [94] M. J. Bohn and J.-C. Diels. Measuring intracavity phase changes by use of double pulses in a linear cavity. *Optics Letters*, 22(9):642–644, May.

- [95] M. J. Bohn and J.-C. Diels. Bidirectional Kerr-lens mode-locked femtosecond ring laser. *Optics Communications*, 141:53–58, August 1997.
- [96] T. Tsang. Observation of higher order solitons from a mode-locked Ti:sapphire laser. *Optics Lett.*, 18:293–295, 1993.
- [97] M. Lai, J. Nicholson, and W. Rudolph. Multiple pulse operation of a femtosecond Ti:sapphire laser. *Optics Communications*, 142:45–49, October 1997.
- [98] V. L. Kalashnikov, N. I. Zhavoronkov, I. G. Poloyko, and V. P. Mikhailov. Control of mode-locking efficiency in a Kerr-lens mode-locked Ti:sapphire laser. *J. Opt. Soc. Am. B*, 14(10):2705–2709, October 1997.
- [99] R. Y. Chiao, P. L. Kelley, and E. Garmire. *Physical Review Letters*, 17:1158, 1966.
- [100] R. L. Carman, R. Y. Chiao, and P. L. Kelley. *Physical Review Letters*, 17:1281, 1966.
- [101] D. C. Hutchings, M. Sheik-Bahae, D. J. Hagan, and E. W. Van Stryland. Kramers-Kronig relations in nonlinear optics. *Optical and Quantum Electronics*, 24:1–30, 1992.
- [102] C. Radzewicz, G. W. Pearson, and J. S. Krasinski. Use of ZnS as an additional highly nonlinear intracavity self-focusing element in a Ti:sapphire self-modelocked laser. *Optics Communications*, 102(5, 6):464 – 468, 15 October 1993.
- [103] N. Bloembergen and P. S. Pershan. Light waves at the boundary of nonlinear media. *Physical Review*, 128(2):606–622, October 1962.
- [104] B. Bouma, A. Gouveia-Neto, J. A. Izatt, J. Russell, R. Sierra, U. Keller, and J. G. Fujimoto. Hybrid mode locking of a flash-lamped-pumped Ti:Al<sub>2</sub>O<sub>3</sub> laser. *Optics Letters*, 19:1858, 1994.
- [105] J. M. Dudley, D. T. Reid, M. Ebrahimzadeh, and W. Sibbett. Characteristics of a non-critically phasematched Ti:sapphire pumped femtosecond optical parametric oscillator. *Optics Communications*, 104(4,5,6):419–430, January 1994.
- [106] R. M. Shelby and M. Rosenbluh. Generation of pulsed squeezed light in a mode-locked optical parametric oscillator. *Appl. Phys. B*, 55:226–232, 1992.

- [107] D. S. Butterworth, S. Girard, and D. C. Hanna. A simple technique to achieve active cavity-length stabilisation in a synchronously pumped optical parametric oscillator. *Optics Communications*, 123:577–582, February 1996.
- [108] A. Hache, G. R. Allan, and H. M. van Driel. Effects of cavity detuning on the pulse characteristics of a femtosecond synchronously pumped optical parametric oscillator. *J. Opt. Soc. Am. B*, 12(11):2209–2213, November 1995.
- [109] T. Kartaloglu, K. G. Koprulu, and O. Aytur. Phase-matched self-doubling optical parametric oscillator. *Optics Letters*, 22(6):280–282, March 1997.
- [110] P. E. Powers, C. L. Tang, and L. K. Cheng. High-repetition-rate femtosecond optical parametric oscillator based on CsTiOAsO<sub>4</sub>. *Optics Letters*, 19(1):37–39, January 1994.
- [111] D. T. Reid, M. Ebrahimzadeh, and W. Sibbett. Noncritically phase-matched Ti:sapphire-pumped femtosecond optical parametric oscillator based on RbTiOAsO<sub>4</sub>. *Optics Letters*, 20(1):55–57, January 1995.
- [112] J. D. Kafka, M. L. Watts, and J. W. Pieterse. Synchronously pumped optical parametric oscillators with LiB<sub>3</sub>O<sub>5</sub>. *J. Opt. Soc. Am. B*, 12(11):2147–2157, November 1995.
- [113] M. Ebrahimzadeh, S. French, and A. Miller. Design and performance of a singly resonant picosecond LiB<sub>3</sub>O<sub>5</sub> optical parametric oscillator synchronously pumped by a self-mode-locked Ti:sapphire laser. *J. Opt. Soc. Am. B*, 12(1):2180–2191, November 1995.
- [114] D. E. Spence, S. Wielandy, C. L. Tang, C. Bosshard, and P. Gunter. High-repetition-rate femtosecond optical parametric oscillator based on KNbO<sub>3</sub>. *Optics Letters*, 20(7):680–682, April 1995.
- [115] S. D. Butterworth, P. G. R. Smith, and D. C. Hanna. Picosecond Ti:sapphire-pumped optical parametric oscillator based on periodically poled LiNbO<sub>3</sub>. *Optics Letters*, 22(9):618, May 1997.

- [116] K. Schneider, P. Kramper, S. Schiller, and J. Mlynek. Toward an optical synthesizer: A single-frequency parametric oscillator using periodically poled LiNbO<sub>3</sub>. *Optics Letters*, 22(17):1293, September 1997.
- [117] W. S. Pelouch, P. E. Powers, and C. L. Tang. Ti:sapphire-pumped, high-repetition-rate femtosecond optical parametric oscillator. *Optics Letters*, 17(15):1070–1072, August 1992.
- [118] C. Fallenich, B. Ruffing, Th. Herrmann, A. Nebel, R. Beigang, and R. Wallenstein. Experimental investigation and numerical simulation of the influence of resonator-length detuning on the output power, pulse duration and spectral width of a cw mode-locked picosecond optical parametric oscillator. *Appl. Phys. B*, 60:427–436, 1995.
- [119] J. E. Rothenberg. Observation of the transient expansion of heated surfaces by picosecond photothermal deflection spectroscopy. *Optics Letters*, 13(9):713–716, September 1988.
- [120] H. T. Grahn, H. J. Maris, and J. Tauc. Picosecond ultrasonics. *IEEE J. Quantum Electron.*, QE-25:2562–2569, 1989.
- [121] O. B. Wright and V. E. Gusev. Ultrafast generation of acoustic waves in copper. *IEEE Trans. Ultrasonics, Ferroelectrics and Frequency Control*, 42(3):331–338, May 1995.
- [122] W. Chen, Y. Lu, H. J. Maris, and G. Xiao. Picosecond ultrasonic study of localized phonon surface modes in Al/Ag superlattices. *Physical Review B*, 50(19):14506–14515, November 1994.
- [123] P. Basseras, S. M. Gracewski, G. W. Wicks, and R. J. D. Miller. Optical generation of high-frequency acoustic waves in GaAs/Al<sub>x</sub>Ga<sub>1-x</sub>As periodic multilayer structures. *J. Appl. Phys.*, 75(6):2761–2768, March 1994.
- [124] J. Zyss. *Molecular Nonlinear Optics*. Academic Press, Boston, 1994.